CHALMERS

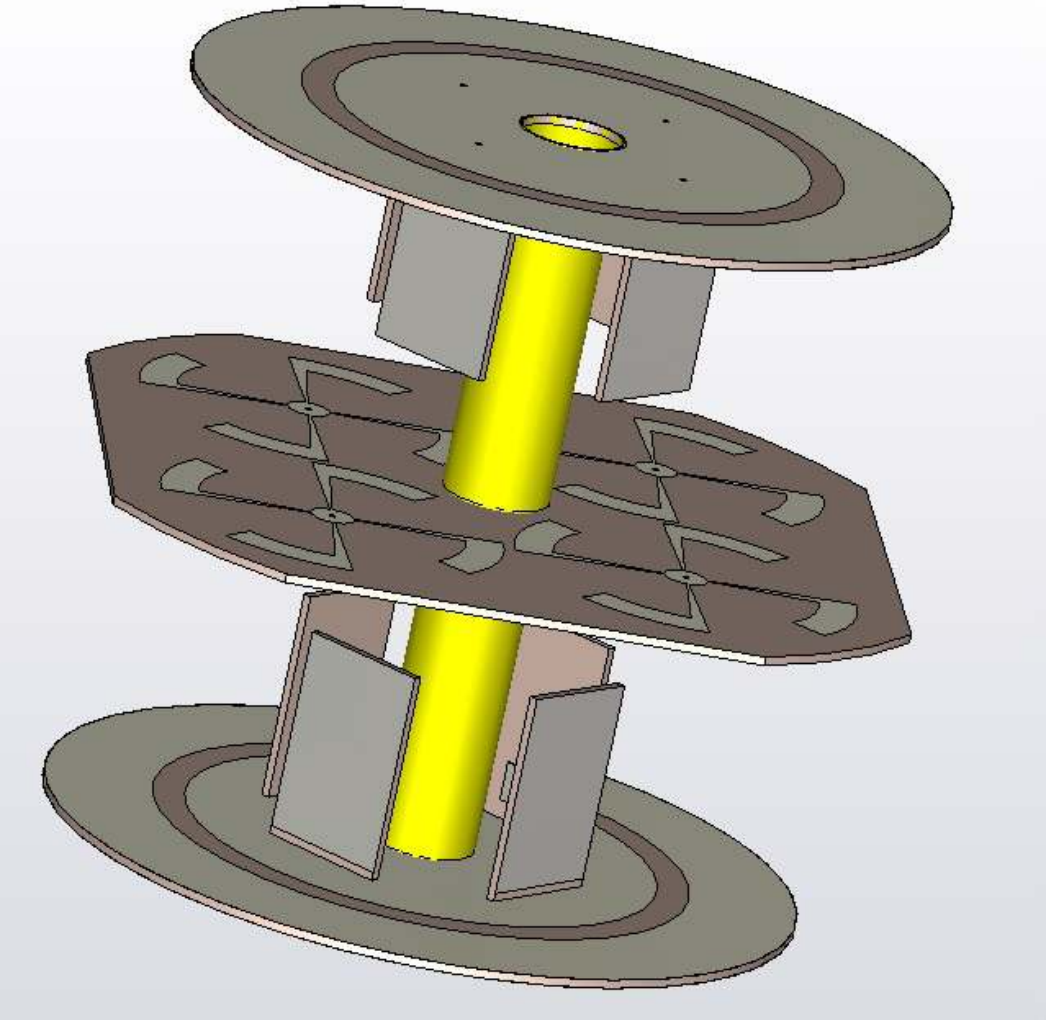

MIMO configurable array for sector/omni-directional coverage

KONSTANTINOS PRIONIDIS

Department of Signals & Systems
Chalmers University of Technology
Gothenburg, Sweden 2014

Abstract

A reconfigurable multiport antenna intended for base station use is designed and a prototype is manufactured. The antenna is composed of twelve elements; eight monopole-patches which provide vertical polarization and four loops acting as magnetic dipoles providing horizontal polarization. The antenna can operate under various configurations, namely as a twelve, eight (logical) or two (logical) port antenna. In particular, when in two-port mode, the antenna has two logical ports, one for each orthogonal polarization and in addition can act as either an omni-directional or a sector-beam radiator, hence providing extra usability. Apart from traditional measurements (S-parameters, radiation patterns etc.) the antenna is also characterized in terms of diversity gain and MIMO capacity by measurements in a reverberation chamber. Furthermore, simulations in Huawei's channel emulator are performed in order to be investigated whether different antenna patterns give different performance in various space distributions of mobile users.

Acknowledgements

Foremost, i would like to thank my principal supervisor, Mattias Gustafsson, for giving me the opportunity to work in such an exciting project and for his constant scientific consultation. Mattias believed in me and this is of great importance to me. Additionally, i would like to thank Mats Högberg and Bengt Madeberg who willingly helped me whenever asked, without any second thoughts as well as my academic supervisor, Dr. Xiaoming Chen, and Prof. Per-Simon Kildal for their useful comments and remarks.
I would also like to thank "Bluetest AB" and John Kvarnstrand for giving me access to their reverberation chambers and Dr. Tilmann Wittig from "CST Computer Simulation Technology AG" for the interest he showed in this project and his eagerness to assist me.

My gratitude towards my family is just indescribable.

Konstantinos Prionidis, Göteborg 22/08/2014

Contents

1

Introduction

Increasing number of mobile users and the ever growing demand for data traffic require the redesign of existing mobile networks in order to become more efficient and provide higher capacity. Reduction of inter-cell interference which will increase the network spectral efficiency and the need of better power efficiency tend to decrease the size of the cells (micro-cells, pico-cells) and as a result new types of base stations with smart antennas that can adapt to different environments and exploit the possibilities of a multipath environment should be employed.

The purpose of this master thesis is the development of such a smart base station antenna which can support MIMO and yet having the ability to adapt in various environments by having a flexible radiation pattern. The driving idea is that the antenna to be designed consists of two independent orthogonal polarized antenna arrays which in principle radiate omni-directionally but also have the ability to form sector beams by proper phase excitation of each individual element. In this way, for instance, the antenna could be used as an omni-directional radiator when placed in the center of a city square or as a sector radiator when facing a street or mounted on a wall while, at the same time, having the ability to transmit/receive distinct information through two uncorrelated streams; one through each orthogonal polarization. Moreover, since the antenna will be formed by many elements, it could be used in a higher order MIMO to rapidly increase the point-to-point capacity.

In this report, the background theory that supports the concept of the antenna is initially given in chapter 2. Chapter 3 describes the whole process of the antenna development together with simulated and measured results. In chapter 4, the antenna is characterized in respect to diversity and MIMO capabilities and its performance is investigated through network simulations whilst Chapter 5 contains a brief conclusion and suggestions for further investigation. Finally, in appendix F, a performance comparison between two commercial 3D-EM simulation softwares is discussed.

2

Background

2.1 Antenna

An antenna is a device which can either receive or transmit electromagnetic energy. Antennas are essential components of wireless communication systems since it is those that will transform the information produced in a transmitter to electromagnetic waves that can travel through the air or, the inverse way, it is the component that will receive electromagnetic waves and guide them to the receiver where the information can be decoded.

An antenna can be as simple as a piece of cable where acceleration of flowing charge due to bending, termination or in general due to discontinuities will result in electromagnetic radiation [1, p. 9]. But antennas can also be complex and very big structures. In traditional Line of Sight (LOS) environments, antennas are characterized mainly by their radiation pattern and the radiation efficiency. The radiation pattern (radiation fields or far field function) describes how the antenna directs the energy that is accepted in its ports, towards free space. The ideal case is an isotropic antenna which spreads the electromagnetic energy equally in space (figure 2.1(a)), thus having a power gain of 1 throughout the whole sphere. Another kind of radiation pattern which is commonly seen in practice is the so called omni-directional pattern (figure 2.1(b)) and is considered the closest possible realistic equivalent of isotropic radiation. The omni-directional pattern, has a power gain larger than one at elevation angle $\theta = 90^o$ but almost zero at $\theta = 0^o$ and is the best choice of antenna if we demand the widest possible coverage. Among many others, there is also the sector beam pattern (figure 2.1(c)). An antenna with a sector beam pattern radiates most of the energy towards a particular direction, a very useful feature, hence it is widely used in today's wireless communications.

The radiation efficiency of an antenna is a metric of how well the antenna radiates the power that has been accepted by the antenna port. Said in another way, radiation efficiency represents the ohmic losses of the antenna, that is the energy that is absorbed by

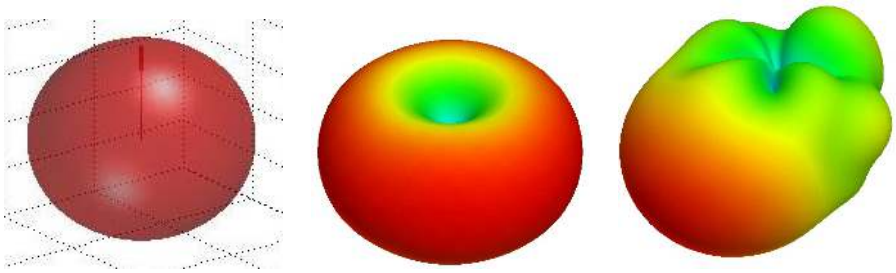

(a) Isotropic pattern (b) Omni pattern (c) Sector Beam

Figure 2.1: Examples of radiation patterns

the antenna and not radiated. It is the ratio of the power radiated to the power accepted :

$e_{rad} = \frac{P_{rad}}{P_{acc}}$

where :

- P_{rad} is the radiated power
- P_{acc} is the accepted power

One can also include more factors of efficiency such as transmission efficiency, e_r, which accounts for the mismatch losses and polarization efficiency e_{pol} (see section 2.2) to calculate a total antenna efficiency [2, p. 50] :

$e_{ant} = e_{rad} \cdot e_r \cdot e_{pol}$

2.2 Wave and Antenna Polarization

The electromagnetic (EM) fields that are radiated by an antenna are usually produced by steady sinusoidal sources hence the fields will have steady sinusoidal time variation as well, thus the instantaneous field at any point can be written as :

$\overrightarrow{E}(x,y,z,t) = \mathrm{Re}\{\mathbf{E}(x,y,z)e^{j\omega t}\}$ and $\overrightarrow{H}(x,y,z,t) = \mathrm{Re}\{\mathbf{H}(x,y,z)e^{j\omega t}\}$

for the electric and magnetic field respectively. Each vector field have both $\hat{\mathbf{x}}$, $\hat{\mathbf{y}}$ and $\hat{\mathbf{z}}$ but in the far field[1] the longitudinal field component $\hat{\mathbf{z}}$ becomes negligible and the field

[1]The far field of the antenna is at a distance $\geq D^2/\lambda$ (D is the largest dimension of the antenna)from the phase center and it is the region where the radiation pattern is measured. This condition is called Fraunhofer condition.

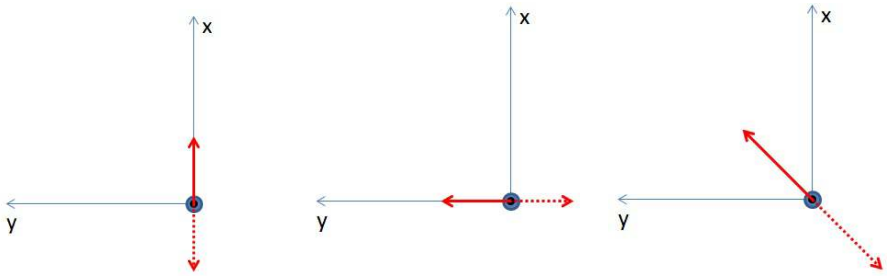

(a) Linear x-polarized (vertical) (b) Linear y-polarized (horizontal) (c) Linear Polarized at 45^o angle

Figure 2.2: Examples of linear polarized waves. The wave propagates towards the reader and the red line represents the electric field vector

can be considered quasi-TEM field [3, p. 90]. This means that if the radiated wave is propagating towards the z-axis then both the electric and magnetic field lie on the x-y plane, i.e perpendicular to the direction of propagation and on a right angle between them. Hence, the electric field can be written as :

$\mathbf{E} = [E_x\hat{x} + E_y\hat{y}]e^{-jkz}$, where:

E_x : is the x-component of the electric field
E_y : is the y-component of the electric field
k : is the wave number ($k = 2\pi/\lambda$) .

The polarization of a plane wave is defined as the direction of its electric field. A wave can be linear, circular or in general, elliptical polarized. If the electric field is directed on a fixed line in the x-y plane for any distance z, then we say that the field is linearly polarized. If this line is the x-axis or y-axis then the wave is x-polarized or y-polarized respectively but in general it can be linear polarized at any angle in-between (see figure 2.2). When spherical coordinates are used instead, then we can say that the wave is $\hat{\theta}$ or $\hat{\phi}$ polarized (figure 2.3). In practice the terms **vertical** and **horizontal** polarization (relative to the direction of propagation) are commonly used and this is the notation that will mainly be used in this report.

In order for the field to be linear polarized the phase difference between the x and y component should be $k \times \pi$ for k:integer. If the two components are equal and they have a phase difference of $|\pi/2|$ then the wave is circular polarized. In any other case the polarization is elliptical. It is the concept of the two orthogonal polarizations, vertical and horizontal, that this project is partly based upon so here we don't go into more details regarding circular and elliptical polarizations.

A transmitting antenna's polarization depends on the polarization of the wave that it generates. For instance, if the waves going out of an antenna are linearly, vertical polarized then we say that the antenna is vertical polarized. Due to reciprocity, the

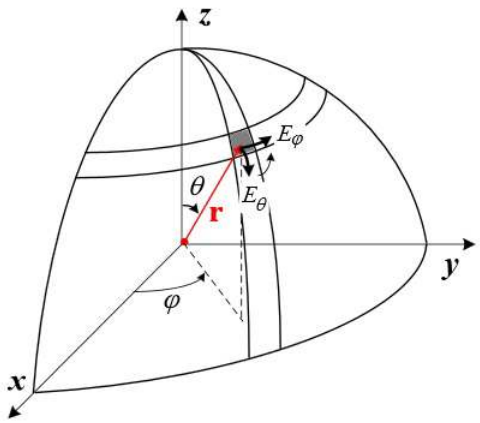

Figure 2.3: Field vector and components in spherical coordinates.

same holds for a receiving antenna, that is, a receiving antenna can get the most out of an incident wave (in terms of power) if its polarization is the same as that of the incident wave, i.e they are aligned.

2.3 Antenna arrays, beamforming and coupling

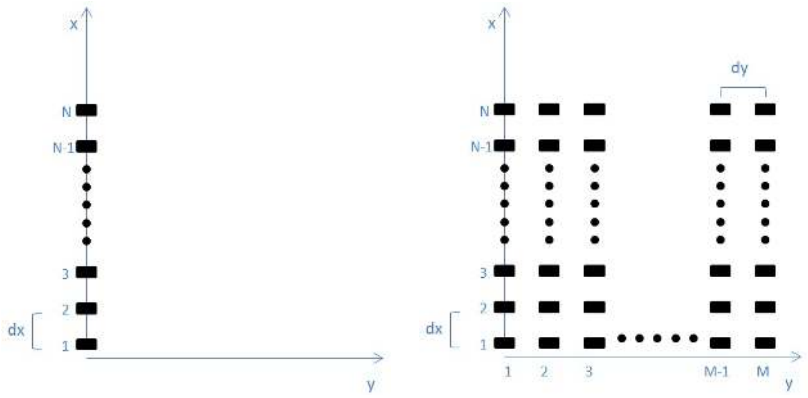

(a) Linear array (b) Planar array

Figure 2.4: Example of array types. A linear, N elements array to the left and an NxM planar array to the right.

Individual antenna elements, such as simple electric dipoles for example, can be combined together to form a collection called array which can provide, in general, higher directivity values. Moreover, they give flexibility regarding the radiation pattern since it is possible to shape it by changing the amplitude, position or the phase excitation of the individual elements. Arrays are called linear when the elements are positioned along

one direction, x, y or z (figure 2.4(a)) and planar when positioned along two directions, xy or xz for instance (figure 2.4(b)).

To show the operation of an antenna array we will consider the simplest case of a uniform, linear, 2-element array in a 2-D environment. It is called uniform because the elements are identical and equally spaced with the same amplitude and a progressive phase change, although in general an array can be formed by elements of any type, with non uniform amplitude, phase or spacing.

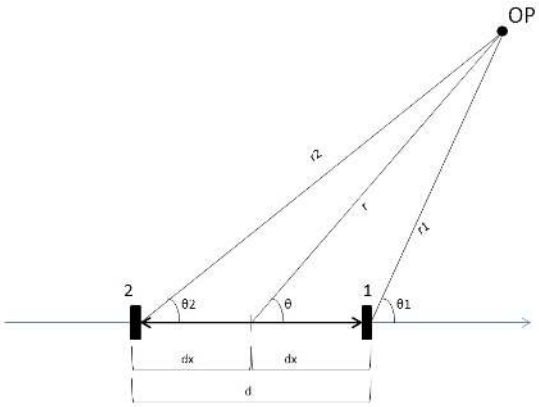

Figure 2.5: Two element linear array.

Consider the observation point **OP** and the elements 1 and 2 that are positioned along the axis in a distance d (figure 2.5). If we neglect any coupling effect (see later), since the elements are identical they will have the same radiation patterns,$\mathbf{G}(\hat{\mathbf{r}})$ or $\mathbf{G}(r,\theta,\phi)$. Hence, by referring to each element's individual reference point (let's say the center of each element), the electric field at **OP** will be :

$\mathbf{E_1} = \frac{1}{r_1} e^{-j(k \cdot r_1 + p_1)} \mathbf{G}(\hat{\mathbf{r_1}})$, due to element 1

and

$\mathbf{E_2} = \frac{1}{r_2} e^{-j(k \cdot r_2 + p_2)} \mathbf{G}(\hat{\mathbf{r_2}})$, due to element 2

where r_1 and r_2 are the distance from element 1 and 2 to the **OP** respectively, $\frac{1}{r}$ is the divergence factor, namely how the amplitude attenuates with distance and p_1, p_2 are the phase excitations of each element. Since superposition holds, the total field at **OP** will be :

$$\mathbf{E} = \mathbf{E_1} + \mathbf{E_2} = \frac{1}{r_1} e^{-j(k \cdot r_1 + p_1)} \mathbf{G}(\hat{\mathbf{r_1}}) + \frac{1}{r_2} e^{-j(k \cdot r_2 + p_2)} \mathbf{G}(\hat{\mathbf{r_2}}). \tag{2.1}$$

Moreover, if the **OP** is located far enough, we can use the Fraunhofer approximations, that is :

1. $\frac{1}{r_1} \simeq \frac{1}{r_2} \simeq \frac{1}{r}$
2. $\theta_1 \simeq \theta_2 \simeq \theta$
3. $r_1 = |\mathbf{r} - \mathbf{dx}| = r - \mathbf{dx} \cdot \mathbf{r} = r - dx \cdot \cos(\theta_1) \simeq r - dx \cdot \cos(\theta) = r - \frac{d}{2} \cdot \cos(\theta)$
4. $r_2 = |\mathbf{r} + \mathbf{dx}| = r + \mathbf{dx} \cdot \mathbf{r} = r + dx \cdot \cos(\theta_2) \simeq r + dx \cdot \cos(\theta) = r + \frac{d}{2} \cdot \cos(\theta)$

where 1 holds for amplitude and 3,4 for phase variations. Hence the total field at **OP** becomes :

$$\begin{aligned}
\mathbf{E} &= \frac{1}{r} e^{-j(k(r - d\cdot\cos(\theta)/2) - dp/2)} \mathbf{G}(\hat{\mathbf{r}}) + \frac{1}{r} e^{-j(k(r + d\cdot\cos(\theta)/2) + dp/2)} \mathbf{G}(\hat{\mathbf{r}}) \\
&= \frac{1}{r} e^{-j(k\cdot r - k\cdot d\cdot\cos(\theta)/2 - dp/2)} \mathbf{G}(\hat{\mathbf{r}}) + \frac{1}{r} e^{-j(k\cdot r + k\cdot d\cdot\cos(\theta)/2 + dp/2)} \mathbf{G}(\hat{\mathbf{r}}) \\
&= \frac{1}{r} \cdot \mathbf{G}(\hat{\mathbf{r}}) \cdot e^{-jk\cdot r} [e^{j(k\cdot d\cos(\theta) + dp)/2} + e^{-j(k\cdot d\cos(\theta) + dp)/2}] \\
&= \frac{1}{r} \cdot \mathbf{G}(\hat{\mathbf{r}}) \cdot e^{-jk\cdot r} \cdot 2\cos(\frac{1}{2}(k \cdot d \cdot \cos(\theta)) + dp)
\end{aligned} \tag{2.2}$$

where dp is the phase difference between the elements and since it is progressive, p_1 and p_2 are substituted by $-dp/2$ and $+dp/2$ respectively. In addition, $\mathbf{G}(\hat{\mathbf{r_1}})$ and $\mathbf{G}(\hat{\mathbf{r_2}})$ are substituted by $\mathbf{G}(\hat{\mathbf{r}})$ because of approximation condition (2). In last line of equation 2.2 Euler's equation has been used.

Equation 2.2 can be divided in two parts. The first one, $\frac{1}{r} \cdot \mathbf{G}(\hat{\mathbf{r}}) \cdot e^{-jk\cdot r}$ can be recognized as the element's contribution to the electric field at **OP** with the reference point lying in the center of the axis. The second part,

$$2\cos(\frac{1}{2}(k \cdot d \cdot \cos(\theta)) + dp) \tag{2.3}$$

is called Array Factor and it is the contribution of the individual elements' combination. From equation 2.3 it is obvious now that changing the spacing d or the phase p of the elements we alter the array factor and hence the total radiation pattern of the array will change. This technique is called beamforming and conceptually is based on the fact that waves radiated by different elements combine sometimes constructively and others destructively thus forming a particular radiation pattern in space. If identical elements are used in the array, with similar amplitudes and fixed positions, then their individual phase can be used to shape the radiation pattern either by analog phase shifter components or in baseband. This type of arrays are called phased arrays and is one of the principles this project is based upon.

By observing equation 2.2 and considering that identical elements are used in the array one can conclude that each element can be replaced by a point source, then the array factor can be calculated considering the point sources and in the end multiply with the elements' radiation pattern to get the array's radiation pattern. Each point source can have the amplitude, position and phase excitation of the element that it replaces. With this in mind we can generalize the array factor for N elements, linearly positioned along one axis. Referring to figure 2.6 and assuming the phase of the first element is zero, the array factor for N elements can be written as :

$$\begin{aligned} AF_{lin} &= \alpha_1 1 + \alpha_2 e^{j(kd_2\cos(\theta)+p_2)} + \alpha_3 e^{j2(kd_3\cos(\theta)+p_3)} + \cdots + \alpha_N e^{j(N-1)(kd_N\cos(\theta)+p_N)} \\ &= \sum_{n=1}^{N} \alpha_n e^{j(n-1)(kd_n\cos(\theta)+p_n)} \end{aligned} \tag{2.4}$$

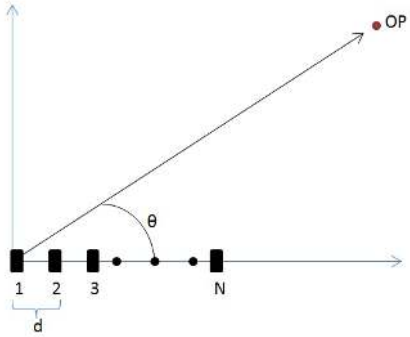

Figure 2.6: Linear N array

Moreover, assuming that the array is uniform (uniform spacing and phase difference) with equal element amplitudes, equation 2.4 simplifies to

$$\begin{aligned} AF_{lin\_u} &= 1 + e^{j(kd\cos(\theta)+p)} + e^{j2(kd\cos(\theta)+p)} + \cdots + e^{j(N-1)(kd\cos(\theta)+p)} \\ &= \sum_{n=1}^{N} e^{j(n-1)(kd\cos(\theta)+p)} \end{aligned} \tag{2.5}$$

Expanding the analysis of the array factor to planar arrays (figure 2.7), we can think of a planar array as a linear collection (in y direction) of linear arrays (in x direction). Hence, by following the same reasoning as above the array factor of a planar array can

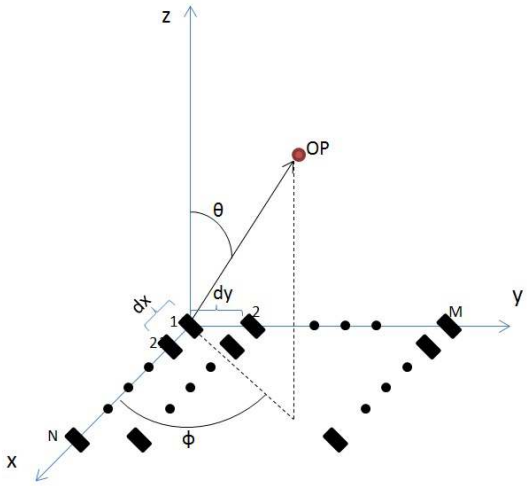

Figure 2.7: Planar NxM array

be written as :

$$\begin{aligned} AF_{pl} &= \sum_{m=1}^{M} AF_{lin}\beta_m e^{j(m-1)\xi_m} \\ &= \sum_{m=1}^{M}\left(\sum_{n=1}^{N}\alpha_n e^{j(n-1)\psi_n}\right)\beta_m e^{j(m-1)\xi_m} \\ &= \left(\sum_{n=1}^{N}\alpha_n e^{j(n-1)\psi_n}\right)\left(\sum_{m=1}^{M}\beta_m e^{j(m-1)\xi_m}\right) \qquad (2.6) \\ &= AF_{linX}\cdot AF_{linY} \qquad (2.7) \end{aligned}$$

thus, the array factor of a planar array is the product of the linear array factor in x-direction and the one in y direction.

In equation 2.6,

$\psi_n = k \cdot dx_n \cdot \sin(\theta)\cos(\phi) + px_n$

and

$\xi_m = k \cdot dy_m \cdot \sin(\theta)\sin(\phi) + py_m$

because when the observation point is in 3-dimension space and the elements lie on

the x or y axis, the distance to the axis origin is dependent on both θ and ϕ angles[1]. That is, the distance that a wave travels with respect to the reference point depends both on elevation and azimuth angles.

In the preceding analysis it has been assumed that since the elements that are used in the array are identical, their radiation patterns are exactly the same. In reality when an individual element radiates, some of the radiated energy is absorbed by the neighboring elements resulting in reduction of the element's efficiency. Moreover, part of this absorbed energy will be re-scattered back, radiated and absorbed by the (initially) radiating element, forming new currents in the antenna and eventually altering the radiation pattern and the input impedance of the element. This electromagnetic interaction between radiating elements is called mutual coupling and mainly depends on the type of the antennas (radiation characteristics) and their relative distance.

In order to be more precise when calculating the array factor or the total radiation efficiency of an array, the embedded element pattern [4] and the embedded element radiation efficiency should be measured. That is, the radiation pattern and the radiation efficiency of an element when all other elements of the array are present and terminated with their port impedances.

2.4 Diversity and MIMO

Wireless communication systems can exist in many different environments, from line-of-sight (LOS) where the transmitting and receiving antennas have only one straight path to environments where the there are only scattered/reflected paths. LOS communication makes use of the traditional antenna characteristics such as the radiation pattern and in this kind of environment the signal power decreases according to the free space model (Friis transmission equation) [5, p. 31]. On the other extreme, the transmitting and receiving antennas can have no LOS connection but waves that have been reflected, refracted or scattered by objects and big obstacles may combine at the receiving antenna to provide communication link, a phenomenon called **multipath** since waves follow many different paths until they reach the receiving antenna. The problem with multipath environments is that since the waves that arrive at the antenna are generally independent and the environment changes over time (an urban environment for instance) they may combine sometimes constructively and others destructively giving rise to a very fast and sharp variation of the received signal power. This is called small scale fading and sometimes can result in deep fade (very low received power) where communication breakdown can occur. A comparison between free space loss and small-scale fading can be seen in figure 2.8.

In order to mitigate the effect of small scale fading and provide more robust communication links diversity can be exploited. There are many kinds of diversities that can be used such as time and frequency diversity but it's space, radiation and polarization diversities that will be discussed here.

[1] An explanation about this is given in Appendix A and equations A.12-A.15

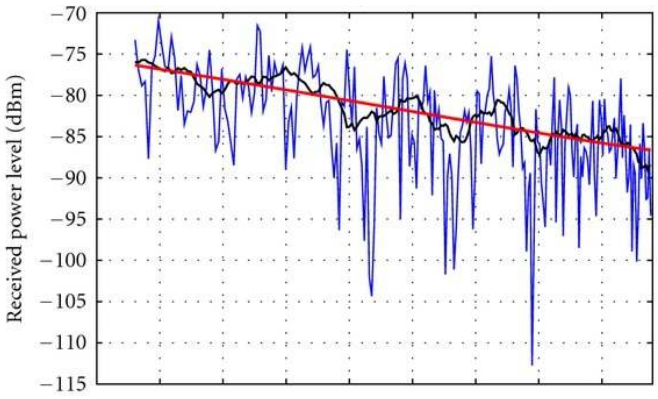

Figure 2.8: Path Loss (red) vs Small scale fading (blue)

In space diversity more than one element can be used at the receiving antenna. Each element will generally sense independent signals and it is very unlikely that all signals are in deep fade simultaneously. Thus, by combining those signals under a diversity combining mechanism deep fades can disappear resulting in a more robust communication link with increased capacity. There are several ways of combining the signals received in each port but the three techniques used in this work are the following:

- Selection Combining (SC): The signals at each port (branch) are constantly monitored and always only the strongest one is forwarded to the receiver circuitry. This is the simplest form of signal combining and requires no complex electronics but the diversity gain diminishes rapidly when additional branches are added.
- Equal gain Combining (EGC): The phase of the signal in each branch is corrected so that signals in all branches have the same phase and then they are all added together. This is a more complex method than SC but it provides higher diversity gains.
- Maximal Ration Combining (MRC): As in EGC, phase is corrected so that signals in all branches share the same phase. In addition, when signals are added together, each is weighted with respect to its SNR; signals with higher SNR receive more weight. This combining technique requires the most sophisticated circuitry but produces the highest gain among the three. MRC is also commonly know as matched filtering.

In order for the different signals that are received to be uncorrelated, the elements should be spaced at least half a wavelength apart because it is known that in multipath two signals de-correlate approximately over a distance of half a wavelength for non-directive antenna elements. In general, the more the signals are correlated the less we gain by diversity. Diversity gains, as defined in [6], can be distinguished as apparent, effective and actual gain.

Polarization and radiation pattern diversity can be understood with a similar reasoning as above. If for instance the antenna has two ports with orthogonal polarizations (one being vertical polarized and the other being horizontal polarized) it will sense two different signals, one vertical and one horizontal polarized which in general, are uncorrelated. The same holds for radiation pattern diversity, namely, when the radiation patterns of each element do not intersect then signals sensed at each port will be independent and will mitigate small scale fading if combined properly.

It has been mentioned before that when there are radiating elements close to each other (in an array for instance) there will be eventually coupling among them so the radiation patterns will change and the radiation efficiency will be reduced. In diversity schemes, this has two effects. Since the embedded radiation patterns change, the signals sensed will be less correlated and this will provide some diversity gain. On the other hand, radiation efficiency is reduced resulting in degradation of diversity gain. It has been shown in [6] that diversity gain degradation due to reduction in radiation efficiency is higher than improvement due to radiation pattern de-correlation so, in general, coupling between antenna elements will reduce the diversity gain.

It has to be noted that antenna diversity can be used at the transmitter side as well. If there is knowledge about the channel state at the transmitter then the different signals to be transmitted can be pre-processed (with matched filtering for example) such that they always combine constructively at the receiver side hence deep fading is wiped out.

In transmit matched filtering, the symbol $\tilde{x}$ has its phase and amplitude modified to match the channel to the receiver, hence it is first multiplied at the transmitter by w_i^* for $i = 1 : T$ where T is the number of the transmit antennas. At the receiver the transmitted signals are added up as:

$$y = \left(\sum_{i=1}^{M_T} h_i w_i^* \right) \tilde{x} + n = \mathbf{w}^H \mathbf{h}\, \tilde{x} + n \tag{2.8}$$

where $\mathbf{w}$ is a column vector containing the complex weights $w_1 \cdots w_T$, $\mathbf{h}$ contain the channel coefficients and n is white noise with zero mean and variance σ_n^2. If the transmit power is denoted as $\overline{P}$ then the SNR of the received signal is:

$$SNR = \frac{\overline{P}|\mathbf{w}^H \mathbf{h}|^2}{\sigma_n^2} \tag{2.9}$$

The quantity $|\mathbf{w}^H \mathbf{h}|^2$ is maximized when the two vectors, $\mathbf{w}$ and $\mathbf{h}$, are aligned, that is when $\mathbf{w} = \mathbf{h}/||\mathbf{h}||$, thus the received signal becomes $y = ||\mathbf{h}||\tilde{x}+n$ and the post-processing SNR :

$$SNR_{MF} = \frac{\overline{P}||\mathbf{h}||^2}{\sigma_n^2} \tag{2.10}$$

Matched filtering is known to maximize the post-processing SNR.

Antenna diversity schemes can also be described as single input multiple output (SIMO) when happening at the receiver side or as multiple input single output (MISO)

when happening at the transmitter side. The need for higher capacity though, gave rise to multiple input multiple output systems or **MIMO** where both the transmitting and the receiving antenna have more than one element.

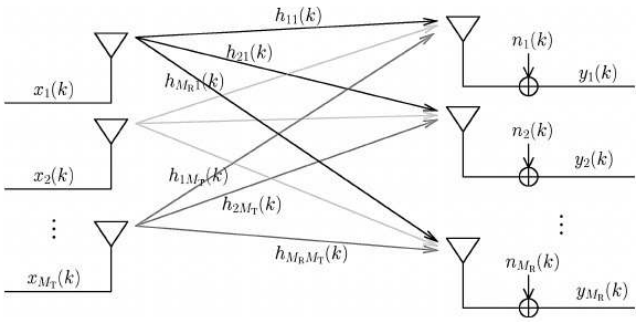

Figure 2.9: $M_T \times M_R$ MIMO system

In a MIMO system there are $M_T \times M_R$ channels formed between the M_T elements of the transmitting and the M_R elements of the receiving antenna (figure 2.9). Hence, a MIMO system can be modeled as :

$$\mathbf{y}(k) = \mathbf{H}(k) * \mathbf{x}(k) + \mathbf{n}(k) \tag{2.11}$$

where :

$\mathbf{y}(k)$ is the $M_R \times 1$ received signal vector,
$\mathbf{x}(k)$ is the $M_T \times 1$ transmitted signal vector,
$\mathbf{H}(k)$ is the $M_R \times M_T$ channel matrix,
$\mathbf{n}(k)$ is the $M_R \times 1$ noise vector,

so, there are M_T different signals leaving the transmitting antenna which then pass through a multipath environment modeled by matrix $\mathbf{H}$ and eventually all consequent waves combine at the M_R terminals of the receiving antenna. Matrix $\mathbf{H}$ contains coefficients for every possible link between the transmitting and receiving terminals. The noise is Gaussian distributed with zero mean and σ_n^2 variance and if the channel is narrowband [2] then equation 2.11 can be written as :

$$\mathbf{y}(k) = \mathbf{H}(k)\mathbf{x}(k) + \mathbf{n}(k) \tag{2.12}$$

If singular value decomposition is performed on matrix $\mathbf{H}$, then it degenerates to :

$$\mathbf{H} = \mathbf{U}\mathbf{\Lambda}\mathbf{V}^H \tag{2.13}$$

[2]When the channel is approximately constant over the whole bandwidth of the signal.

Matrix $\mathbf{\Lambda}$ contains the non-negative singular values of matrix $\mathbf{H}$. The number of those positive singular values shows how many different independent sub-channels can be formed by exploiting MIMO. Hence someone could send as many different streams of data through the channel as the number of positive eigenvalues of $\mathbf{H}$, a process called spatial multiplexing (SM). The number of singular values is also called the rank of matrix $\mathbf{H}$ and can be at most equal to $\min(M_T, M_R)$.

Setting :

$$\tilde{\mathbf{x}} = \mathbf{V}^H \mathbf{x} \iff \mathbf{x} = \mathbf{V}\tilde{\mathbf{x}} \tag{2.14}$$

and

$$\tilde{\mathbf{y}} = \mathbf{U}^H \mathbf{y} \iff \mathbf{y} = \mathbf{U}\tilde{\mathbf{y}} \tag{2.15}$$

where $\tilde{\mathbf{x}}$ and $\tilde{\mathbf{y}}$ are the input and output data stream vectors respectively, equation 2.12 can be rewritten as :

$$\begin{aligned} \mathbf{y} &= \mathbf{H}\mathbf{x} + \mathbf{n} \\ \mathbf{U}\tilde{\mathbf{y}} &= \mathbf{U}\mathbf{\Lambda}\mathbf{V}^H\mathbf{V}\tilde{\mathbf{x}} + \mathbf{n} \\ \mathbf{U}^H\mathbf{U}\tilde{\mathbf{y}} &= \mathbf{U}^H\mathbf{U}\mathbf{\Lambda}\mathbf{V}^H\mathbf{V}\tilde{\mathbf{x}} + \mathbf{U}^H\mathbf{n} \\ \tilde{\mathbf{y}} &= \mathbf{\Lambda}\tilde{\mathbf{x}} + \tilde{\mathbf{n}} \end{aligned} \tag{2.16}$$

where $\tilde{\mathbf{n}} = \mathbf{U}^H\mathbf{n}$ has the same statistics as $\mathbf{n}$. What the above equations (2.12 - 2.16) describe is that initially the data stream $\tilde{\mathbf{x}}$ is multiplied with the matrix $\mathbf{V}$ to get $\mathbf{x}$ (pre-processing) which is then sent through the channel $\mathbf{H}$ while at the other end, the antenna receives $\mathbf{y}$ which is then multiplied with $\mathbf{U}^H$ to recover the initial data stream (post-processing). From equation 2.16 we see that the output $\tilde{\mathbf{y}}$ is formed by the input $\tilde{\mathbf{x}}$ enhanced by each sub-channel gain $\mathbf{\Lambda}$ plus a white Gaussian noise generated at the receiver. The final MIMO system is presented in figure 2.10.

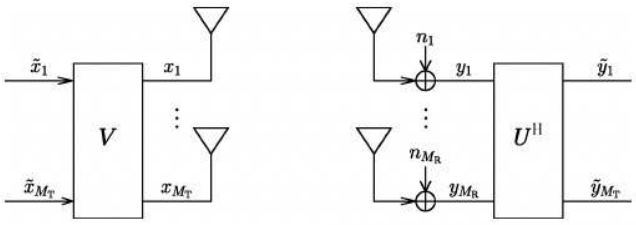

Figure 2.10: $M_T \times M_R$ MIMO system

The capacity of a time-invariant MIMO channel is given by :

$$C_{MIMO} = \sum_{i=1}^{r_H} \log_2 (1 + SNR_i) = \sum_{i=1}^{r_H} \log_2 \left(1 + \frac{P_i^o |\lambda_i|^2}{\sigma_n^2}\right) \tag{2.17}$$

where P_i^o is the optimal power allocated to i-th stream and $|\lambda_i|^2$ is the gain of the i-th sub-channel. An interesting result shown in [7, p. 41] is that, by using the water-filling optimization algorithm, when the system operates under the high SNR regime then it is preferable to allocate equal amounts of power to all streams whilst when under low SNR, all power should be allocated to the strongest stream (highest $|\lambda_i|^2$). However, as it is mentioned in [8], when putting more power in the strongest stream and less to the worst one, the relative throughput of such a SVD-based MIMO system will be worse than allocating equal amounts of power to all streams and therefore, the water-filling technique is not used in practical systems such as LTE. In the same work, it is proposed an inverse power allocation scheme which is performs 2.5 dB better than the equal power allocation and 1.5 dB better than the open-loop zero forcing MIMO system.

3

Antenna Design

Mobile networks were formed until recently by coverage cells that are served by base stations (BS) with directive antennas, usually single (vertical) polarized. The BS's coverage can reach up to 35 kilometers and that's why this type of networks are called macrocells and traditionally, macrocell architecture use relatively high amounts of power at the BS antennas in order to provide this wide coverage. Nowadays, there is the trend of scaling networks down in order to improve power efficiency and increase capacity so new types of network architectures, such as microcell, picocell or even femtocell networks have been evolved. The coverage of these cells can range from few tens of meters up to 2 kilometers, thus new types of base stations are required which in principle, are also scaled down in size and placed in a more dense way throughout urban environments.

The antenna to be developed should be a novel BS smart antenna which serves these new types of networks. It shall be dual polarized, that is, provide both vertical and horizontal polarizations. In that way, since orthogonal polarizations are uncorrelated and considering each polarization as a logical antenna port, antenna diversity and spatial multiplexing can be used to increase the robustness and capacity of the microwave link. Hence, by exploiting antenna diversity, signals sensed by each polarization can get combined together to avoid deep fades. On the other hand by making use of MIMO, two different data streams could be transmitted, one over each polarization. Of course, a prerequisite for MIMO is that the mobile device's antenna should have more than one element.

In addition, the new antenna should be flexible in terms of radiation pattern so it can adapt in many different scenarios. It should for example, provide an omni-directional pattern when placed in the middle of a city square or form a beam and direct the energy when mounted on the wall of a building. For this reason, an array of omni-directional elements shall be designed in order to provide both omni-directional and sector beams by adjusting the phase of the elements in the array (beamforming).

It is shown later (section 3.1) that the current distribution on half-wavelength dipole antennas is such that the antenna produces an omni-directional pattern . Electric and magnetic dipoles can hence provide omni-directional vertical and horizontal polarized patterns respectively but although electric dipoles are easy to design, magnetic dipoles are in general hard to realize. On the whole, the antenna structure will be a 2x2 planar array of both electric and magnetic dipoles (figure 3.1).

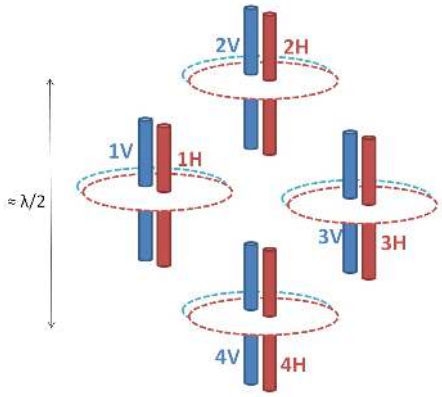

Figure 3.1: A 2x2 planar array. The blue elements are electric dipoles which produce a vertical polarized omni-directional pattern. The red elements are magnetic dipoles which produce a horizontal polarized omni-directional pattern.

As discussed in section 2.3 phase excitation of each element will determine the array factor and consequently the overall radiation pattern of the array. When all elements, [1st,2nd,3rd,4th], are excited with the same phase, an omni-directional pattern is formed and the antenna is said to operate in omni mode whilst when excited with a certain phase difference then some kind of beam shall be formed. In particular, when elements are excited with phase vector $[0^o,90^o,180^o,90^o]$ then a sector beam directed towards the first element is formed, when excited with phase vector $[90^o,0^o,90^o,180^o]$ then a sector beam directed towards the second element is formed and so on. In this case it is said that the antenna operates in sector mode. Another interesting beam that can be used in mobile cellular networks is created when the phase vector $[0^o,180^o,180^o,0^o]$ is used in which case a double beam pattern is formed. The array modes are summarized in figure 3.2.

A fact to be noticed is that separation of elements in the array play a crucial role on the array factor. As can be observed from figures E.2 and E.3 the further away the elements are positioned the more the radiation pattern is disturbed hence the elements on the array should not be placed much more than half-wavelength apart.

The three most important specifications set for the antenna to be designed are:

- Return Loss $\geq$ 10db between 1.7 and 2.2 Ghz [1]
- Coupling $\geq$ 12.5 db (ideally $\geq$ 15db).

[1]Return loss is defined here as $10\log_{10}\frac{P_i}{P_r}$ where P_i is the incident power and P_r is the reflected power.

- Azimuth rippling $\leq$ 3db when in omni mode.
- Sidelobes shall be at least 10db lower than the main beam when in sector mode.

Moreover, the antenna shall be a compact structure and in principle cheap and easy to fabricate.

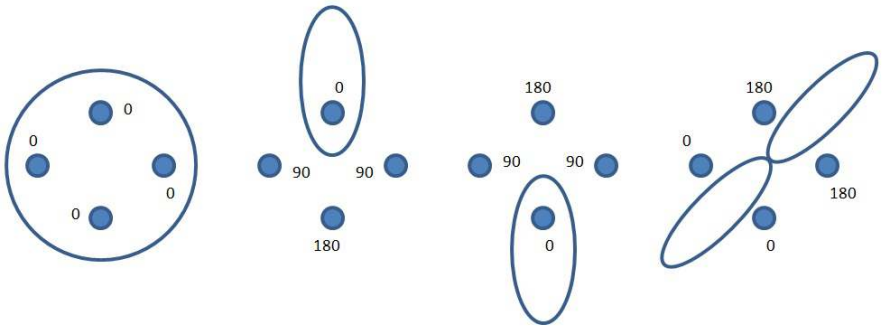

Figure 3.2: Summary of the antenna modes.

3.1 Half-wavelength Dipole Antenna

Imagine a balanced waveguide that carries a sinusoidal signal current as in figure 3.3 where the end of the waveguide is connected to a dipole of length l, one line to each dipole arm. Initially, the current wave propagates into the waveguide and then through the dipole until it reaches the end of the dipole arm where undergoes a total reflection resulting in standing waves formation. As seen from the picture, these standing waves have the same phase in both arms, hence the current distribution through the dipole [1] is given by :

$$\mathbf{I}(z) = \begin{cases} \hat{\mathbf{z}} I_0 \sin\left[\mathrm{k}(\frac{l}{2} - \mathrm{z})\right], & 0 \leq \mathrm{z} \leq \frac{l}{2} \\ \hat{\mathbf{z}} I_0 \sin\left[\mathrm{k}(\frac{l}{2} + \mathrm{z})\right], & -\frac{l}{2} \leq \mathrm{z} \leq 0 \end{cases} \tag{3.1}$$

As can be seen from equations A.1 and A.2 which are derived by the use of auxiliary vector potentials [9], the electric and magnetic fields of a radiating element each has two components, one due to electric and one due to magnetic surface current distribution. As there are no magnetic currents to the described dipole above ($\mathbf{I}_J \neq 0$ and $\mathbf{I}_M = 0$), the electric field at the far-field region is described by equation A.7 and is oriented at $\hat{\mathbf{z}} - (\hat{\mathbf{z}} \cdot \hat{\mathbf{r}})\hat{\mathbf{r}}$ where $\hat{\mathbf{r}}$ is the unitary vector at the direction of propagation. Hence, the electric field is orthogonal to the direction of propagation and vertical polarized. Said in a different way, the electric field has only a $\hat{\theta}$ component since $\hat{\mathbf{z}} - (\hat{\mathbf{z}} \cdot \hat{\mathbf{r}})\hat{\mathbf{r}} = \sin(\theta)\hat{\theta}$ in

[1] The Dipole is assumed to be positioned along the z axis. Moreover, a very thin dipole is considered hence the current is independent of the x and y components and depends only on z.

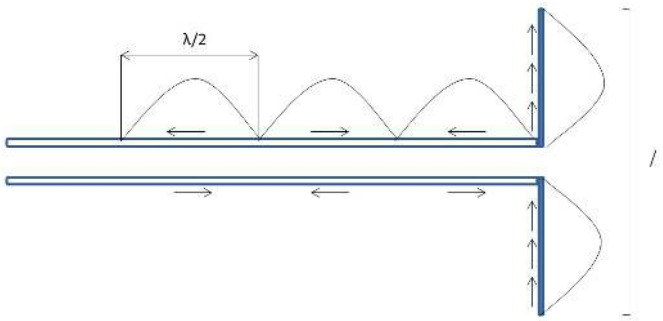

Figure 3.3: Current distribution in balanced waveguide and (full-wavelength) dipole. After reflections at both ends of the dipole, standing current waves are formed. Neighboring waves have 180 degrees phase difference.

spherical coordinates. Consequently, the magnetic field vector lies perpendicular to the plane formed by the electric field vector and the direction of propagation.
In order to find the radiating fields of the dipole, the dipole's length is divided into infinitesimal parts of Δz and then the contribution of each infinitesimal dipole is summed together to produce the dipole's radiation pattern. The radiating electric field of an infinitesimal electric dipole is known by [1], [2] as :

$$dE_\theta \simeq j\eta \frac{k\mathbf{I}(\mathbf{z})e^{-jkr}}{4\pi r}\sin(\theta)e^{jkz\cos(\theta)}dz \tag{3.2}$$

Using equation 3.1 in equation 3.2 and integrating over the length of the dipole, the electric field can be written as :

$$E_\theta \simeq \frac{jk\eta I_0 e^{-jkr}}{4\pi r}\sin(\theta)\left\{\int_0^{l/2}\sin\left[\mathrm{k}(\frac{l}{2}-\mathrm{z})\right]e^{jkz\cos(\theta)}dz + \int_{-l/2}^{0}\sin\left[\mathrm{k}(\frac{l}{2}+\mathrm{z})\right]e^{jkz\cos(\theta)}dz\right\} \tag{3.3}$$

which by using equation A.11 simplifies to :

$$E_\theta \simeq j\eta\frac{I_0 e^{-jkr}}{2\pi r}\left[\frac{\cos\left(\frac{kl}{2}\cos\theta\right)-\cos\left(\frac{kl}{2}\right)}{sin\theta}\right] \tag{3.4}$$

For the half wavelength dipole case ($l = \lambda/2$), the current distribution on the dipole is the one shown in figure 3.4 and equation 3.4 becomes :

$$E_\theta \simeq j\eta\frac{I_0 e^{-jkr}}{2\pi r}\left[\frac{\cos\left(\frac{\pi}{2}\cos\theta\right)}{sin\theta}\right] \tag{3.5}$$

and since $\mathbf{H} = \frac{1}{\eta}\mathbf{z}\times\mathbf{E}$,

$$H_\phi \simeq j\frac{I_0 e^{-jkr}}{2\pi r}\left[\frac{\cos\left(\frac{\pi}{2}\cos\theta\right)}{sin\theta}\right] \tag{3.6}$$

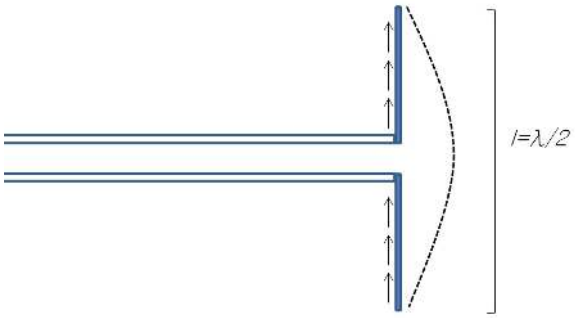

Figure 3.4: Current distribution in a half-wavelength dipole. Observe that current maximum is at the middle of the dipole.

The rest of the field components, namely E_ϕ, H_θ and H_r are zero and E_r can be also assumed zero for far-field observations.

From equations 3.5 and 3.6 it is apparent again that the electric field is oriented only at the $\hat{\theta}$ plane and that there is no dependence on the ϕ variable. So, when the current going through the dipole is an electric current, the radiation pattern is omni-directional and the electric field is vertically polarized. On the other hand, if a magnetic current source is used instead, the radiating fields in far-field are again described by equations A.7 and A.8 with $\mathbf{I}_J = 0$ and $\mathbf{I}_M \neq 0$ hence it is the magnetic field that lies on the $\hat{\theta}$ plane. Consequently, the electric field which is perpendicular to the plane formed by the magnetic field vector and the direction of propagation, lies on the $\hat{\phi}$ plane resulting in omni-directional horizontal polarized radiation pattern.

3.2 Horizontal Polarized Element

As stated in the previous section, a short magnetic dipole can provide omni-directional pattern and horizontal polarization. It is shown in [1] and [2] that an electrically small loop[1] with a constant current throughout the loop has the same far-field function as a magnetic dipole. However, the radiation impedance of a small loop is generally very small and usually smaller than the loss impedance of the wire resulting in very low radiation efficiency, hence small loop antennas are very poor radiators and are not used as transmitting antennas. Moreover, small loops cannot be used together with practical transmission lines (50 Ω or 75 Ω) because mismatch losses would be very high. Increasing the number of turns of the loop or inserting a ferrite core of high permeability within the loop are ways to increase the radiation impedance of a small loop antenna. Increasing the circumference of the loop is another way of increasing the radiation impedance but as the circumference increases, the current at the loop becomes non-uniform and thus

[1]Electrically small is considered a loop with circumference less than 0.1 λ

the maximum radiation shifts to the axis of the loop as the circumference approaches one wavelength.

Novel horizontal polarized antennas inspired by meta-materials have been proposed in [10] and [11] but radiation efficiency and bandwidth are poor. Based on the same concept, innovative loop antennas that keep the current in phase throughout the loop by utilizing the artificially created infinite wavelength transmission lines are proposed in [12] and [13].

Alford and Kandoian [14] presented a way of creating an electrically large loop antenna which has in-phase current distribution throughout the loop hence radiating omni-directionally and horizontal polarized while having good radiation characteristics at the same time. It is proved that having a current distribution similar to that in figure 3.5 then it is possible to get a resonant loop antenna with omni-directional characteristics. Such a printed loop has been patented [15] and used again in [16] but both have a narrow bandwidth.

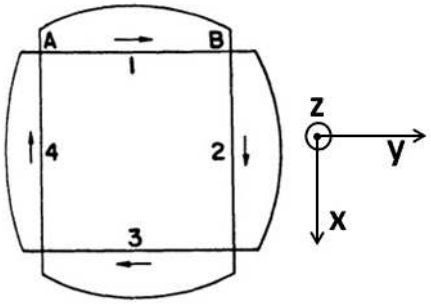

Figure 3.5: Alford antenna current distribution.

Referring back to figure 3.4 one can notice that such a current distribution exists when the length of the dipole is approximately $\lambda/2$ (each of the dipole's arm has $\lambda/4$ length). Thus, by combining 4 half-wavelength electric dipoles that lie in the x-y plane (fig. 3.5) in a loop formation, a horizontal polarized omni-directional pattern is possible. A very good horizontally polarized planar antenna is developed in [17] with a bandwidth of 31% and good omni-directional pattern. It is a deployment of four printed arc dipoles combined with a broadband balun to produce a balanced signal. Unfortunately, the dimensions of the proposed printed loop are rather large hence when placed in a planar array, elements would have been placed far apart resulting in high grating lobes. In [18] and [19] a similar approach is followed but although compact in size, the antennas present narrow bandwidth. In [20] an innovative wideband omni-directional horizontally polarized printed antenna is presented. This antenna steps again on the principle of 4 arc-dipoles combined together. It is composed by 2 parts, 4 arc-dipoles printed in both sides of a dielectric substrate together with a balun structure and 4 parasitic strips which enhance the bandwidth of the antenna. This antenna's size (excluding parasitic strips), bandwidth and radiation characteristics in combination with ease of manufacturing made it a very good candidate and was further investigated.

The horizontally polarized antenna consists of 4 arc-dipoles which are fed by a coaxial cable thus there shall be a balun structure that transforms the unbalanced signal of the coaxial cable to a balanced signal required by a dipole. The balun structure consists of two circular metal patches, each printed in different sides of the dielectric substrate and 4 pairs of tapered lines that connect the circular patches with each dipole arm, thus, the length of the tapered lines and the size of the circular patches significantly affect the impedance matching. Consequently, the arms of the dipole are printed in different sides of the dielectric substrate. The center conductor of the feeding coaxial cable is connected to the upper circular patch whilst the outer conductor is connected to the bottom circular patch. The antenna shape and the corresponding dimensions can be seen in figure 3.6.

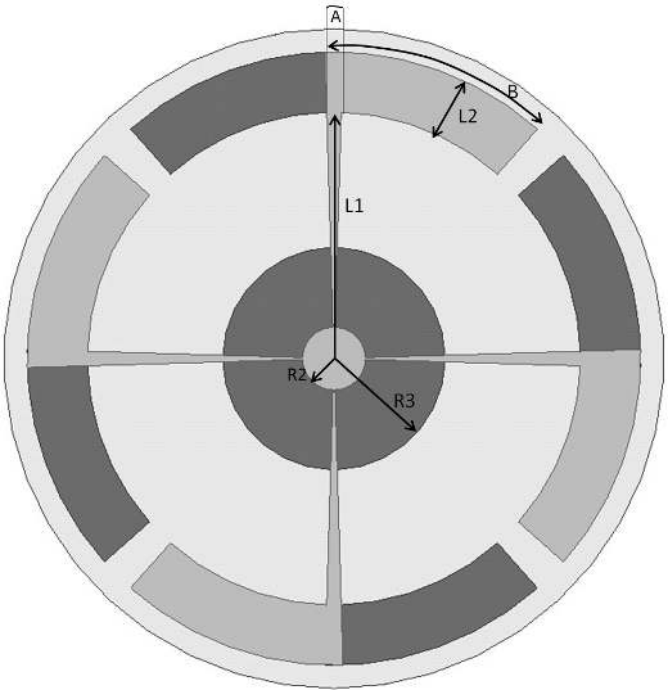

Figure 3.6: Horizontally polarized omni-directional antenna. The metal surfaces are printed in both sides of the substrate. The light gray parts are printed on the top side and the dark gray on the bottom side of the FR4 substrate.

Initially, the antenna was designed and simulated in a commercial 3D EM-solver software with dimensions proposed by [20]. Figure D.1 shows that, without the parasitic elements, the bandwidth of the antenna is indeed narrower than what was expected. Moreover, the center frequency should be shifted lower in the spectrum and that demands the increase of the antenna size (dipole + tapered line length). A parametric analysis on the width of the tapered line (figure D.2) shows that the bandwidth of the antenna can be increased with increasing angle A. Unfortunately, the return loss becomes worse but always remains within acceptable levels. Parametric study results on the length of

Table 3.1: Magnetic dipole's dimensions table

R2 (mm)	4	L1 (mm)	24.5	A (deg)	5.75
R3 (mm)	8	L2 (mm)	7	B (deg)	44.75

the tapered line and the length of the dipole arms are shown in figure D.3. The longer the dipole arm, the lower the resonance frequency of the antenna becomes. Moreover, increasing dimension L2 will also shift the frequency lower in the spectrum (figure D.4). Unfortunately, since the space available is limited [1], concessions shall be made regarding the return loss of the antenna.

After proper tuning of the dimensions discussed above and adjustment of the circular patches radius, the final geometry parameters of the proposed omni-directional HP antenna are presented in table 3.1. The antenna is to be printed on a typical FR-4 board with dielectric constant 4.4, loss tangent of 0.02 and 1.6 mm thickness.

S11 values are shown in figure 3.7. S11 is less than -10dB between 1.75 and 2.3 GHz, giving a bandwidth of 550 MHz ($\approx 27\%$). Radiation patterns of the proposed antenna are given in figure E.1 for three different frequencies, 1.7, 2 and 2.2 GHz. There, it is seen that the antenna produces a very well omni-directional radiation pattern with negligible rippling in the azimuthal cut and very well suppressed cross polar (XP) components. The radiation efficiency of this antenna is 85%, 92% and 92% at these three frequencies respectively. In figure 3.8 the current distribution of the antenna is presented and can be verified that the current per dipole is distributed similar to [14] or figure 3.5 and is in phase throughout the whole antenna.

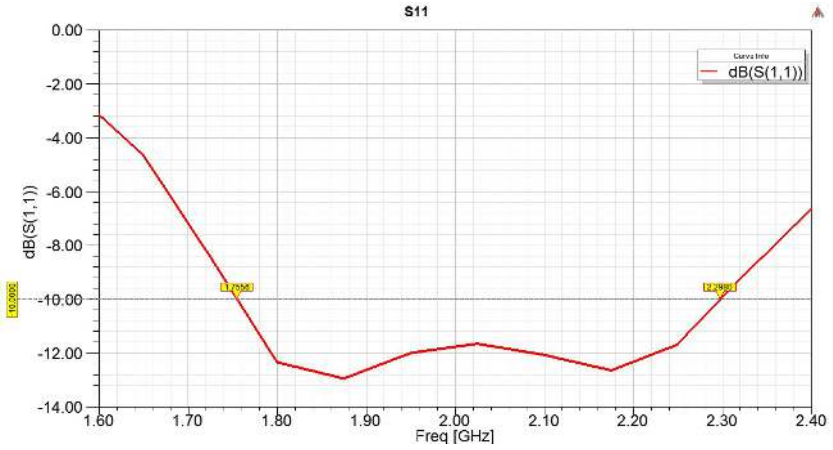

Figure 3.7: Return loss of the proposed antenna.

[1] The elements shall be placed in an array so the spacing between them should be $\leq .5\lambda$

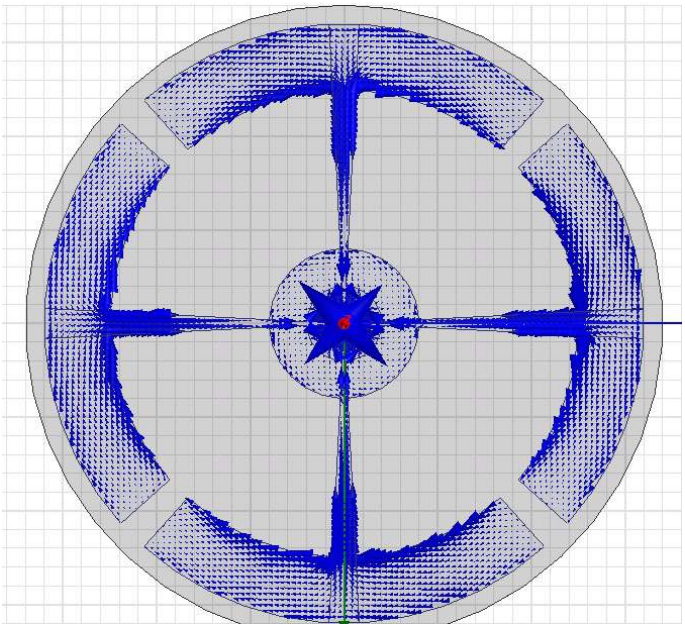

Figure 3.8: Current distribution on the HP omni-directional antenna.

3.3 Horizontally polarized Array

For the horizontal polarized component, 4 magnetic dipoles shall be positioned together in an a 2x2 array. Since the diameter of the loop is 2*(L1+L2) = 63 mm, the minimum maximal-distance between elements will be at least[2]: $\sqrt{2 * (2 * (L1 + L2))^2} \approx 89\ mm$ as can be understood by Figure B.5 and its accompanying caption. This translates to 0.65λ ,0.59λ and 0.505λ at 2.2, 2 and 1.7 GHz respectively hence, inevitably, the radiation pattern of the array will not be the desired one. Moreover, it should be considered that the array elements should not be placed very close together in order to get as low coupling levels as possible.

When such an array was simulated, it was observed that indeed, because of the large distance between the elements, the radiation pattern was not the desired one. At the elevation-plane the maximum radiation did not lie at $\theta = 90^o$ as desired but have diverged around 55^o hence the maximum radiation happened at $\theta_1 = 35^o$ and $\theta_2 = 145^o$ instead, as shown in figure 3.9(b).

To fix this, two metallic circular planes are introduced above and below the plane of the array so that waves radiated at angles θ_1 and θ_2 will reflect to the ground planes and then they will combine again at $\theta = 90^o$ plane as presented in figure 3.9(a). The distance between the middle plane and the ground planes along with the ground plane radius have been tuned to 67.5 and 70 mm respectively so that waves combine is a proper way throughout the bandwidth of interest (1.7 - 2.2 GHz). The ground planes are also chosen to be printed on a board. A metal surface will be printed in both sides of the

[2]The diagonal elements of the array.

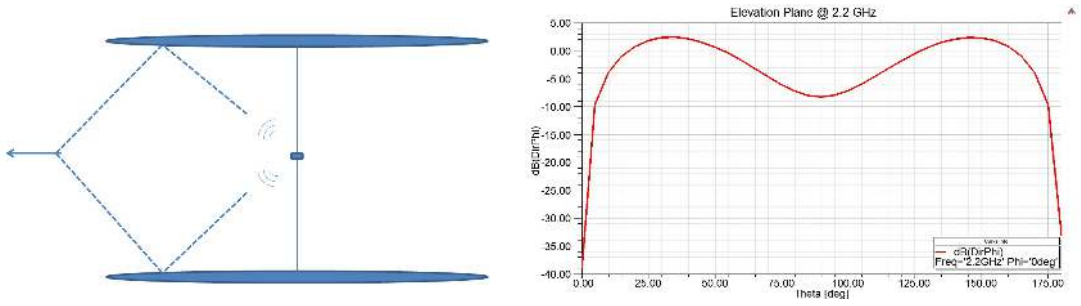

(a) (b)

Figure 3.9: Introduction of ground planes (left) and θ-cut of the array without ground planes (right).

FR-4 board.

In order to support the structure, the three planes are connected together by a central hollow metal tube which will also serve as the passage for any feeding cables. The tube was chosen to be metallic so that any passing cable will not disrupt the electromagnetic characteristics of the antenna. In other words, by passing the cables through the metal tube, the actual radiation pattern of the antenna would be very close to what has been simulated.

The final horizontal polarized array structure is presented in figure 3.10(a). Detailed figures and dimensions are presented in appendix B. Figure 3.10(b) shows the S-parameters of the 4 elements array when one element is excited and all the others are terminated in 50Ω. The array achieves a good return loss between 1.7 and 2.2 GHz but coupling is just out of specification. In particular, adjacent elements have 12 dB of coupling while coupling between diagonal elements is as low as 20 dB.

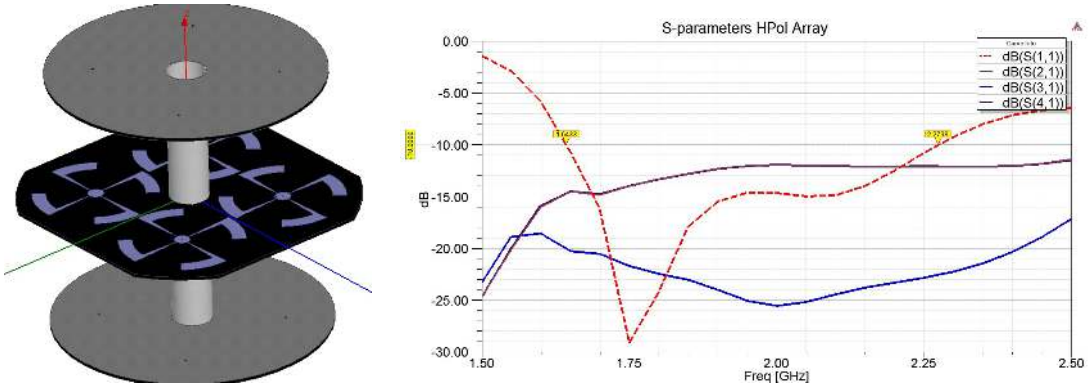

(a) (b)

Figure 3.10: Horizontal Polarized array structure (left) and passive S-parameters of the array (right).

Radiation patterns when in OMNI mode are presented in figure E.4 where can be seen that the antenna produces good omni-directional patterns with well suppressed cross polar components in all frequencies. Maximum azimuthal rippling is at 3dB and maximum cross polar component is at -15 dBi. Figure E.5 present the radiation patterns when the antenna is excited in SECTOR mode. Mainlobe / Sidelobe difference is around 7.5 db ($> 10db$) but this is inevitable because of the large spacing between the elements. However, it is possible to increase this difference by tuning the phase excitation as it is shown later in this report.

3.4 Vertical Polarized Element

As described in section 3.1, omni-directional vertical polarized radiation fields can be produced by electric dipoles. A lot of work has been done on printed electric dipoles and planar dipoles array such as in [21], [22], [23], [24] but integrating this kind of dipoles in the current structure is a tricky procedure. Instead, since there are ground planes in the structure already, a concept based on monopoles was investigated.

A monopole antenna is an electric conductor above a ground plane and usually is a quarter of a wavelength in size, for instance the inner conductor of a coaxial cable that extends above a ground plane. According to imaging theory the radiated fields of a monopole above an infinite perfect ground plane are equal to those of an electric dipole for the same region and are zero below the plane, as is also explained by figure 3.11. The same goes for the radiation pattern but the directivity of the monopole is 3 dB higher than that of a dipole since it radiates only in half-space.

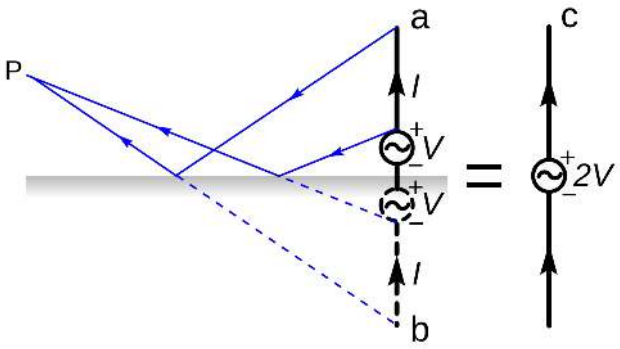

Figure 3.11: This figure shows that a monopole above an infinite perfect ground plane has the same radiating fields, in the space above the plane, as an electric dipole with twice the voltage.

A monopole's maximum radiation happens at x-y plane when the monopole is above an infinite perfect ground plane (figure 3.12(a)). In reality though, ground planes are of finite size and this fact strongly affects the radiation pattern. When the size of the ground plane is electrically very large (more than 3λ in diameter), then the monopole radiates

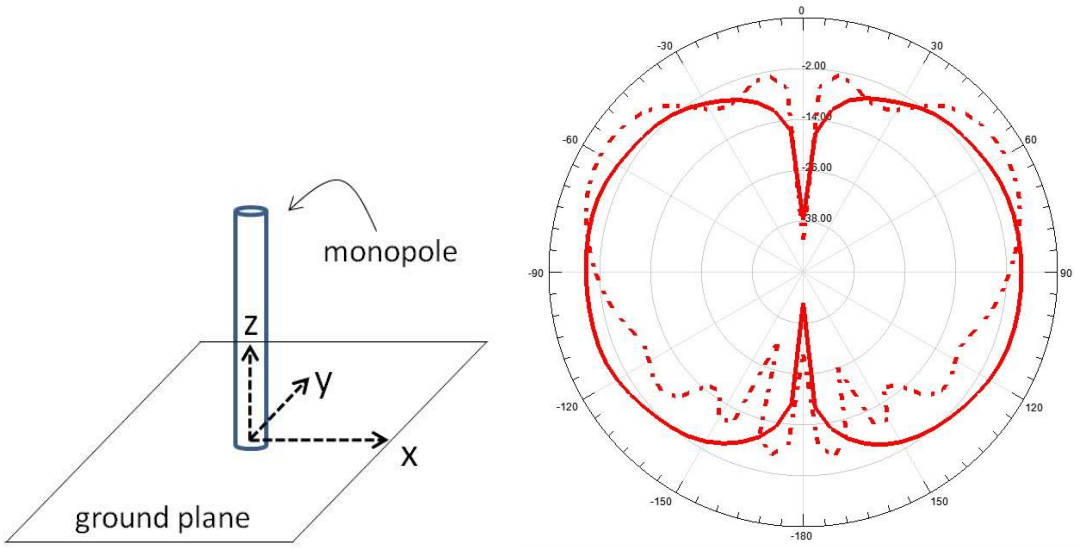

(a) (b)

Figure 3.12: Left: Monopole on z-axis with ground plane lying on x-y plane. Right: Ground plane size effect on monopole's radiation pattern. Presented for ground diameter of approximately $\lambda/2$ (solid line) and 2.5λ (dashed line).

mainly above the x-y plane but the maximum radiation shifts away from x-y plane. Finite size of ground planes results in diffraction of the radiated power towards any direction and eventually part of the power is radiated below x-y plane also. In particular, as the ground plane become electrically very small[1] then the radiation pattern approximately matches that of a half-wavelength dipole as can be seen in figure 3.12(b).

Based on the above notion, an array of monopoles can be used above one of the existing (electrically) small ground planes in order to provide the vertical polarization. However, since the ground plane is electrically smaller at 1.7 GHz than at 2.2 GHz, radiation patterns will, in principle, differ in the θ plane. For this reason, the exact same array of monopoles will also be used on the second ground plane, symmetrically as of the x-y plane, so that the combination of the two arrays will always give an omni-pattern with the maximum radiation at $\theta = 90^o$. Additionally, inserting a second monopole array to the antenna will also increase the available number of elements hence a higher diversity gain is possible to be achieved and extra flexibility in terms of MIMO can be provided. In order for the combined radiation pattern to be omni-directional with maximum radiation at $\theta = 90^o$ the arrays should have a phase difference of 180^o so that the radiated waves combine constructively in the area between the two ground planes.

Monopole antennas can be implemented by planar radiating elements standing above a ground plane and radiator sheets can have many different shapes [25] which is some cases ([26], [27]) can reach up to ultra-wide bandwidth. For a rectangular shaped radi-

[1] Half a wavelength in diameter for instance

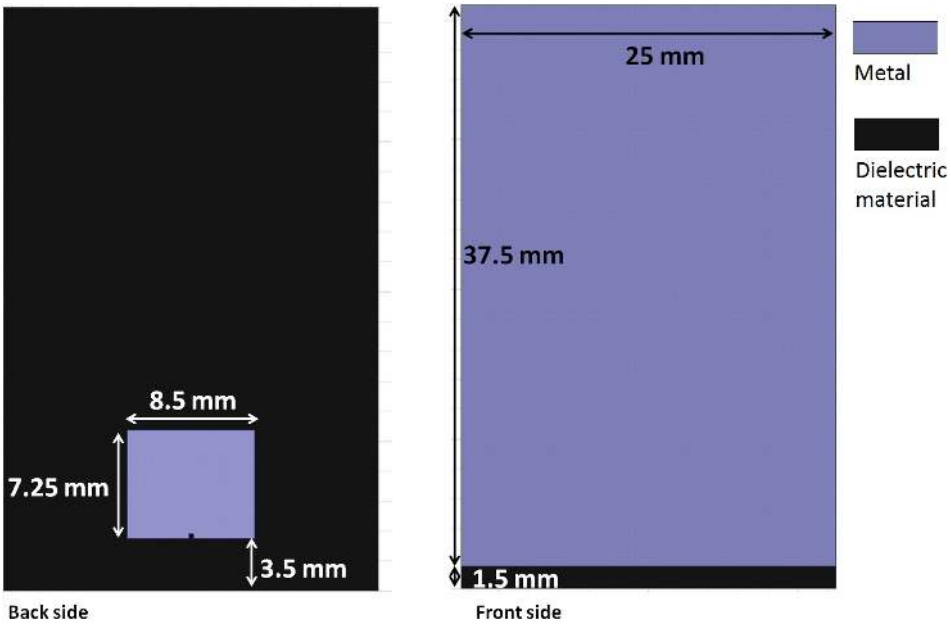

Figure 3.13: Element to be used as monopole together with its dimensions. Feeding of the monopole is done by a coaxial cable whose inner conductor shall be connected (soldered) to the small patch on the monopole's back side.

ator, the length of the sheet will determine the resonance frequency while its width will enhance the bandwidth. It has also been observed in [28] that the distance between the radiating element and the ground plane significantly affects impedance matching.

The monopoles to be used in the current antenna structure are thus designed as rectangular metal sheets printed on 1.6 mm - width FR4 substrate of 4.4 dielectric constant. The length of each sheet is chosen as such to provide the right resonance frequency and the width is adjusted so that the impedance matching is good throughout the band of interest. The feed-gap is also tuned to provide good impedance matching. The monopole shall be fed by a coaxial cable, thus, a small probe-fed patch which is electromagnetically coupled to the radiator is printed on the other side of the dielectric substrate as proposed by [29], hence the inner conductor of the cable shall be attached to the probe patch while the outer conductor will be connected to the ground plane. The monopole element is presented in figure 3.13. It has also been observed that the ground plane's size also affects the impedance matching. This is why a circular corrugation is introduced on the ground planes (see figure 3.15) so that both the monopole elements are well matched and the ground planes are large enough to refocus the horizontal polarized pattern.

The S-parameters for the monopole array are shown in figures 3.14(a) and 3.14(b) for impedance matching and coupling respectively. It can be seen that the array presents a good impedance match ($>$ 11dB) between 1.7 and 2.2 GHz. Coupling between 2 adjacent elements is at 14 dB and under 18 dB between any other element in the array.

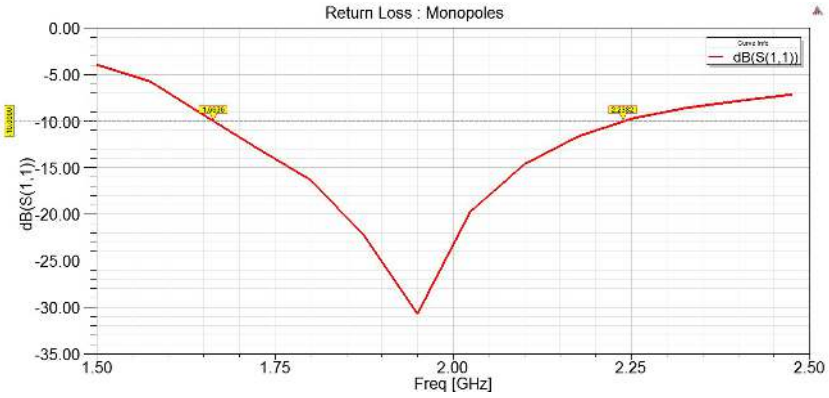

(a)

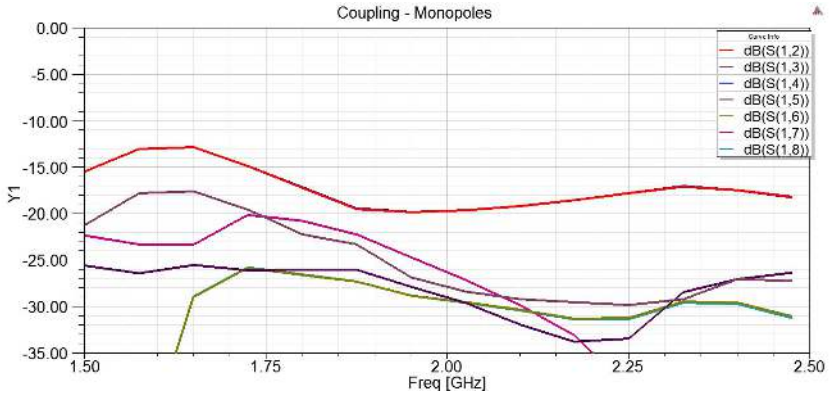

(b)

Figure 3.14: Passive S-Parameters of the monopole array. Return loss (up) and coupling (down).

Radiation patterns when in OMNI mode are presented in figure E.6 where can be seen that the antenna produces very good omni-directional patterns with well suppressed cross polar components in all frequencies. Maximum azimuthal rippling is at 1.1dB and maximum cross polar component is at -30 dBi. Figure E.7 present the radiation patterns when the antenna is excited in SECTOR mode. Mainlobe / Sidelobe difference is between 6.5 and 10 dB and the 3-dB beamwidth (full angle) in the ϕ-plane is between 90^o and 75^o for the frequency range 1.7 to 2.2 GHz. As for the magnetic dipoles case though, it is possible to increase the mainlobe/sidelobes difference by tuning the phase excitation. XP components can get as high as -1.5 dBi when is SECTOR mode.

3.5 Dual Polarized Antenna

The final dual polarized antenna array is eventually created by a combination of what has been described above. It is composed by three planes of which the middle plane contains

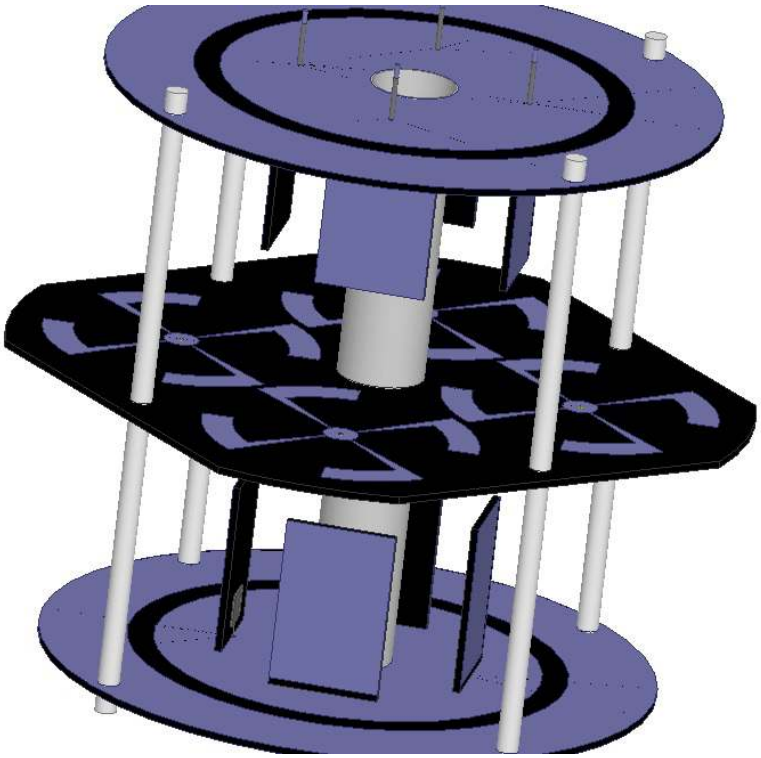

Figure 3.15: Dual Polarized Antenna Array.

the magnetic dipoles and the other two are ground planes with mounted monopoles in a circular array configuration. Each pair of monopoles that lie on the same vertical axis (mirrored monopoles) can be considered as one electric dipole hence, on the whole, there are two orthogonal polarized 2x2 arrays formed in accordance to the initial idea presented in figure 3.1. The three planes are pooled by a hollow copper tube which also serves as the passage for the feeding cable. Four supporting nylon rods will also be used on the prototype in order to make the whole structure even more robust. The final antenna is presented in figure 3.15 and detailed figures and dimensions are given in appendix B. The volume of the antenna is approximately 2.78 dm^3.

It would be expected that since the elements have very well suppressed cross polar components, the interaction between orthogonal polarized elements should be very small and thus, their individual characteristics should not change when combined under one structure. Figures D.5 and D.6 prove precisely this fact and it is evident that the return loss for both vertical and horizontal polarized elements is almost unchanged. Same holds for the coupling values. An interesting thing to be mentioned is that coupling between elements of different polarizations is, indeed, weak ($>$ 23dB).

Radiation patterns when in OMNI mode are presented in figure E.8. The antenna produces nice "donut shaped" radiation patterns for both polarizations. The radiation efficiencies of the two orthogonal polarizations (logical ports) are [95% 93% 91%] and

Table 3.2: Optimal Phase excitations

Freq	Horizontal Polarization	Vertical Polarization
1.7 GHz	[0 50 177.5 50.5]	[0 91 224 90]
2 GHz	[0 80 216 80.5]	[0 70 238 70]
2.2 GHz	[0 66 205 65]	[0 66.5 230 65.5]

[78% 84% 85%] for vertical and horizontal polarizations and frequencies 1.7, 2 and 2.2 GHz respectively. SECTOR mode patterns are presented in figure E.9. The phase excitations have been optimized through a numerical-solving software in order to produce the lowest possible sidelobe levels and optimal excitations are presented in table 3.2. For these optimal excitations, the vertical component produces good sector beams with 3dB beamwidth angle (ϕ plane) ranging between 73^o and 76^o throughout the bandwidth of interest and mainlobe/sidelobes differences more than 10dB. The horizontal polarized beam is affected by the cross polarization produced by the monopoles and hence the beams are a bit skewed. Additionally, although the beam at 2.2 GHz present a good beamwidth and mainlobe/sidelobes levels, it is required a wider beam at 1.7 and 2 GHz in order to keep the mainlobe/sidelobes difference in acceptable levels which reach up to 8dB. Details about elevation and azimuth beamwidths are given in table E.1 .

3.6 Prototype

A prototype of the above antenna has been manufactured and its characteristics in terms of S-parameters, radiation patterns and MIMO capacity have been investigated. The three different layers are all printed on FR-4 substrate and the ground planes (outer layers) have metal surfaces printed on both sides of the substrate and are connected by vias. The eight monopole patches are also printed on FR-4 substrate and have an extended substrate size to provide some tuning flexibility. The final antenna prototype is presented in figure 3.16.

For feeding the magnetic dipoles, the inner conductor of the cable is soldered to the top surface while the outer conductor is soldered to the bottom one, as presented in figure B.6. The four feeding cables are driven to the lower part of the antenna through 4 holes on the central copper tube. The monopoles are first glued to the ground planes and then the inner conductor of a coaxial cable is soldered to the feeding patch while the outer conductor is soldered to the outer surface of the ground plane as presented in figure B.7. The four cables feeding the top monopoles are driven through the hollow tube to the lower part of the antenna, so, the feeding of every element can be done easily from the bottom side of the antenna (Figures B.8, B.9). Each vertical dipole is formed by combining each monopole pair (top and bottom) through a 180^o power splitter. The four magnetic or electric dipoles are combined together with a 4-way power splitter. Four threaded nylon rods together with plastic nuts are inserted in order to easily fix the planes in position and make the whole structure more robust.

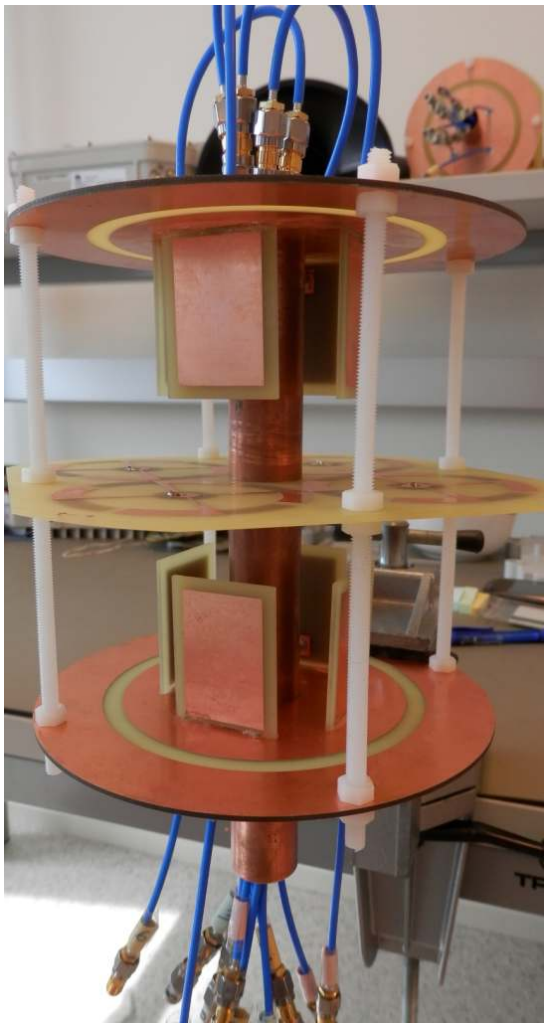

Figure 3.16: The manufactured prototype

The S-parameters measurements taken in a 2-port vector network analyzer show very good agreement with the simulations. Figures D.7 and D.8 presents the return loss for the magnetic dipoles and the monopole sheets. The monopole impedance bandwidth is shifted towards lower frequencies but this is probably because of the extended substrate used which increased the electrical length of the monopole. To verify this, the simulated extended monopole return loss is also plotted in the same figure.

Coupling plots are presented in figures D.9-D.11 where can be observed that highest coupling between magnetic dipoles is at 12.5 dB and 13.5 dB between monopoles. Cross coupling between horizontal and vertical polarized elements is at 23 dB. Again, there is very good agreement between simulations and real measurements.

The antenna was also measured in the anechoic chamber (figure 3.17) and results for azimuth and elevation cuts are presented in figures E.10 - E.12. The measured radiation

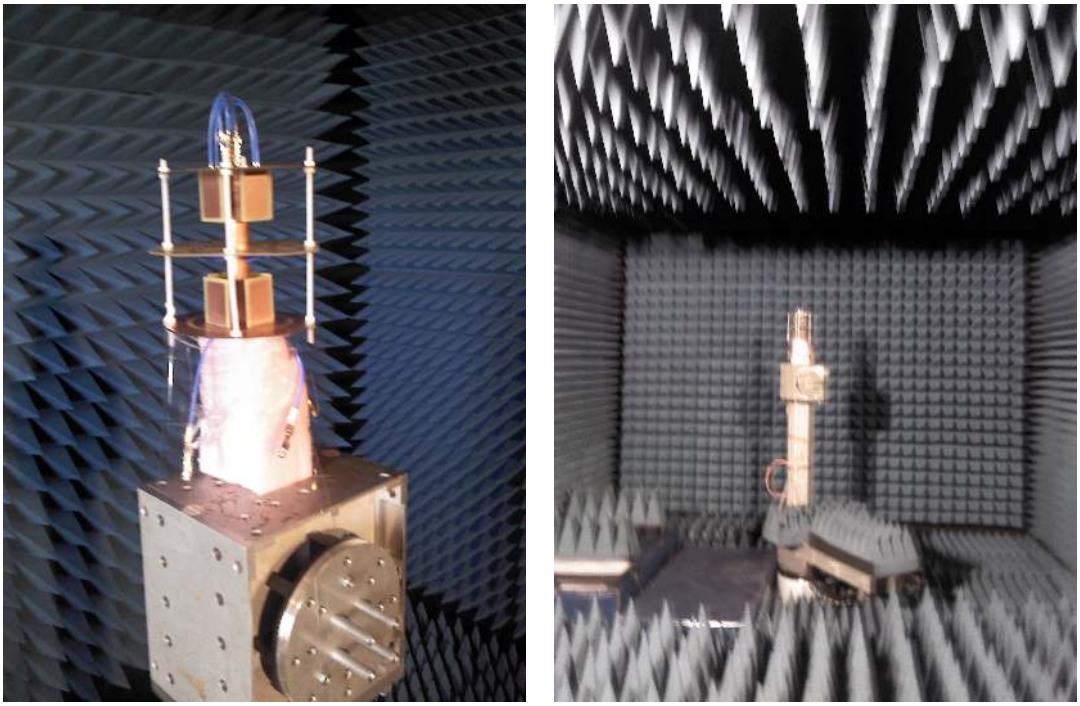

(a) (b)

Figure 3.17: Measurement of radiation patterns in the anechoic chamber

patterns presented in these figures are normalized to the mean power (for OMNI mode) and to the directivity (for SECTOR mode) of the corresponding simulated patterns. The radiation patterns that the prototype produced are generally very close to the simulated ones. One thing to be noticed is that the measurements showed very high cross-polar components in comparison to the simulated values but it is believed that this mainly happens due to imperfections both in the antenna assembly and the antenna mounting in the chamber. Azimuth rippling is, also, a little bit higher than simulated values. For easy comparison, tables 3.3 - 3.6 present aggregated values of simulated and measured values.

Table 3.3: Simulated azimuth rippling values and elevation 3dB beam-width angles when in OMNI mode.

Freq	Horizontal		Vertical	
	Az.Rippling	3dB BW	Az.Rippling	3dB BW
2GHz	1.5dB	68^o	0.5dB	56.5^o
2.2GHz	3dB	59^o	0.8dB	50^o

Table 3.4: Measured azimuth rippling values and elevation 3dB beam-width angles when in OMNI mode.

Freq	Horizontal		Vertical	
	Az.Rippling	3dB BW	Az.Rippling	3dB BW
2GHz	2.7dB	51^o	1.65dB	57^o
2.2GHz	3.35dB	34^o	2.58dB	55^o

Table 3.5: Simulated Main-lobe/Side-lobe difference and azimuth 3db-Beamwidth values when in SECTOR mode.

Freq	Horizontal		Vertical	
	Main/Side-lobe difference	Azimuth 3dB-BW	Main/Side-lobe difference	Azimuth 3dB-BW
2GHz	6dB	90^o	7.4dB	80^o
2.2GHz	7.6dB	74^o	6.3dB	74^o

Table 3.6: Measured Main-lobe/Side-lobe difference and azimuth 3db-Beamwidth values when in SECTOR mode.

Freq	Horizontal		Vertical	
	Main/Side-lobe difference	Azimuth 3dB-BW	Main/Side-lobe difference	Azimuth 3dB-BW
2GHz	6.1dB	75^o	6.4dB	81^o
2.2GHz	7.3dB	76^o	6dB	75^o

4

Diversity and MIMO

As explained in section 2.4, multiport antennas can be used in order to mitigate the effects caused by a multipath environment. The developed antenna can support either 12-ports (8 monopoles and 4 magnetic dipoles), 8-ports (4 electric and 4 magnetic dipoles) or 2 logical ports, one for each polarization (figure 4.1). Antenna diversity and channel capacity are calculated both in a reverberation chamber which emulates a rich isotropic multipath (RIMP) environment and in appropriate software (ViRM-Lab) in order to determine theoretical limits. More ports are expected to have better performance but will result in creation of complex systems whilst fewer ports will result in lower performance but simpler architectures. Additionally, the antenna is simulated in Huawei's channel emulator (ACE) in order to be investigated whether different antenna patterns give different performance in various space distribution of mobile users.

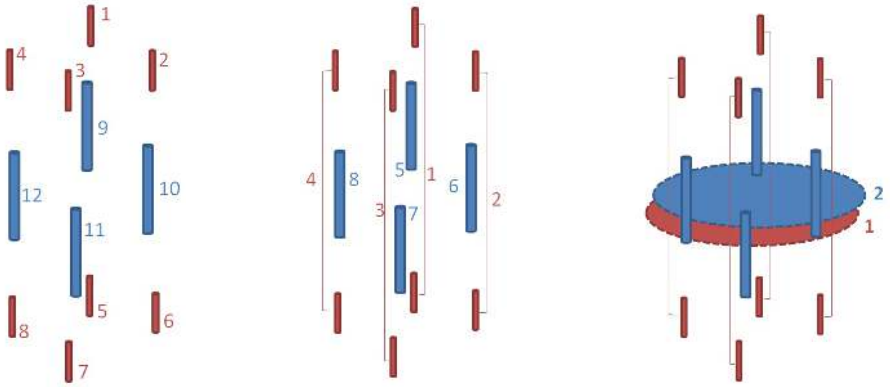

(a) (b) (c)

Figure 4.1: Diversity modes : 12-port, 8-port and OMNI/SECTOR modes

4.1 Antenna diversity simulations

Antenna diversity can be characterized in two extreme reference environments [30]; the rich isotropic multipath (RIMP) and the 3D-random line of sight (R-LOS) environments. In a RIMP environment waves of different amplitude and phase arrive at the antenna with a uniform angle of arrival (AoA) over all directions in space, therefore the statistical properties of the received voltages are independent of the orientation of the antenna. This can imply that radiation patterns in a RIMP environment play a minor role compared to a traditional LOS. The other extreme environment is when there is a dominant LOS component on the incoming signal. However, if the user position arbitrariness is taken into account together with the random orientation of a mobile device then a LOS environment with 3D arbitrariness can be defined.

In this work two extra reference environments are introduced. The Half-Sphere environment (HS) is very similar to the RIMP but the angle of arrival of the incoming waves is limited to $[-\pi/2\,\pi/2]$ interval on azimuth plane. In addition, Half-Random-LOS (HR-LOS) it is an R-LOS environment where the waves arrive only at the $[-\pi/2\,\pi/2]$ interval on azimuth plane. In this way, multipath and random LOS environments where the antenna is mounted on a wall or when users are positioned at a street facing the antenna for instance, can be modeled. The four different environments are explained graphically in figure 4.2.

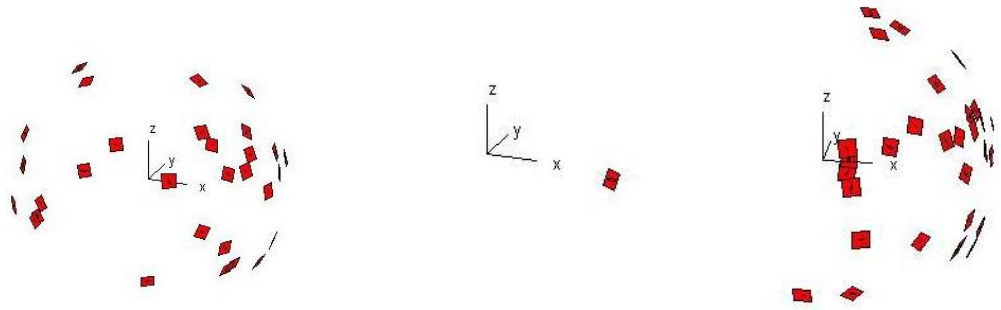

(a) (b) (c)

Figure 4.2: Different diversity environments; RIMP, R-LOS and HS respectively. In R-LOS environment the wave can arrive from every possible direction while in HR-LOS, the wave can only arrive in the interval $[-\pi/2 \quad \pi/2]$.

Diversity gains in RIMP and R-LOS are defined in [31] and [32] respectively and are distinguished in apparent and effective gains. Apparent gain is the difference on received power between the combined signal and the signal on the strongest branch of the multiport antenna while effective gain is the difference between the combined signal and an ideal one-port antenna taken at the same cumulative probability level, which is normally at 1%. In a RIMP environment the in-phase and quadrature components of the signal are Gaussian distributed hence the magnitude will be Rayleigh distributed. This means that the cdf of each branch of the antenna should follow the theoretical Rayleigh

distribution. The same should hold for the HP environment but not exactly for R-LOS environments.

Initial diversity simulations are done in ViRM-Lab [33], a ray-based simulation tool which enables users to study the performance of arbitrary user-defined multiport antennas located in user-specific multipath environment and it works by defining the multiport antenna by each element's embedded radiation pattern. Radiation patterns of the designed antenna produced by the 3D-EM simulator software are imported to ViRM-Lab in order to calculate diversity gains and channel capacity for 12-port, 8-port and 2-port cases. For the 2-port case both OMNI and SECTOR modes are considered.

Table 4.1: Diversity gains in dBr for different multiport modes of the designed antenna in four different environments @ 2 GHz

Used Ports	RIMP		R-LOS		HS		HR-LOS	
	SC	MRC	SC	MRC	SC	MRC	SC	MRC
12	19.88	26.65	19.92	27.05	18.49	25.08	20.8	27.9
8	18.27	23.72	18.85	24.45	17.518	22.9	13.65	19.77
2-OMNI	9.05	10.49	2.91	3.28	9.05	10.54	2.66	3
2-SECTOR	8.8	10.32	5.7	7.33	11.19	12.73	8.27	9.79

Table 4.2: Reference measurements in a RIMP environment using ideal sources @ 2 GHz

Used Ports	Reference Measurement	
	SC	MRC
12	20.08	26.8
8	18.42	23.85
2-OMNI	10.2	11.8
2-SECTOR	9.85	11.34

Table 4.1 presents aggregated results of the different multiport modes at 2 GHz central frequency. The voltages at each port of the antenna are corrected by the total radiation efficiencies of each element and for each case the effective gain (in dBr)[1] is presented for both Selection Combining (SC) and maximum ratio combining (MRC). For comparison, table 4.2 presents the results of reference measurements which are made in a RIMP environment using ideal incremental electric and magnetic sources for 12, 8 and 2-OMNI cases and two orthogonal polarized ideal sector beams for the 2-SECTOR case.

Results in Table 4.1 show that the antenna can achieve a very high diversity gain

[1]dBr is the gain in dB between the reference antenna and the combined signal.

when operated under 12- or 8- port mode where the gain can reach up to 26.5 dBr when MRC is used. As expected, when in OMNI mode the antenna achieves exactly the same gain in RIMP and HS environments since regardless where the waves come from, the antenna will sense each wave the same. An interesting result is derived by comparing the gains achieved in HS and HR-LOS environments against RIMP and R-LOS for the 2-SECTOR mode where it is seen that the gain can be increased by more than 2.5dB when a sector beam towards the direction of the incoming waves is used. And this gain is expected to increase even more when there is a LOS component together with the multipath waves (Rician).

Table 4.3: SIMO (1×X) spectral efficiencies (bits/s/Hz) at 15 dB SNR

Used Ports	RIMP	R-LOS	HS	HR-LOS
12	7.28	7.31	7.25	7.3
8	6.6	6.64	6.56	6.45
2-OMNI	4.33	4.34	4.33	4.25
2-SECTOR	4.3	3.94	5.01	4.8

Table 4.3 presents calculated mean capacities (bits/s/Hz) for the 4 different modes in the same four environments. The capacity is calculated at 15 dB SNR considering one transmit antenna and the mean over all channel realization is taken. Again, there is an increase in spectral efficiency when a sector beam is used in a HS or HR-LOS environment compared to an omni-directional pattern.

4.2 Reverberation Chamber

Measurements have been also performed in a reverberation chamber (RC) which is well known to produce a RIMP environment [34]. RC is a shielded metallic chamber with mechanically stirred parts which generates a uniform multipath environment and can provide a statistically repeatable laboratory-produced environment for multiport antenna characterization.

Measurements were performed in 'Bluetest AB' premises on a RTS60 chamber which can support frequencies between 650 and 6000 MHz. Initially, a measurement of the reference antenna is taken with the antenna under test (AUT) inside the chamber (figure 4.3). Then, measurements of the AUT's ports are taken with the reference antenna inside the chamber in order to have the chamber equally loaded as for the reference measurement. A 4-port VNA is used to collect the voltages at the antenna ports but since one of the VNA's port is always connected to the source antenna, 3-ports where available for tracking receiving ports. Measurements were taken by using 12-, 8-, 2-OMNI and 2-SECTOR modes between 1.7 and 2.2 GHz and diversity gain results, correlation values and MIMO capacities which are calculated according to [35] are presented in Table 4.4.

Figure 4.3: RC set-up

Table 4.4: Diversity gains and correlation values for different multiport modes of the designed antenna measured in Reverberation Chamber. The right part of the table presents the MIMO channel capacities for 1, 2 and 4 transmitting antennas at 15 db SNR level.

Used Ports	Diversity gain		Correlation	MIMO capacity (bits/s/Hz)		
	SC	MRC		1×X	2×X	4×X
12	16.5 - 17.5	23.5 - 24.5	< 0.05	8.07	14	23.45
8	15 - 16	20.5 - 21.5	< 0.05	7.2	12.15	19.45
2-OMNI	6.5 - 8	8 - 9	< 0.03	4.65	6.53	7.35
2-SECTOR	6.5 - 7.5	8 - 9	< 0.03	4.61	6.44	7.25

Radiation efficiency values measured in the RC are lower than what has been simulated in the 3D-EM software and this is probably the reason why diversity gains are lower than what has been simulated in ViRM-Lab. In particular, radiation efficiencies measured in the reverberation chamber are between -1 and -2 db for the 12-port mode while it degrades up to -3.5 dB for the 2-port cases. It is believed that the introduction of power splitters to the antenna in order to divide power to more than one elements (8- and 2- modes) is mainly responsible for this radiation efficiency degradation. Neverthe-

less, diversity gains achieved are still very high and can reach up to 24.5 dB when all 12 ports are used. Spectral efficiency can reach up to 23.45 bits/s/Hz in an 4×12 MIMO system. It can also be seen that values of both diversity gain and capacity are quite close for OMNI and SECTOR modes; a fact that reinforces the notion that radiation patterns play a minor role in a RIMP environment. Diversity gain and capacity plots taken out of the RC measurements are presented in appendix C.

4.3 Channel Simulations

Channel simulations have been performed in Huawei's channel emulator 'ACE'. In brief, the designed antenna is used as a base station (BS) multiport antenna within a network cell where mobile users with specific location and velocity are spread. For each mobile user a channel matrix **H** between the transmitter and the receiver is calculated based on the Winner II channel model [36] and a capacity analysis is done and conclusions can be drawn by observing the average values of capacity over a large number of mobile users. Simulations have been done for an urban single cell network, that is, there is no interference between neighboring cells or between mobile users while mobile users' antennas are composed of one vertically and one horizontally polarized isotropic radiator.

In order to investigate the performance of the antenna, simulations have been performed in the same way as for diversity gain measurements; that is 12-, 8-, OMNI and SECTOR modes and initially it was investigated whether there is any difference in performance between 2-port antennas :

- having one electric and one magnetic dipole co-centered (dual polarized)
- having 2 electric dipoles in right angle
- having 2 electric dipoles placed λ distance apart

and as can be observed from figure C.9 the dual polarized dipole gives in total better SNR than the other two cases and an increase in spectral efficiency of more than 1 bps/Hz compared to the others.

The main goal of the simulations was to be investigated whether in an urban environment there is better performance when a directive beam towards a collection of users is used instead of an omni-directional antenna. Therefore, capacity analysis has been done for a collection of users confined in an certain angle ξ within the network cell as figure 4.4 shows.

The final results are presented in figure 4.5 from which it can be seen (blue dashed line) that, as expected, the mean capacity stays on the same level regardless of the coverage angle ξ since the location of a mobile user plays no role when the antenna is used in OMNI mode as it serves the whole cell equally with it's omni-directional pattern. On the other hand, it can be seen (red dashed line) that the mean capacity is increased when the antenna is used in SECTOR mode and users are confined in antenna's beam. It can also be noted that the sector beam saturates around its 3dB-beamwidth angle (75 - 85 degrees) where at that point provides 2 bps/Hz extra than the OMNI mode. When

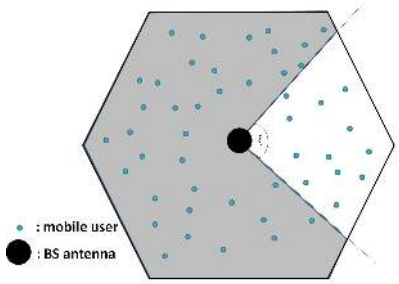

Figure 4.4: Depiction of the coverage angle in a mobile cell.

the antenna is used in 12- or 8-port modes it always outperforms 2-port cases since it adapts with the optimal way to each user. Additionally, a capacity analysis for a quite narrow beam has been also performed (black dashed line) and is presented in the same plot. From the results of above analysis it can be concluded that although in a multipath environment it still make sense to direct the power of the antenna towards the location that users are located!

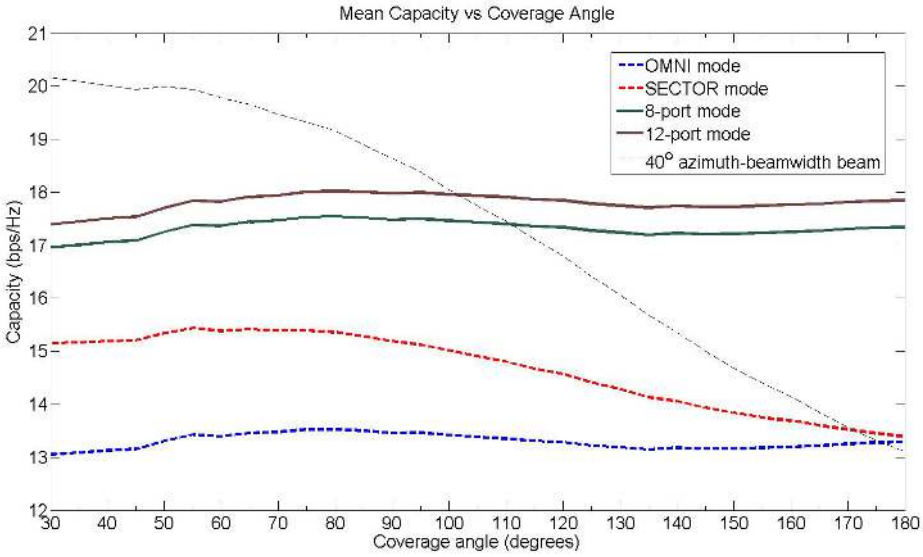

Figure 4.5: Capacity vs Confinement angle

5

Conclusions and Future work

5.1 Conclusions

A multiport antenna, intended for base station use, has been designed and a prototype has been implemented. The antenna is composed of 12 elements in an array configuration, can provide both horizontal and vertical polarizations and it is also shown how it can operate under different modes. Special interest presents the 2-port case, where the elements are configured in such a way that the antenna provides a two logical-port interface. In particular, the vertically polarized elements are combined in order to provide one vertically polarized radiation pattern and the horizontally polarized elements are combined such that they give one horizontally polarized radiation pattern. In this way, the two orthogonal polarizations can provide two very uncorrelated ports and thus being able to transmit two different streams of data at the same time; one through each polarization.

In addition, since the elements are positioned in an array configuration, they can provide an additional feature; beamforming. Hence, by properly selecting the phase excitation of the elements in the antenna, the radiation pattern (of each polarization) can vary between omni-directional or sector beam which, additionally, can be stirred towards four directions ($\pm x$, $\pm y$). Diversity and channel simulations has shown that even in a multipath environment, directing the energy towards the direction where the users are located can increase the performance of the link. Hence, the designed antenna could be used in various environments regardless if it is preferable to have an omni-directional pattern or a sector beam.

The developed antenna presents a good impedance match (VWSR < 2) between 1.7 and 2.2 GHz giving a bandwidth of around 25%. Coupling between neighboring elements is up to 12.5dB and coupling between cross polarized elements is as low as 23dB. Simulated radiation patterns show an omni-directional rippling of maximum 3dB and when in SECTOR mode, a mainlobe/sidelobes difference which at minimum is at 8

and 10 dB for the horizontal and vertical polarization respectively.

Measurements on the prototype regarding impedance match and coupling show great similarity with the simulated values. The radiation patterns were also measured in an anechoic chamber and the results are very close to what has been simulated. Additionally, characterization of the antenna in terms of diversity and MIMO capacity has been performed in a reverberation chamber and result analysis showed that the antenna can achieve a diversity gain up to 24dB when all twelve elements are used and a spectral efficiency of more than 23 bps/Hz for a 4x12 MIMO system. Both channel simulations and diversity measurements showed that the antenna performs better when all its elements are individually used. For example, 12-ports perform better than 8-ports configuration which in turn performs better than 2-ports configuration. However, usage of more ports increase the complexity of the system (more hardware, extra resources) so 2-port mode can be used when simplicity is of major importance. Overall, the designed antenna is a flexible implementation since it can adapt both in terms of complexity (different modes) and in terms of environment (omni/sector).

5.2 Future work

The performance of the antenna can be increased if the design of the horizontal components is further investigated. Although the existing loops give good omni-directional, horizontal polarized patterns with a quite wide impedance match, their diameter is wide and sets some restrictions regarding the array configuration. Smaller size would allow a closer spacing for the elements ($< \lambda/2$) hence the omni-directional rippling would be reduced and sidelobes level would be lower.

Feeding of the elements can also be reconsidered in order to provide an easier and manufacture-friendly way to excite the elements. Instead of coaxial cables, planar transmission lines that follow the central metallic pole and spread on the three planes can be used as a feeding network. In this way, it would also be easier to use more than one antenna in a stacked configuration in order to increase directivity and/or total number of ports.

Bibliography

[1] C. A. Balanis, Antenna Theory : Analysis and Design, John Wiley & Sons, Inc., 2005.

[2] P. S. Kildal, Foundations of Antennas : A unified approach for Line-Of-Sight and Multipath, 2013.

[3] R. Yadava, Antenna and Wave Propagation, Phi Learning Private Limited, 2011.

[4] A. Ludwig, Mutual coupling, gain and directivity of an array of two identical antennas, Antennas and Propagation, IEEE Transactions on 24 (6) (1976) 837–841.

[5] A. Goldsmith, Wireless Communications, Cambridge University Press, 2005.

[6] P. S. Kildal, K. Rosengren, Correlation and capacity of mimo systems and mutual coupling, radiation efficiency, and diversity gain of their antennas: simulations and measurements in a reverberation chamber, Communications Magazine, IEEE 42 (12) (2004) 104–112.

[7] T. Brown, E. De Carvalho, P. Kyritsi, Practical Guide to the MIMO Radio Channel with MATLAB Examples, John Wiley & Sons, 2012.

[8] X. Chen, B. Einarsson, P.-S. Kildal, Improved mimo throughput with inverse power allocation - study using usrp measurement in reverberation chamber, Antennas and Wireless Propagation Letters, IEEE 13 (2014) 1494–1496.

[9] M. A. Solano, A. Vegas, A. Gomez, On the use of auxiliary vector potentials as a common tool for studying electromagnetic problems at undergraduate level, International Journal of Electrical Engineering Education 40 (2) (2003) 123.

[10] S.-W. Lee, J.-H. Lee, Electrically small mng zor antenna with multilayered conductor, IEEE Antennas and Wireless Propagation Letters 1 (2010) 724–727.

[11] J.-H. Park, Y.-H. Ryu, J.-H. Lee, Mu-zero resonance antenna, IEEE Transactions on Antennas and Propagation 54 (6) (2010) 1865–1875.

[12] K. Wei, Z. Zhang, Z. Feng, M. F. Iskander, A mng-tl loop antenna array with horizontally polarized omnidirectional patterns, IEEE Transactions on Antennas and Propagation 60 (6) (2012) 2702–2710.

[13] K. Wei, Z. Zhang, Z. Feng, Design of a wideband horizontally polarized omnidirectional printed loop antenna, IEEE Antennas and Wireless Propagation Letters 11 (2012) 49–52.

[14] A. Alford, A. G. Kandoian, Ultrahigh-frequency loop antennas, Transactions of the American Institute of Electrical Engineers 59 (12) (1940) 843–848.

[15] H. Chuang, T. Horng, J. Pan, C. Wang, Omni-directional horizontally polarized alford loop strip antenna, uS Patent 5,767,809 (Jun. 16 1998).
URL `http://www.google.co.uk/patents/US5767809`

[16] C.-C. Lin, H. R. Chuang, A 2.4ghz planar printed antenna with omni-directional horizontally polarized pattern for wlan applications, in: Microwave Conference, 2003. 33rd European, 2003, pp. 1275–1278.

[17] X. Quan, R. Li, J. Wang, Y. Cui, Development of a broadband horizontally polarized omnidirectional planar antenna and its array for base stations, Progress In Electromagnetics Research 128 (2012) 441–456.

[18] C.-H. Ahn, S.-W. Oh, K. Chang, A dual-frequency omnidirectional antenna for polarization diversity of mimo and wireless communication applications, Antennas and Wireless Propagation Letters, IEEE 8 (2009) 966–969.

[19] C. Jiang, X. W. Dai, Y.-C. Jiao, A novel compact horizontally polarized omnidirectional antenna, in: Signals Systems and Electronics (ISSSE), 2010 International Symposium on, Vol. 1, 2010, pp. 1–3.

[20] Y. Yu, F. Jolani, Z. Chen, A wideband omnidirectional horizontally polarized antenna for 4g lte applications, Antennas and Wireless Propagation Letters, IEEE 12 (2013) 686–689.

[21] J. I. Kim, B. M. Lee, Y. J. Yoon, Wideband printed dipole antenna for multiple wireless services, 2001, pp. 153–156.

[22] G. Chen, J. Sun, A printed dipole antenna with microstrip tapered balun, Microwave and Optical Technology Letters 40 (4) (2004) 344–346.

[23] Y. Wang, L. Yang, S. Gong, X. Feng, J. Wang, Omnidirectional antenna with dipole array, IEEE, 2012, pp. 347–348.

[24] B. G. Duffley, G. A. Morin, M. Mikavica, Y. M. M. Antar, A wide-band printed double-sided dipole array, IEEE Transactions on Antennas and Propagation 52 (2) (2004) 628–631.

[25] K. P. Ray, Design aspects of printed monopole antennas for ultra-wide band applications, International Journal of Antennas and Propagation 2008 (2008) 1–8.

[26] A. V. S. Lages, V. Dmitriev, M. N. Kawakatsu, D. C. Nascimento, D. B. Ferreira, E. S. Costa, Ultr-wideband planar monopole antennas with improved characteristics, Microwave and Optical Technology Letters 55 (9) (2013) 2149–2154.

[27] R. A. Sadeghzadeh, Y. Zehforoosh, N. Mirmotahhary, Ultra-wideband monopole antenna with modified triangular patch, Microwave and Optical Technology Letters 53 (8) (2011) 1752–1756.

[28] M. Ammann, Square planar monopole antenna, in: Antennas and Propagation, 1999. IEE National Conference on., 1999, pp. 37–40.

[29] Z. N. Chen, Broadband planar monopole antenna, IEE Proceedings - Microwaves, Antennas and Propagation 147 (6) (2000) 526.

[30] P. Kildal, C. Orlenius, J. Carlsson, Ota testing in multipath of antennas and wireless devices with mimo and ofdm, Vol. 100, IEEE, 2012, pp. 2145–2157.

[31] P. Kildal, K. Rosengren, J. Byun, J. Lee, Definition of effective diversity gain and how to measure it in a reverberation chamber, Microwave and Optical Technology Letters 34 (1) (2002) 56–59.

[32] P.-S. Kildal, U. Carlberg, J. Carlsson, Definition of antenna diversity gain in user-distributed 3d-random line-of-sight, Journal of electromagnetic engineering and science 13 (2) (2013) 86–92.

[33] U. Carlberg, J. Carlsson, A. Hussain, P. S. Kildal, Ray based multipath simulation tool for studying convergence and estimating ergodic capacity and diversity gain for antennas with given far-field functions, in: ICECom, 2010 Conference Proceedings, 2010, pp. 1–4.

[34] P.-S. Kildal, X. Chen, C. Orlenius, M. Franzen, C. S. L. Patane, Characterization of reverberation chambers for ota measurements of wireless devices: Physical formulations of channel matrix and new uncertainty formula, IEEE Transactions on Antennas and Propagation 60 (8) (2012) 3875–3891.

[35] X. Chen, P.-S. Kildal, J. Carlsson, J. Yang, Mrc diversity and mimo capacity evaluations of multi-port antennas using reverberation chamber and anechoic chamber, IEEE Transactions on Antennas and Propagation 61 (2) (2013) 917–926.

[36] WINNER Phase II Model, `http://www.ist-winner.org/phase_2_model.html` (2007).

A

Mathematical expressions for radiating fields

General expressions for radiating fields

If the electric surface current and the magnetic surface current, $\mathbf{J}$ and $\mathbf{M}$ respectively, are known then the general radiation expressions are given by [2]:

$$\mathbf{E}(\mathbf{r}) = \mathbf{E}_J(\mathbf{r}) + \mathbf{E}_M(\mathbf{r}) \tag{A.1}$$

$$\mathbf{H}(\mathbf{r}) = \mathbf{H}_J(\mathbf{r}) + \mathbf{H}_M(\mathbf{r}) \tag{A.2}$$

where

$$\mathbf{E}_J = C_k \iint\limits_{S'} \left[\eta \mathbf{J} C_{N1} - (\eta \mathbf{J} \cdot \hat{\mathbf{R}})\hat{\mathbf{R}}\, C_{N2}\right] \frac{1}{R} e^{-jkR}\, dS' \tag{A.3}$$

$$\mathbf{H}_J = -\frac{1}{\eta} C_k \iint\limits_{S'} \left(\eta \mathbf{J} \cdot \hat{\mathbf{R}}\right) C_N \frac{1}{R} e^{-jkR}\, dS' \tag{A.4}$$

$$\mathbf{E}_M = C_k \iint\limits_{S'} \left(\mathbf{M} \cdot \hat{\mathbf{R}}\right) C_N \frac{1}{R} e^{-jkR}\, dS' \tag{A.5}$$

$$\mathbf{H}_M = \frac{1}{\eta} C_k \iint\limits_{S'} \left[\mathbf{M} C_{N1} - (\mathbf{M} \cdot \hat{\mathbf{R}})\hat{\mathbf{R}}\, C_{N2}\right] \frac{1}{R} e^{-jkR}\, dS' \tag{A.6}$$

with $C_k = -jk/(4\pi)$, $C_N = 1 + \frac{1}{jkR}$, $C_{N1} = 1 + \frac{1}{jkR} - \frac{1}{(kR)^2}$, $C_{N2} = 1 + \frac{3}{jkR} - \frac{3}{(kR)^2}$ and where S' is the surface of the radiating element, $\mathbf{r}'$ is the current vector, $\mathbf{r}$ is the observation point and $\mathbf{R} = \mathbf{r} - \mathbf{r}'$, $R = |r - r'|$, $\hat{\mathbf{R}} = \mathbf{R}/R$.

When in far-field, the Fraunhofer approximation can be applied, thus:

$$\mathbf{E}(\mathbf{r}) = \frac{1}{r} e^{-jkr} \left\{ \mathbf{I}_J - (\mathbf{I}_J \cdot \hat{\mathbf{r}})\, \hat{\mathbf{r}} + \mathbf{I}_M \times \hat{\mathbf{r}} \right\} \tag{A.7}$$

$$\mathbf{H}(\mathbf{r}) = \frac{1}{\eta} \hat{\mathbf{r}} \times \mathbf{E} = \frac{1}{\eta r} e^{-jkr} \left\{ \hat{\mathbf{r}} \times \mathbf{I}_J + [\mathbf{I}_M - (\mathbf{I}_M \cdot \hat{\mathbf{r}}) \hat{\mathbf{r}}] \right\} \tag{A.8}$$

where

$$\mathbf{I}_J = C_k \iint\limits_{S'} \eta \mathbf{J}(\mathbf{r}') e^{jk(\mathbf{r}' \cdot \hat{\mathbf{r}})} dS' \tag{A.9}$$

$$\mathbf{I}_M = C_k \iint\limits_{S'} \mathbf{M}(\mathbf{r}') e^{jk(\mathbf{r}' \cdot \hat{\mathbf{r}})} dS' \tag{A.10}$$

are the electric and magnetic radiation integrals.

Integral formula used in dipole's radiating field:

$$\int e^{\alpha x} \sin(\beta x + \gamma) dx = e^{\alpha x} \frac{1}{\alpha^2 + \beta^2} [\alpha \sin(\beta x + \gamma) - \beta \cos(\beta x + \gamma)] \tag{A.11}$$

3-Dimensional Characteristics

For a vector $\mathbf{r}$ with magnitude $r = |\mathbf{r}|$, conversion from spherical to rectangular coordinate system can be obtained through the following equations :

$$\begin{aligned} x &= r \sin\theta \cos\phi\ \hat{\mathbf{x}} \\ y &= r \sin\theta \sin\phi\ \hat{\mathbf{y}} \\ z &= r \cos\theta\ \hat{\mathbf{z}} \end{aligned} \tag{A.12}$$

The angle γ between one axis and an observation point can be obtained by the dot product of a unit vector along this axis and a unit vector towards the observation point. If the elements of a linear array are along the z-axis then they have a symmetry in respect to this axis and are independent of the ϕ angle because :

$$\cos\gamma = \hat{\mathbf{a}_z} \cdot \hat{\mathbf{a}_r} = \hat{\mathbf{a}_z} \cdot (\hat{\mathbf{a}_x} \sin\theta \cos\phi + \hat{\mathbf{a}_y} \sin\theta \sin\phi + \mathbf{a}_z \hat{\cos}\theta) = \cos\theta \rightarrow \gamma = \theta \tag{A.13}$$

On the other hand, if elements are positioned along x or y axis then angle γ is dependent of both θ and ϕ angles as can be seen from the following equations :

$$\begin{aligned} &\cos\gamma = \hat{\mathbf{a}_z} \cdot \hat{\mathbf{a}_r} = \hat{\mathbf{a}_z} \cdot (\hat{\mathbf{a}_x} \sin\theta \cos\phi + \hat{\mathbf{a}_y} \sin\theta \sin\phi + \mathbf{a}_z \hat{\cos}\theta) = \sin\theta \cos\phi \rightarrow \\ &\rightarrow \gamma = \cos^{-1}(\sin\theta \cos\phi) \end{aligned} \tag{A.14}$$

and

$$\cos\gamma = \hat{\mathbf{a}_z} \cdot \hat{\mathbf{a}_r} = \hat{\mathbf{a}_z} \cdot (\hat{\mathbf{a}_x} \sin\theta\cos\phi + \hat{\mathbf{a}_y} \sin\theta\sin\phi + \mathbf{a}_z \hat{\cos}\theta) = \sin\theta\sin\phi \rightarrow$$
$$\rightarrow \gamma = \cos^{-1}(\sin\theta\sin\phi) \tag{A.15}$$

B

Antenna Structure figures

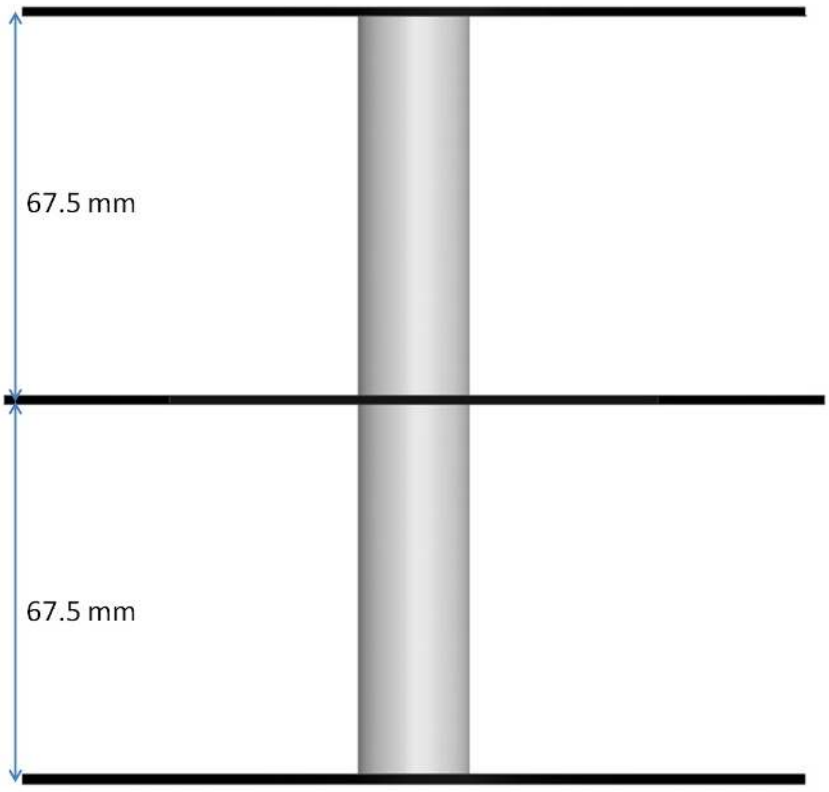

Figure B.1: View 1 of the HPol Array. Middle plane contains the 4 horizontal polarized elements and the other two are the ground planes

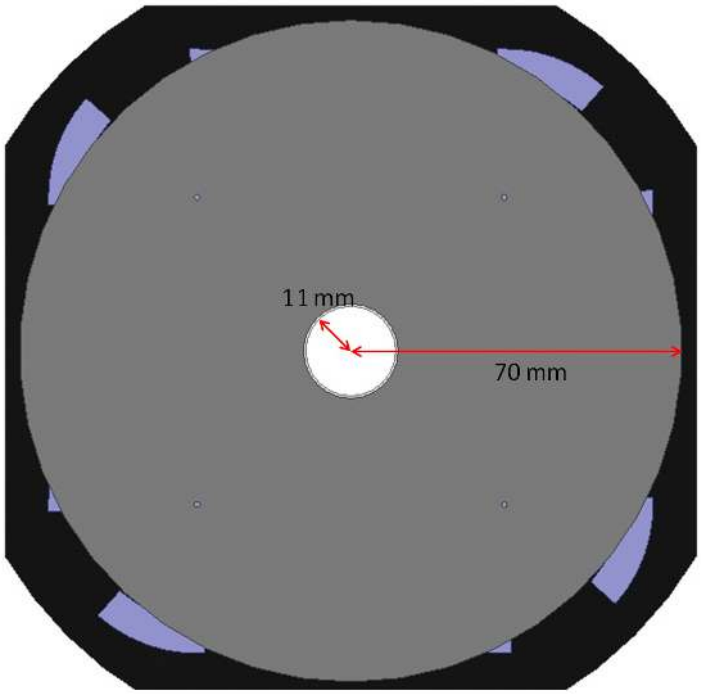

Figure B.2: View 2 of the HPol Array. Radius of the ground plane and the hollow central metal tube.

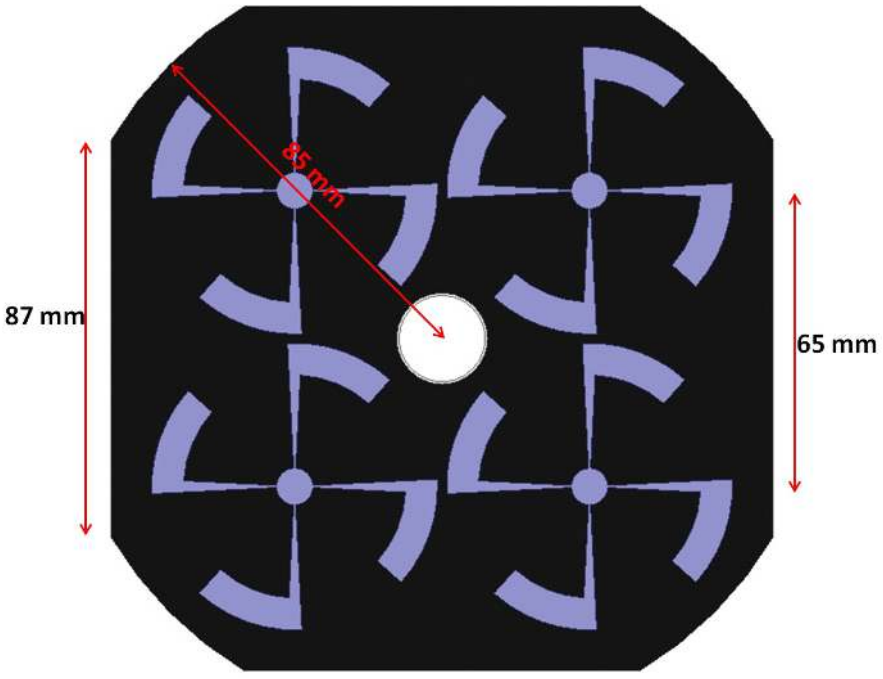

Figure B.3: View 3 of the HPol Array. Dimensions of the middle plane.

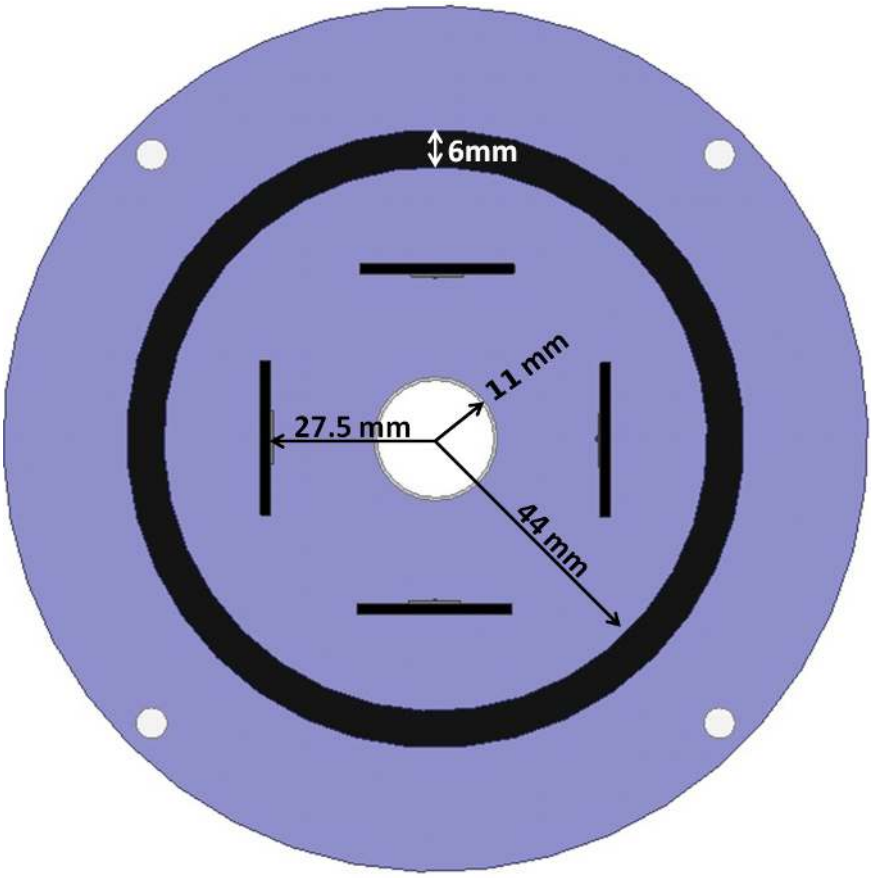

Figure B.4: Dimensions of the ground plane and positioning of the monopoles.

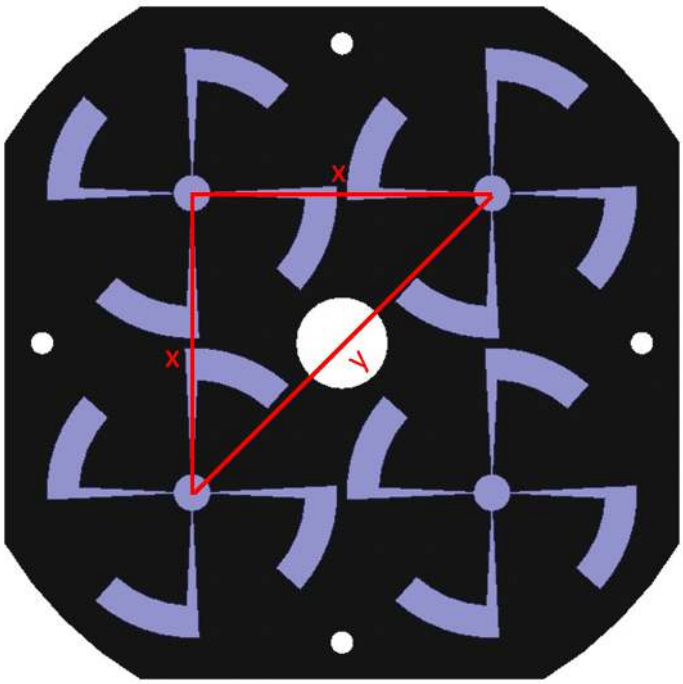

Figure B.5: Maximal distance (y) between two magnetic dipoles. $x = 2 * (L1 + L2)$ and $y = \sqrt{2 * x^2}$

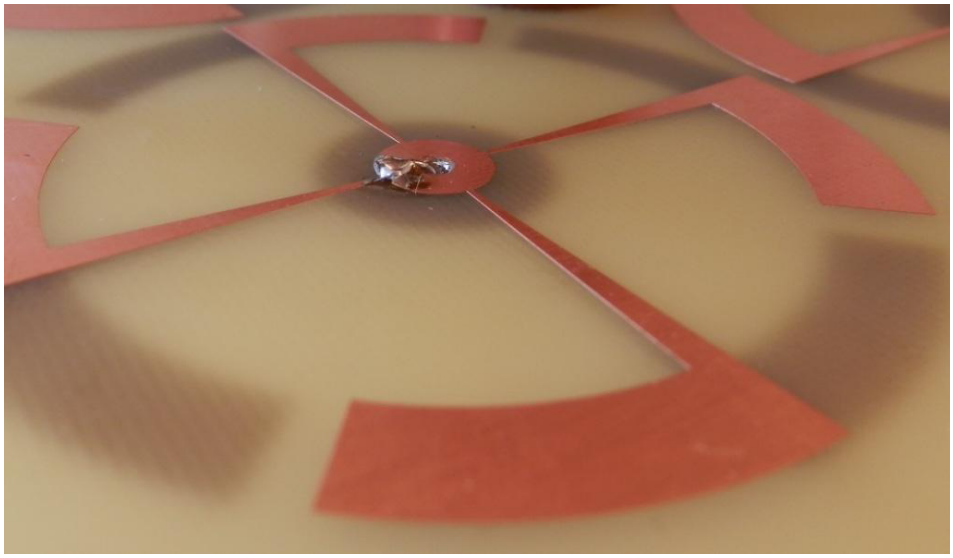

(a)

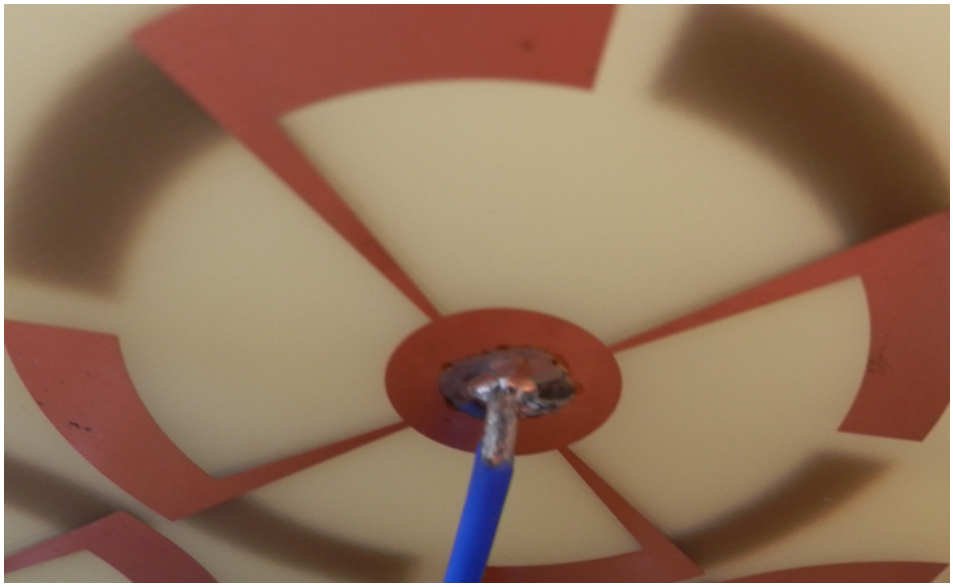

(b)

Figure B.6: Feeding of the magnetic dipole. Inner conductor of the coaxial cable is soldered to the top metal (up) and outer conductor to the bottom metal (down).

(a)

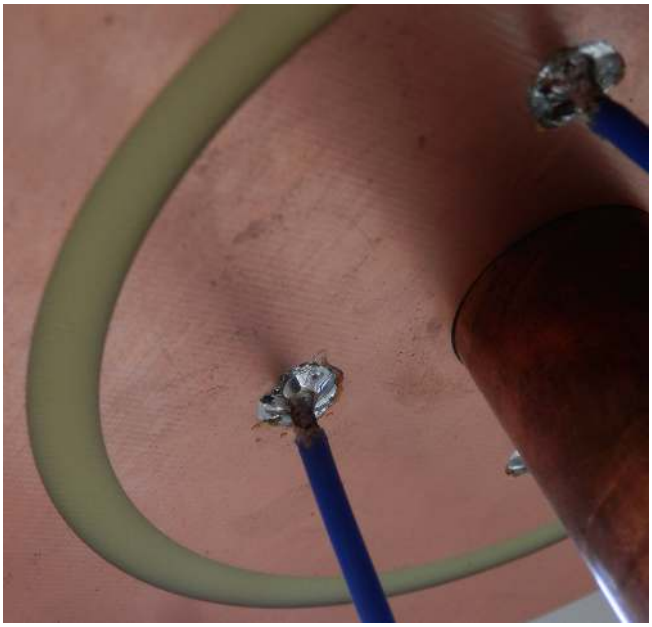

(b)

Figure B.7: Feeding of the monopole patches. The Inner conductor of the coaxial cable is soldered to the feeding patch (up) and the outer conductor to the outer surface of the ground plane (down).

Figure B.8: Top view of the prototype antenna

Figure B.9: Bottom view of the prototype antenna

C

Reverberation Chamber and channel simulation

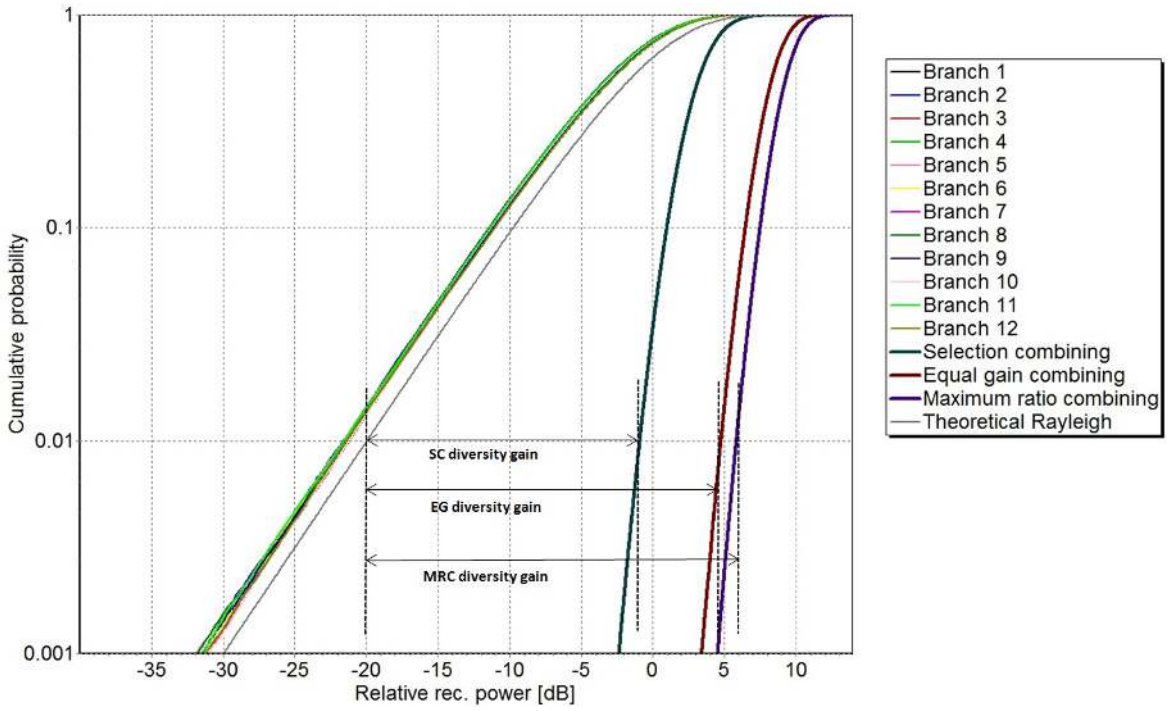

Figure C.1: CDF plots and effective gain of the 12-port antenna

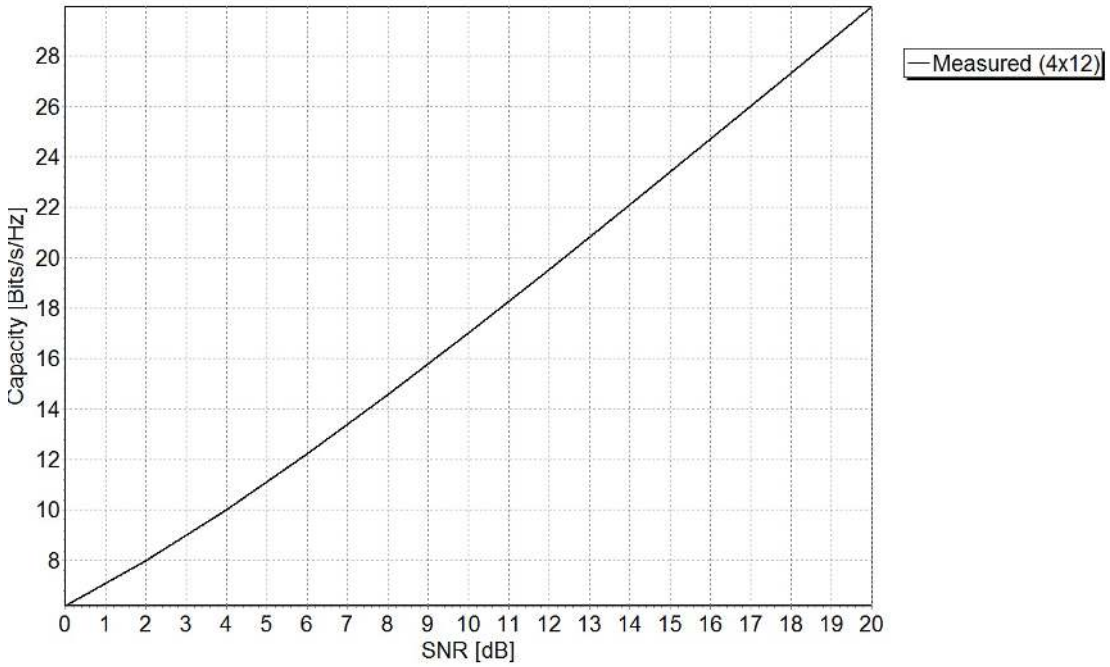

Figure C.2: Spectral efficiency plot of the 4 × 12 MIMO channel

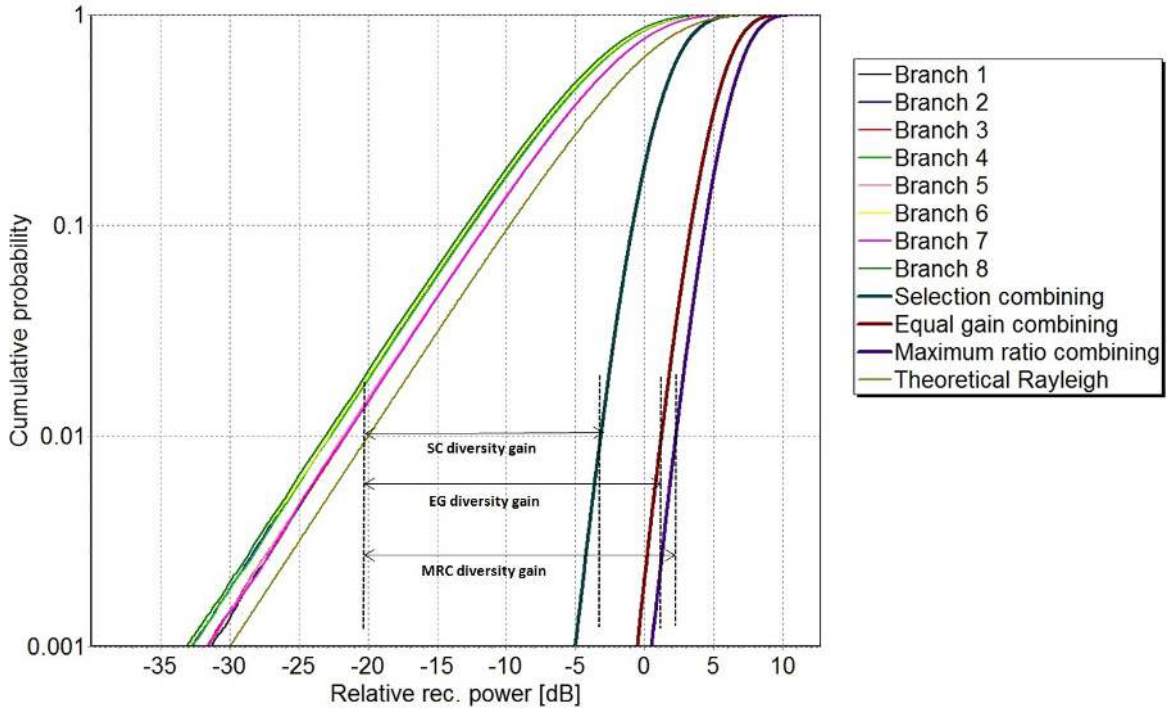

Figure C.3: CDF plots and effective gain of the 8-port antenna

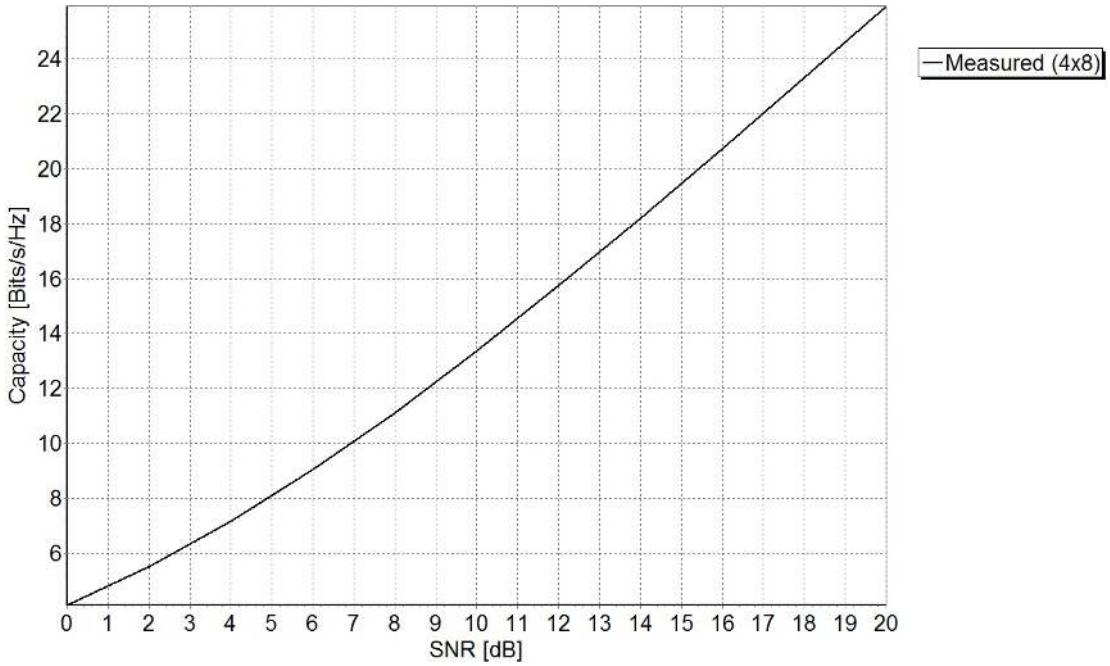

Figure C.4: Spectral efficiency plot of the 4 × 8 MIMO channel

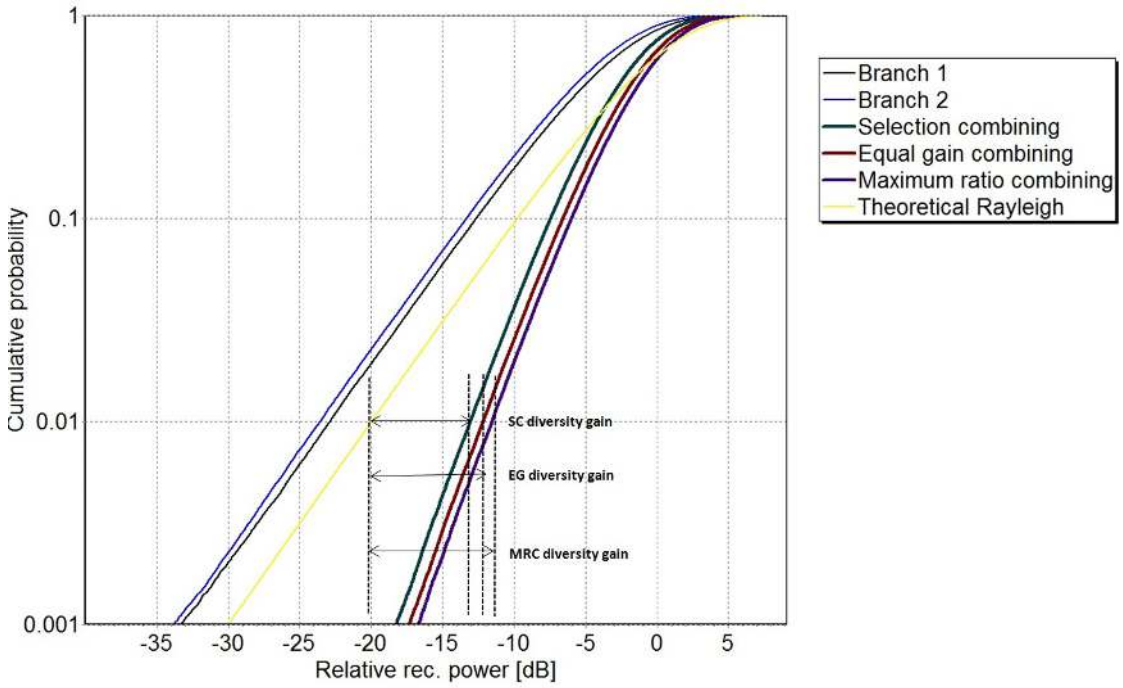

Figure C.5: CDF plots and effective gain of the 2-port OMNI-mode antenna

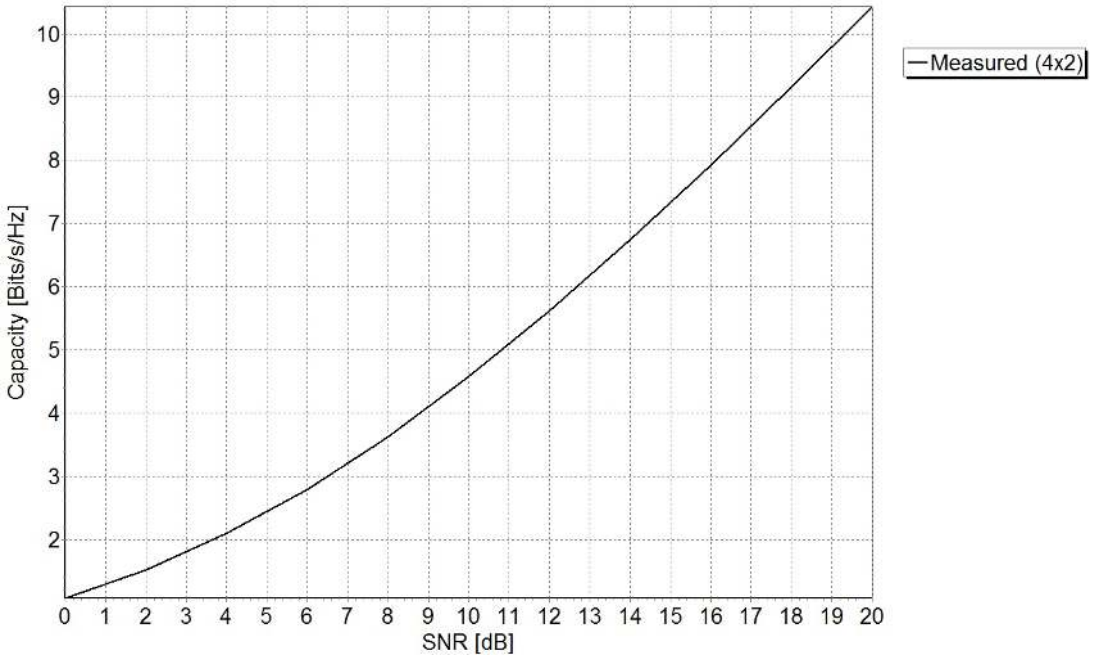

Figure C.6: Spectral efficiency plot of the 4 × 2 MIMO channel

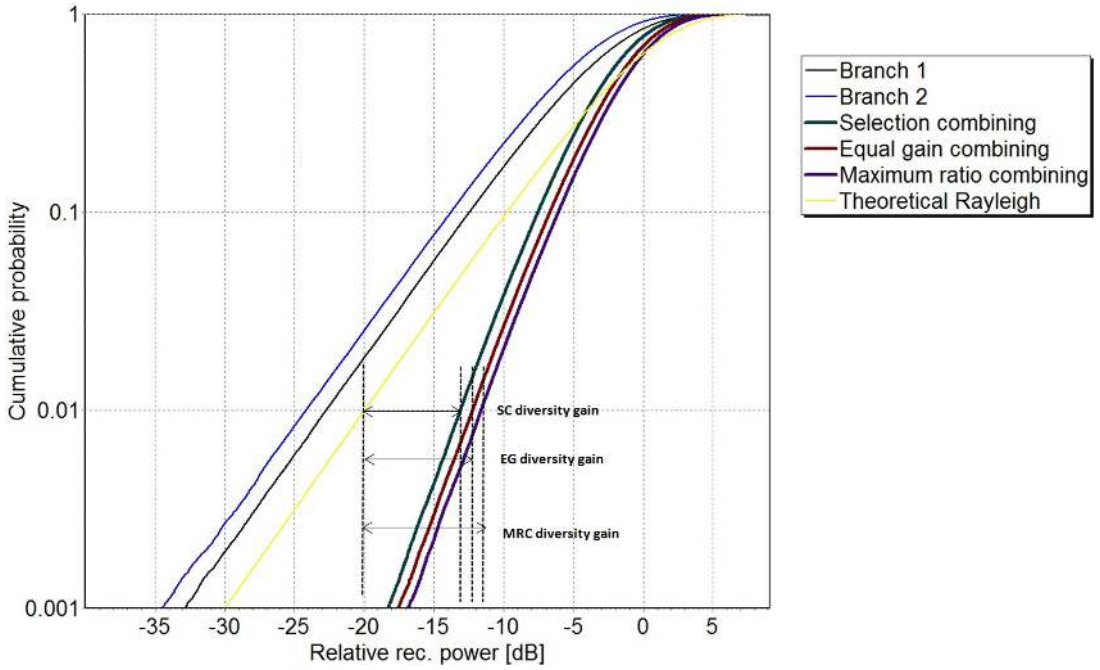

Figure C.7: CDF plots and effective gain of the 2-port SECTOR-mode antenna

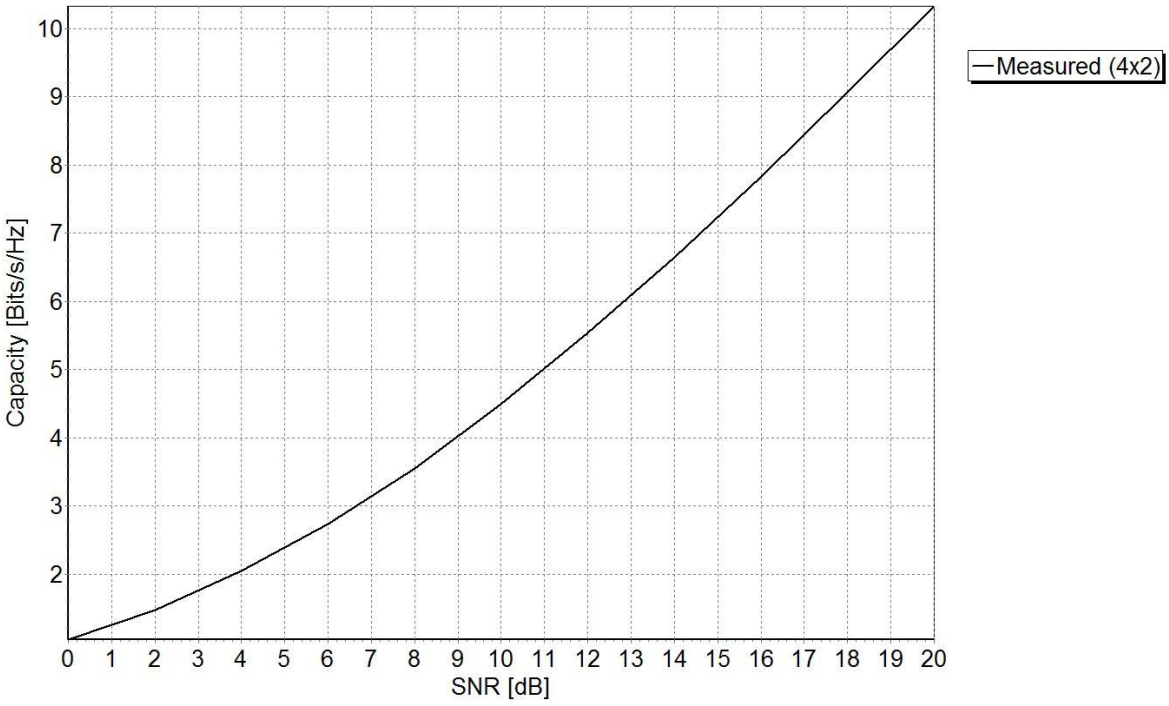

Figure C.8: Spectral efficiency plot of the 4 × 2 MIMO channel

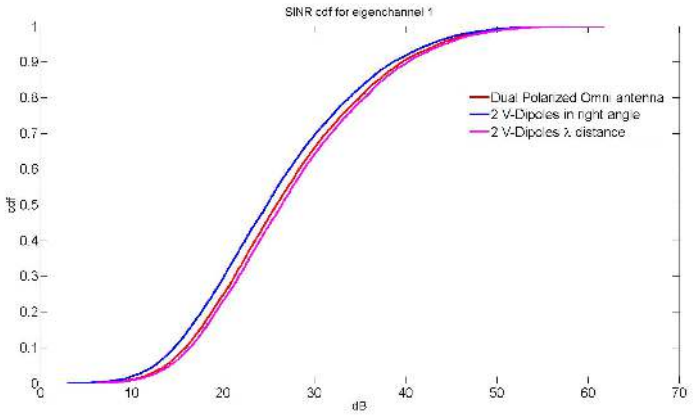

(a)

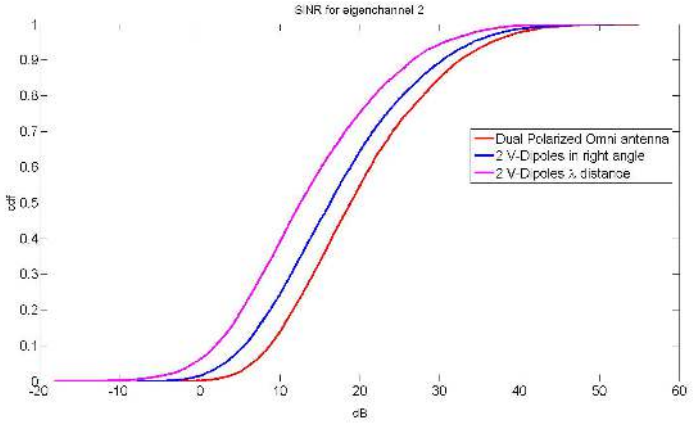

(b)

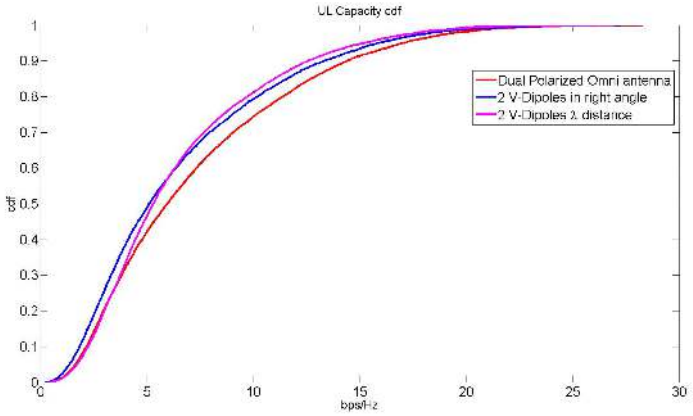

(c)

Figure C.9: Plots for SNR of eigenchannel 1, eigenchannel 2 and spectral efficiency respectively. Red lines indicate the dual polarized antenna, blue lines indicate two orthogonal electric dipoles and the purple one indicates two electrical dipoles placed one λ apart.

D

Return Loss and coupling

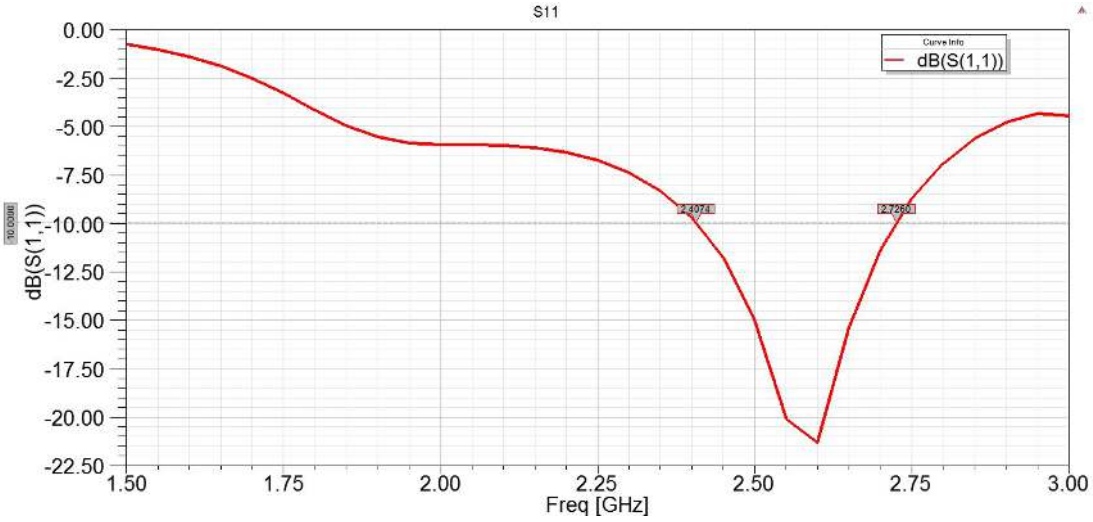

Figure D.1: Bandwidth of the original antenna as proposed by [20] but without parasitic strips.

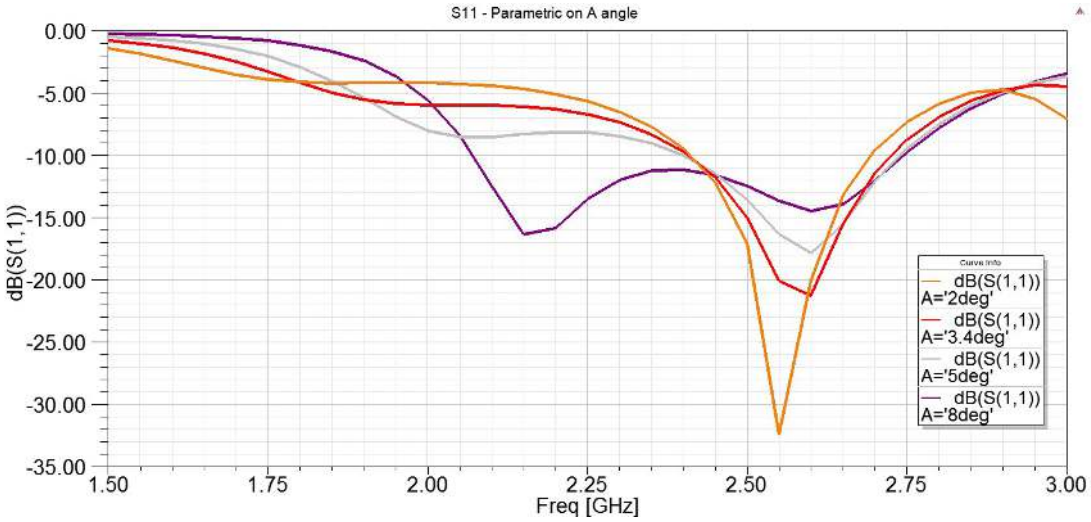

Figure D.2: Parametric study on horizontally polarized omni-directional antenna's angle A. Bandwidth increases as angle A increases.

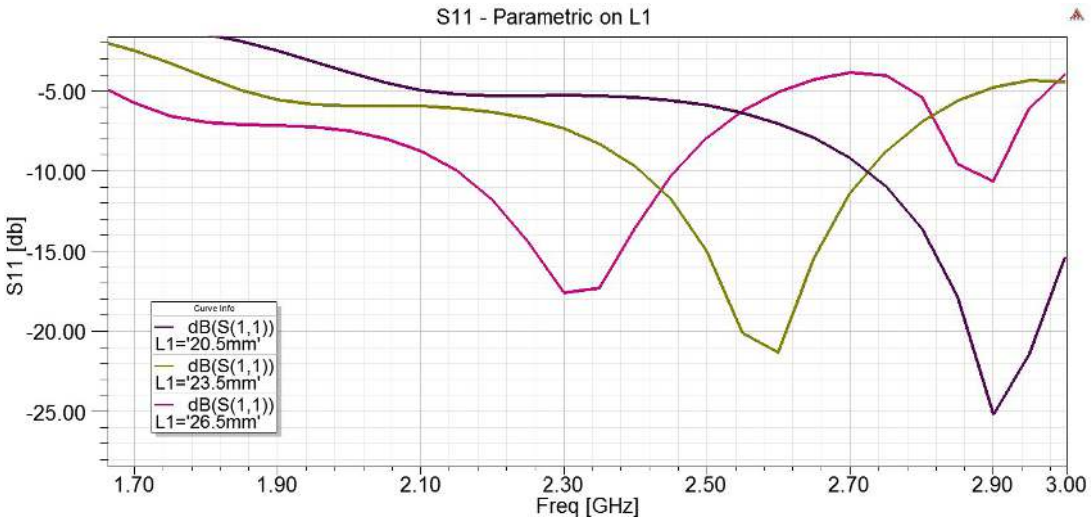

Figure D.3: Parametric study on horizontally polarized omni-directional antenna's size. The resonance frequency moves lower in the spectrum as the size of the antenna increases.

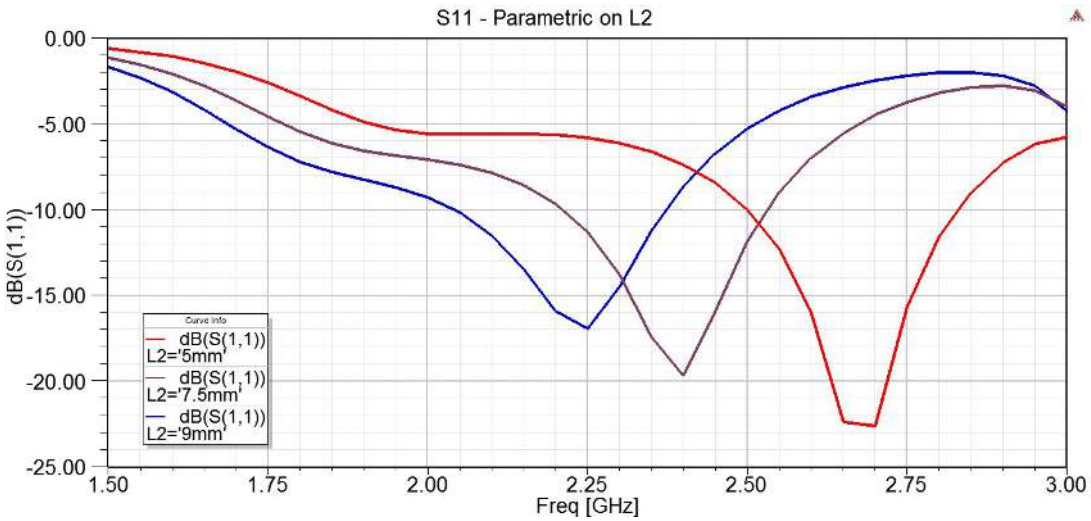

Figure D.4: Parametric study on horizontally polarized omni-directional antenna's size. The resonance frequency moves lower in the spectrum as the width of the dipole arm increases.

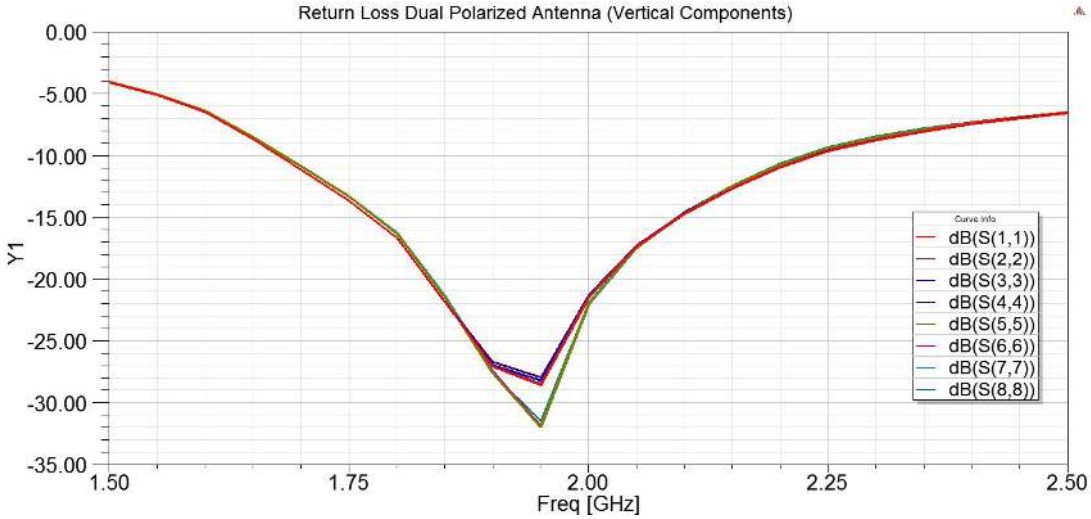

(a) Return Loss of Monopoles

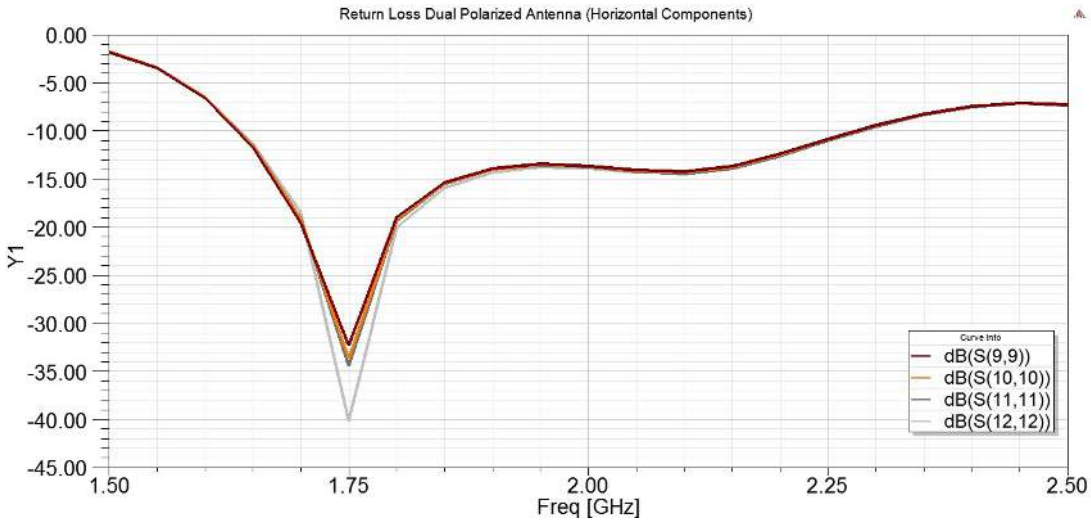

(b) Return Loss of magnetic dipoles

Figure D.5: Return loss of the dual polarized antenna.

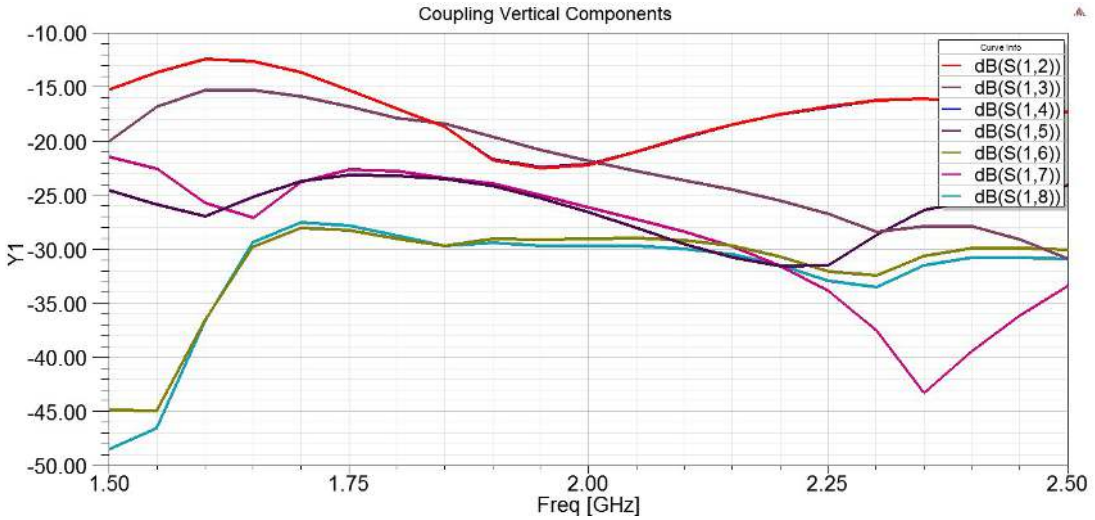

(a) Coupling between monopole elements

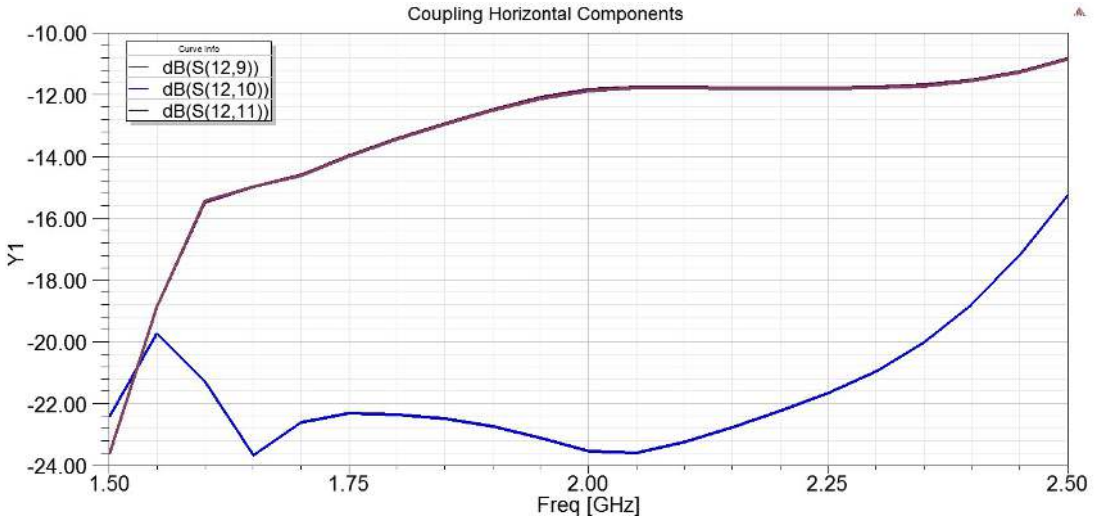

(b) Coupling between magnetic dipole elements

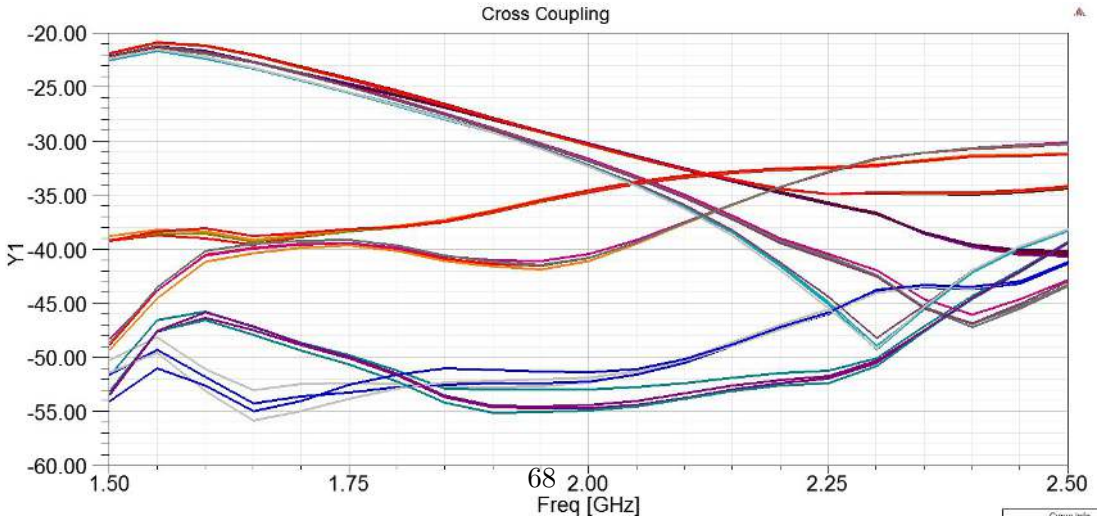

(c) Coupling between orthogonal polarized elements

Figure D.6: Coupling of the dual polarized antenna.

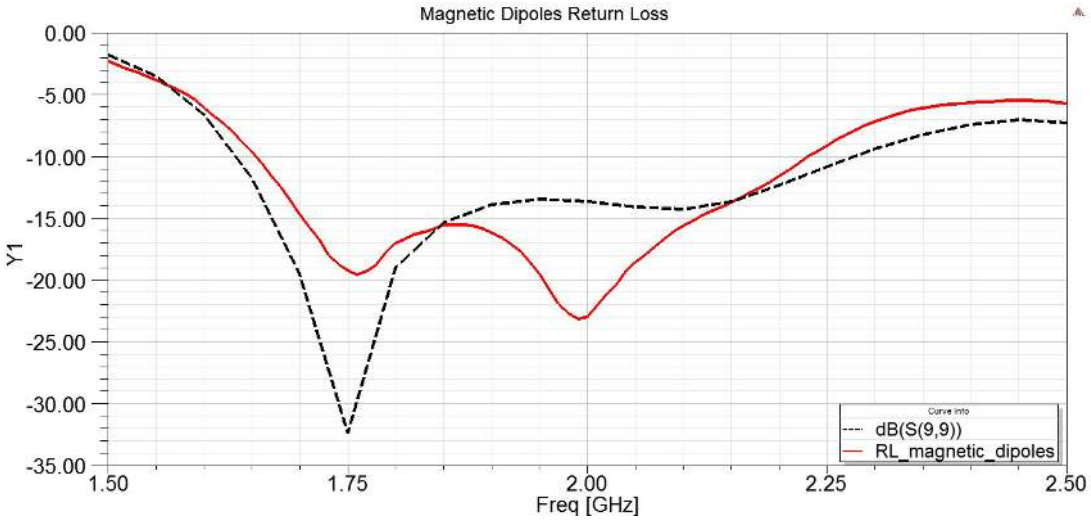

Figure D.7: Return loss of the magnetic dipoles as measured on a 2-port VNA. The black dashed line indicates the simulated return loss.

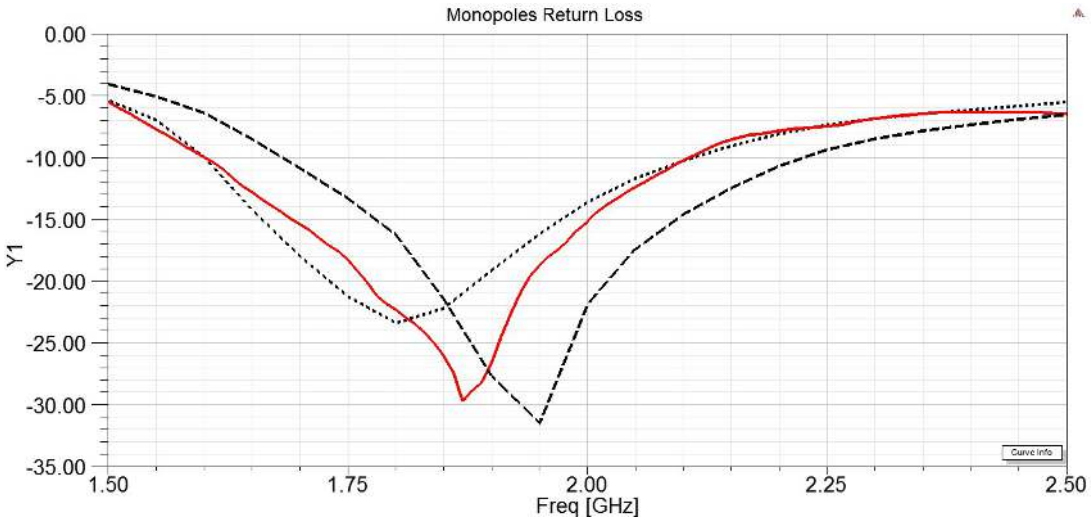

Figure D.8: Return loss of the monopole patches as measured on a 2-port VNA. The black dashed line indicates the initially simulated return loss while the dotted line shows the simulated return loss for the expanded substrate case.

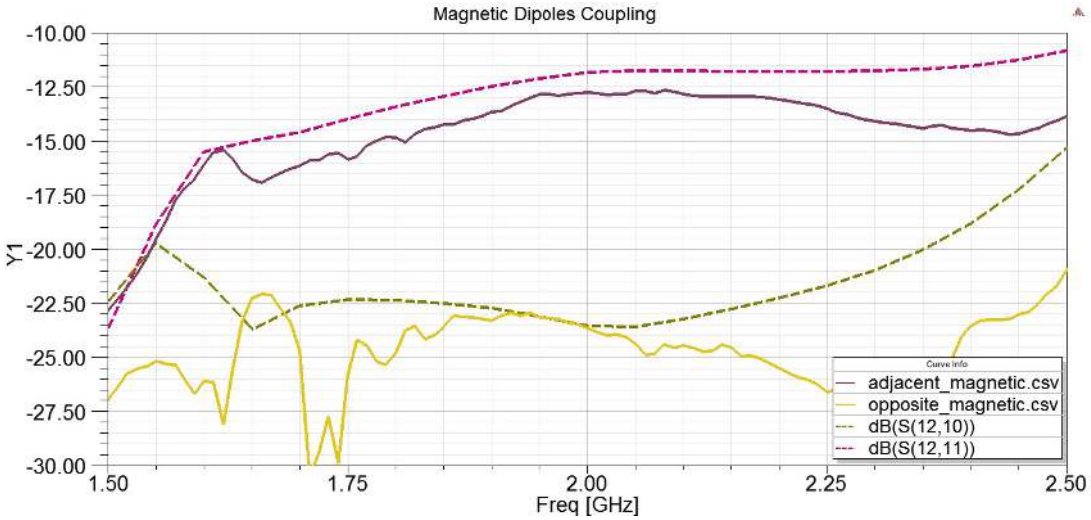

Figure D.9: Coupling levels between magnetic dipoles. Purple line shows coupling values for adjacent dipoles while yellow line shows coupling between opposite dipoles. Dashed lines indicate the simulated values.

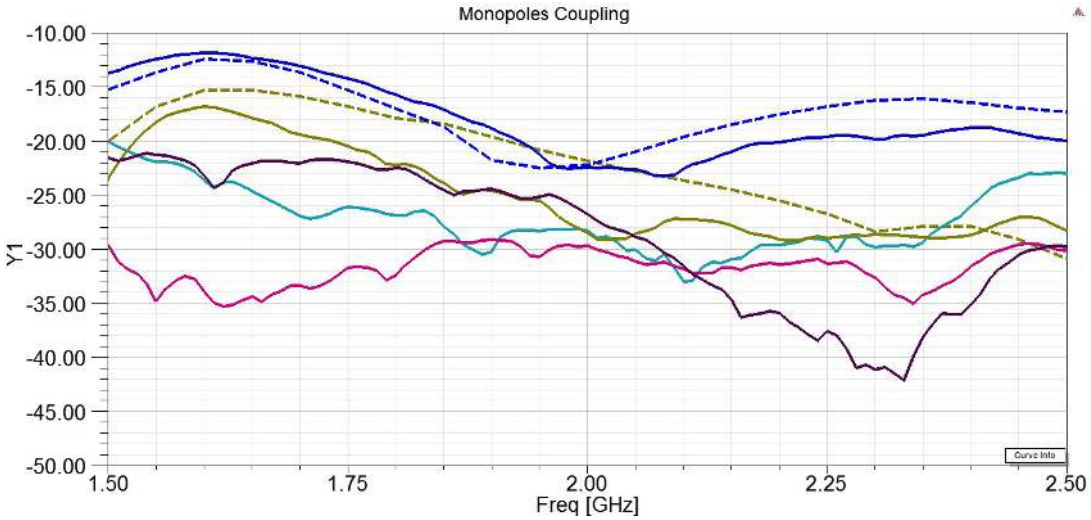

Figure D.10: Coupling levels between monopole patches. Dashed line represent simulated values for adjacent and opposite elements.

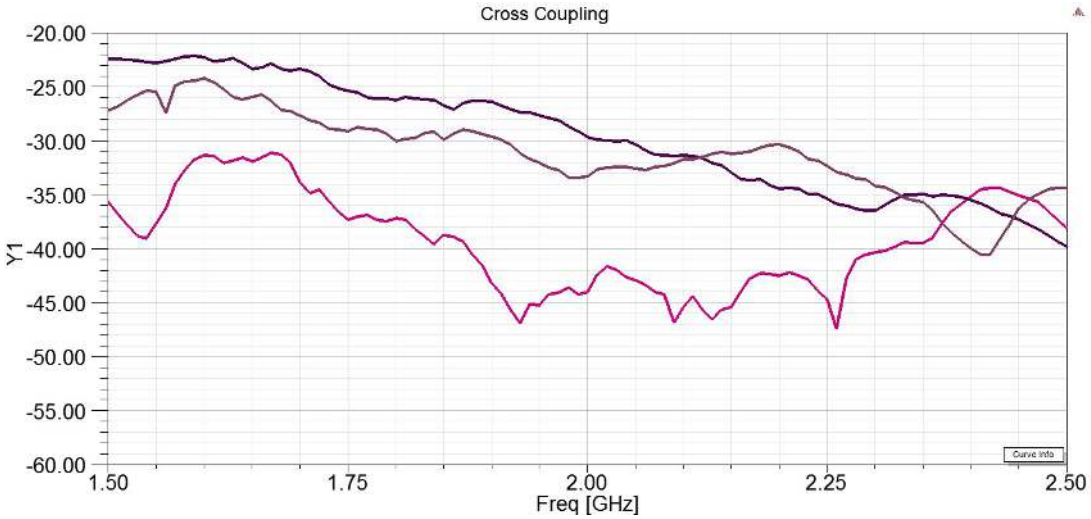

Figure D.11: Coupling levels between vertical and horizontal polarized elements.

E

Radiation Patterns

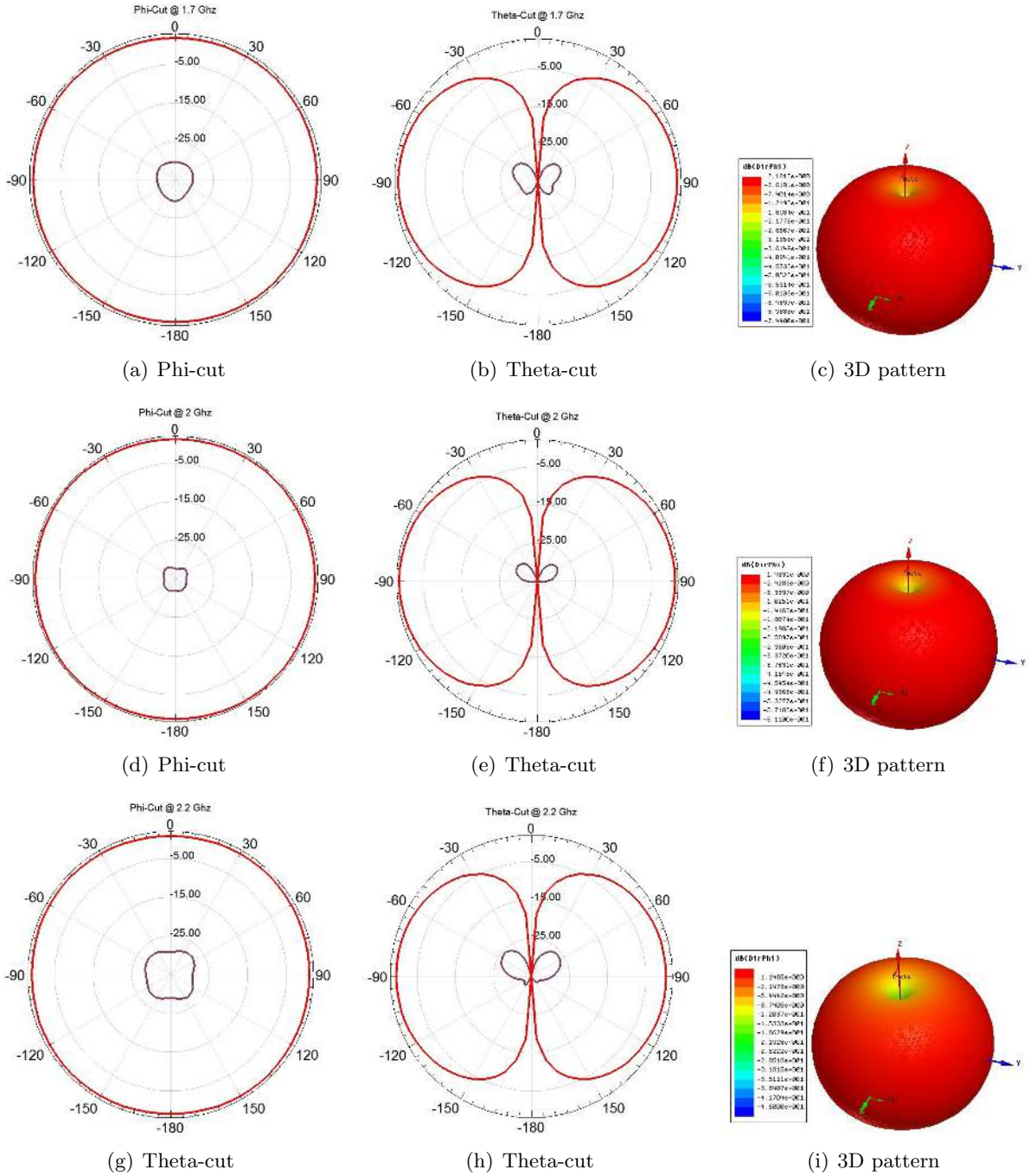

(a) Phi-cut (b) Theta-cut (c) 3D pattern

(d) Phi-cut (e) Theta-cut (f) 3D pattern

(g) Theta-cut (h) Theta-cut (i) 3D pattern

Figure E.1: Horizontal polarized omni-directional antenna radiation pattern @ 1.7, 2 and 2.2 GHz. Both co-polar and cross-polar components are depicted.

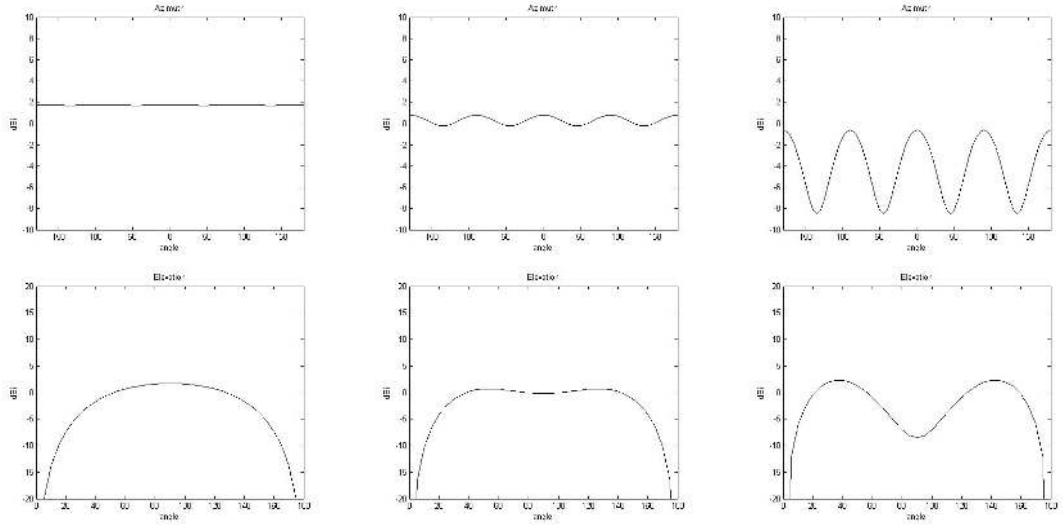

(a) $\lambda/4$ distance (b) $\lambda/2$ distance (c) $\lambda/1.5$ distance

Figure E.2: Azimuth (up) and elevation (down) cuts when in OMNI mode for three different element distances.

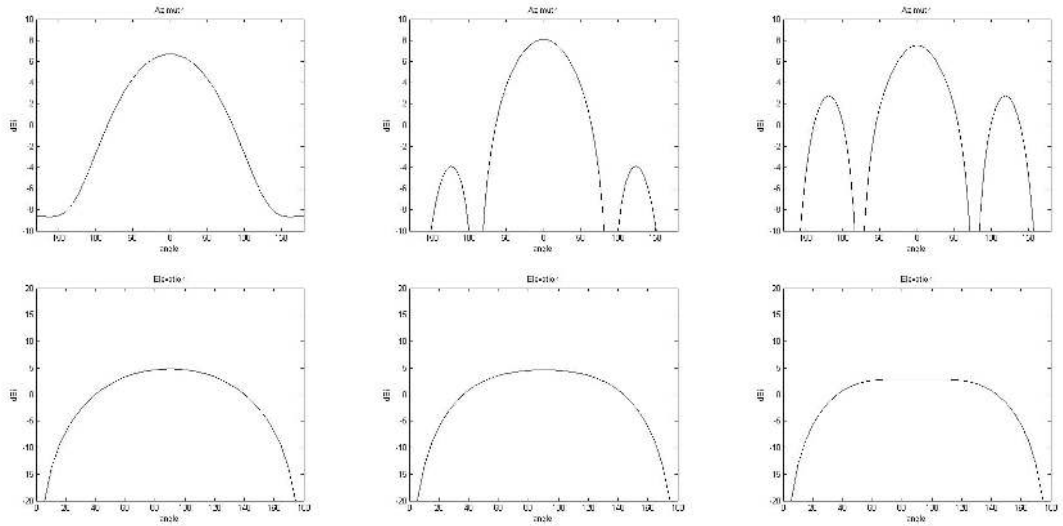

(a) $\lambda/4$ distance (b) $\lambda/2$ distance (c) $\lambda/1.5$ distance

Figure E.3: Azimuth (up) and elevation (down) cuts when in SECTOR mode for three different element distances.

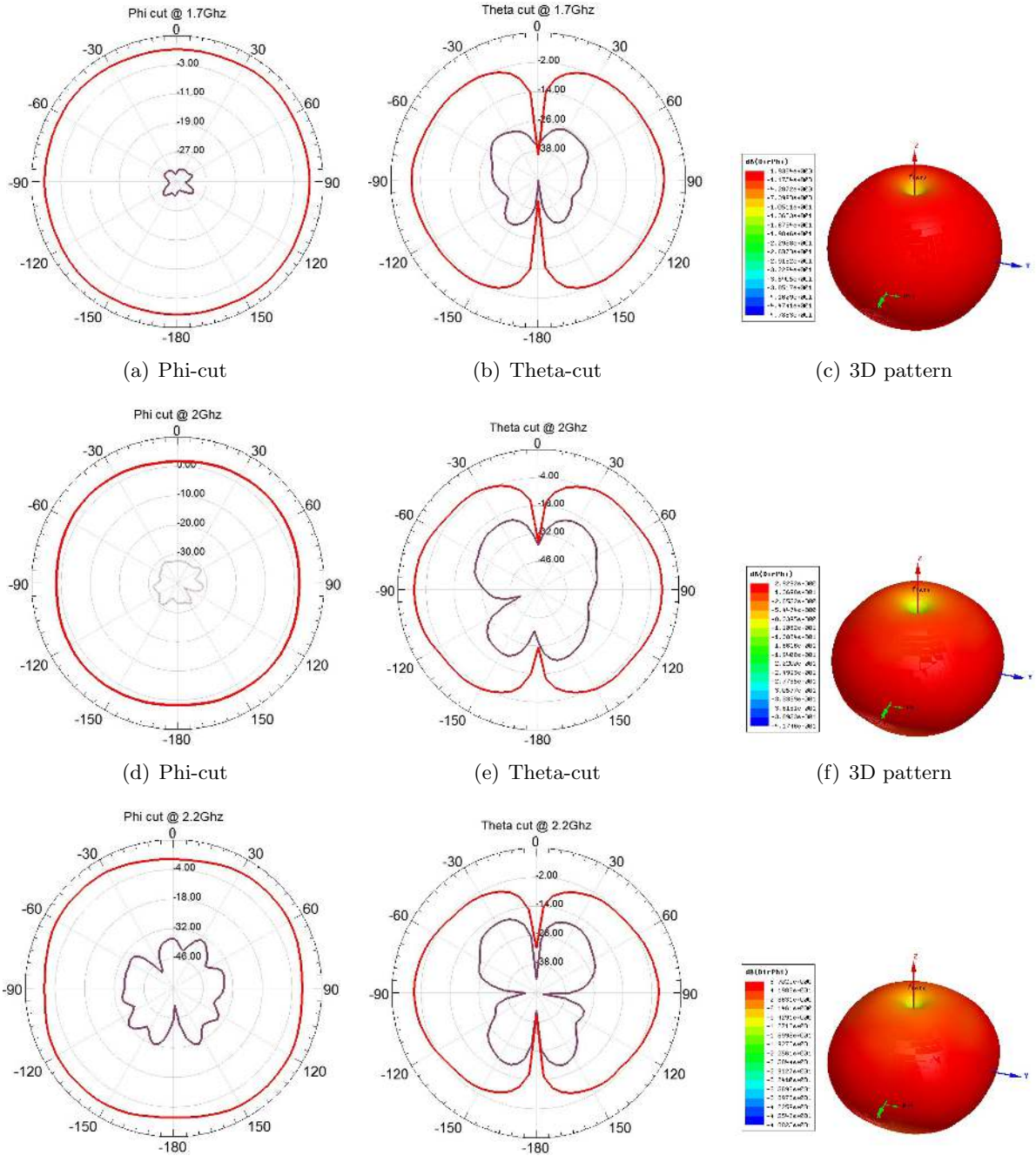

(a) Phi-cut (b) Theta-cut (c) 3D pattern

(d) Phi-cut (e) Theta-cut (f) 3D pattern

(g) Phi-cut (h) Theta-cut (i) 3D pattern

Figure E.4: Horizontal polarized Array radiation pattern in OMNI mode @ 1.7, 2 and 2.2 GHz.

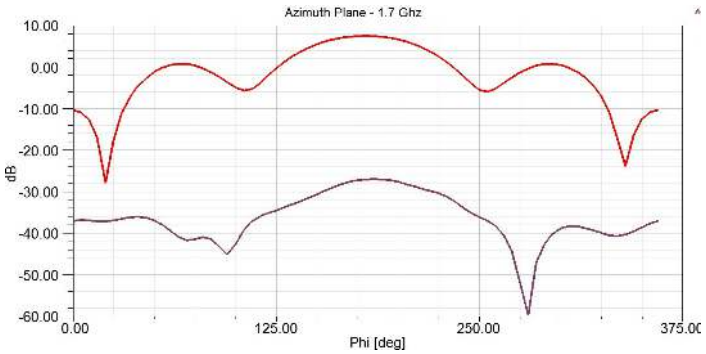

(a) Phi Cut

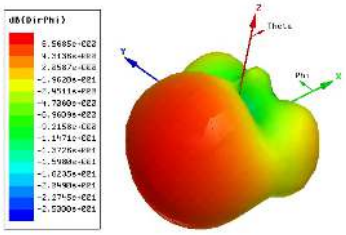

(b) 3D pattern

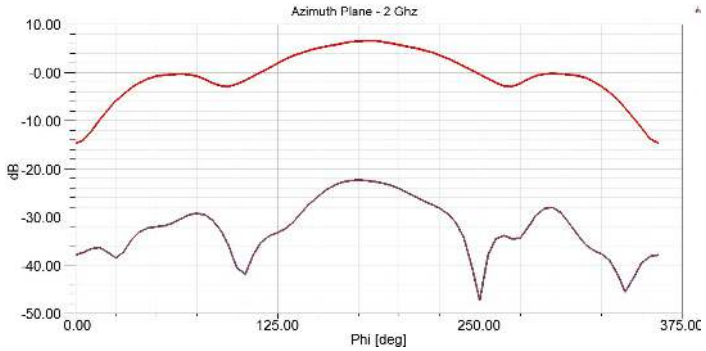

(c) Phi Cut

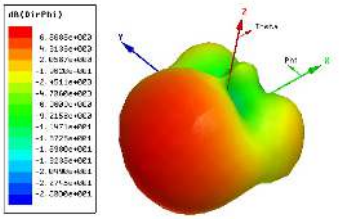

(d) 3D pattern

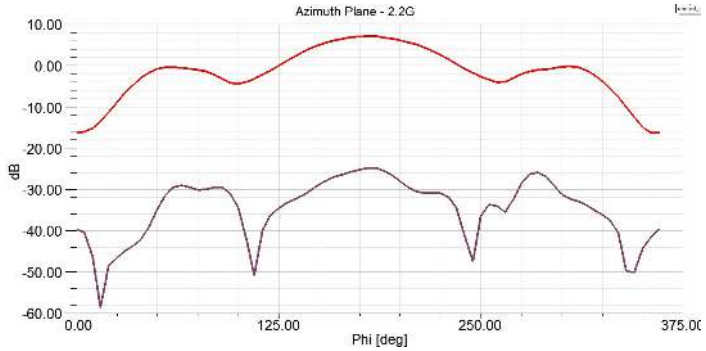

(e) Phi Cut

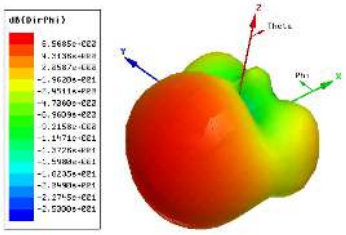

(f) 3D pattern

Figure E.5: Horizontal polarized Array radiation pattern in SECTOR mode @ 1.7, 2 and 2.2 GHz

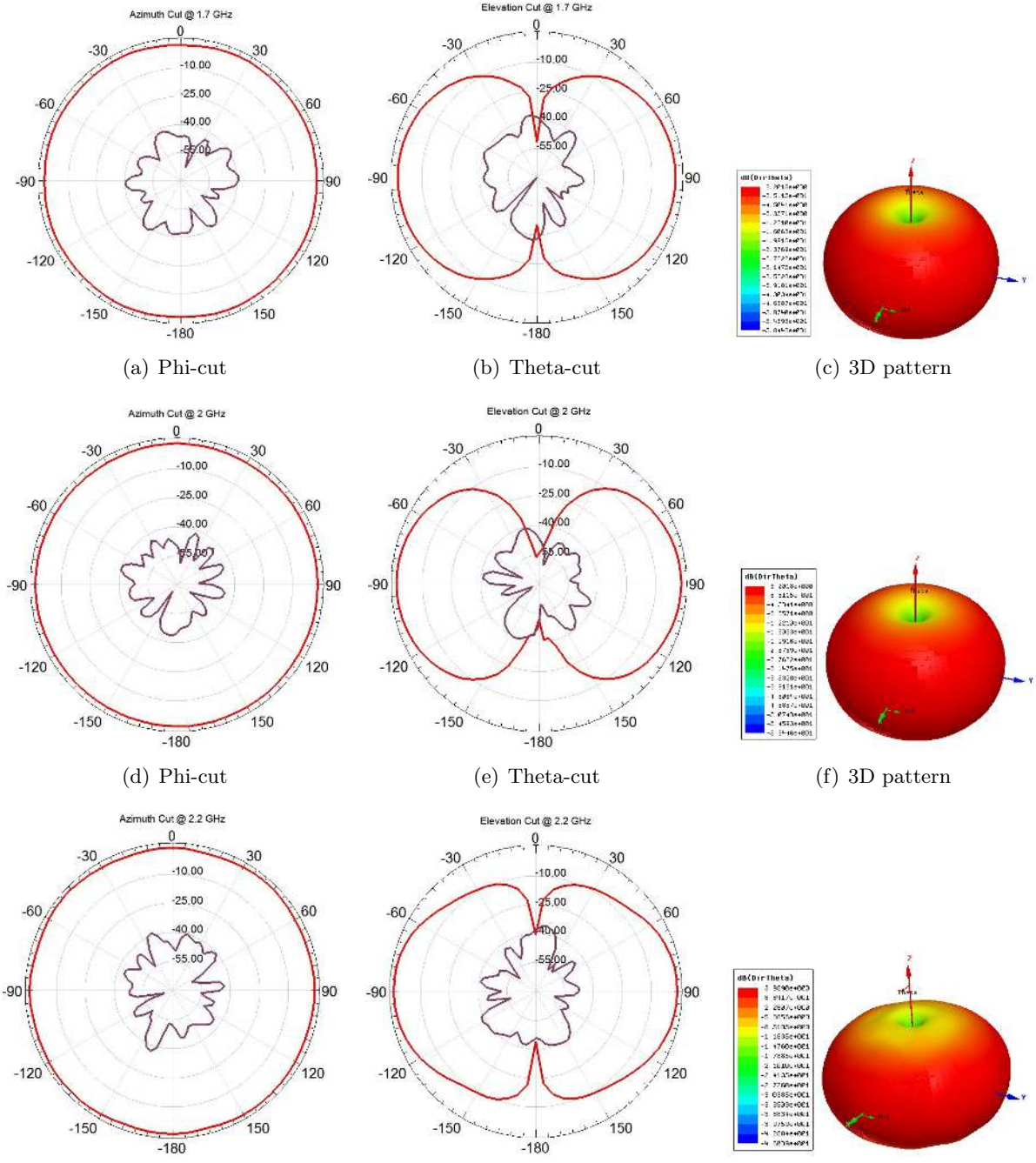

(a) Phi-cut (b) Theta-cut (c) 3D pattern

(d) Phi-cut (e) Theta-cut (f) 3D pattern

(g) Phi-cut (h) Theta-cut (i) 3D pattern

Figure E.6: Vertically polarized Array radiation pattern in OMNI mode @ 1.7, 2 and 2.2 GHz.

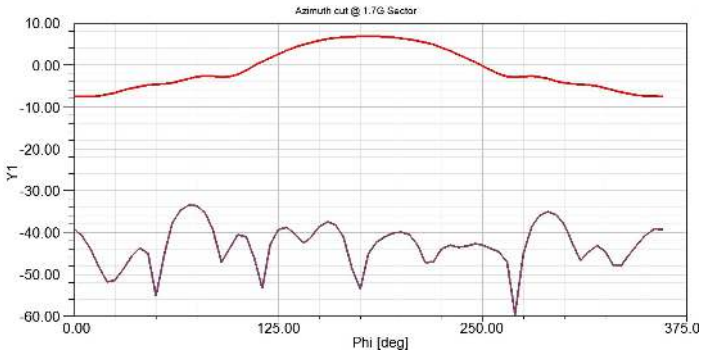

(a) Phi Cut

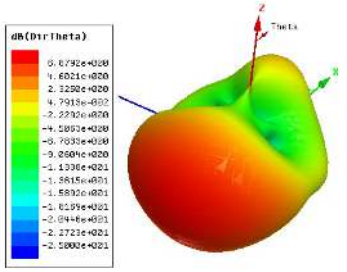

(b) 3D pattern

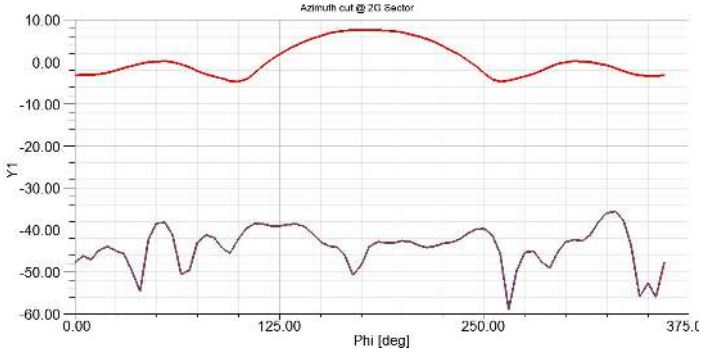

(c) Phi Cut

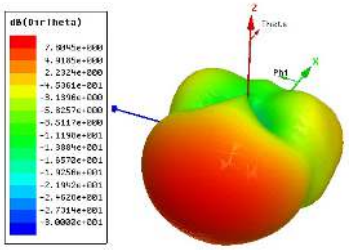

(d) 3D pattern

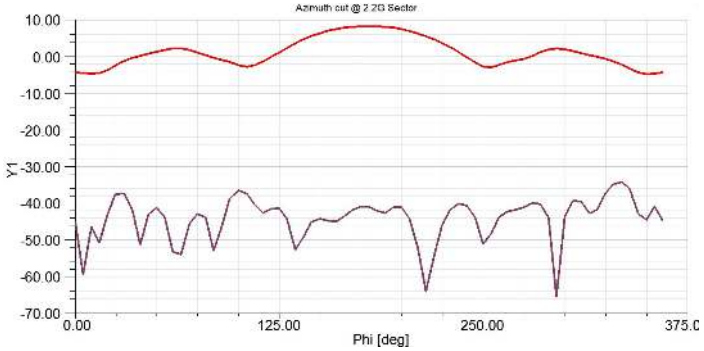

(e) Phi Cut

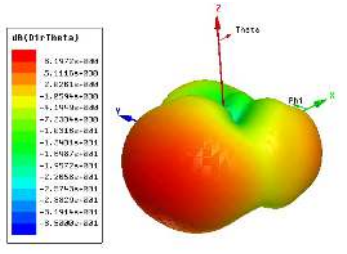

(f) 3D pattern

Figure E.7: Vertical polarized Array radiation patterns in SECTOR mode @ 1.7, 2 and 2.2 GHz

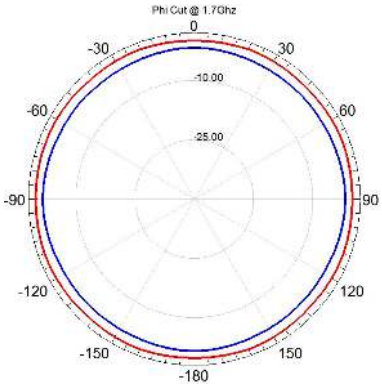

(a) Phi cut

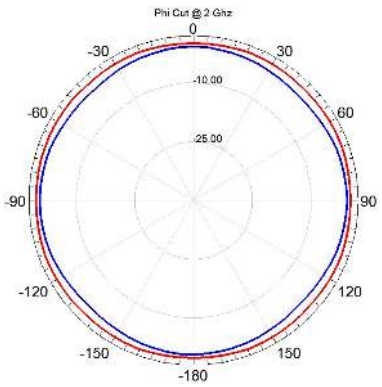

(b) Phi cut

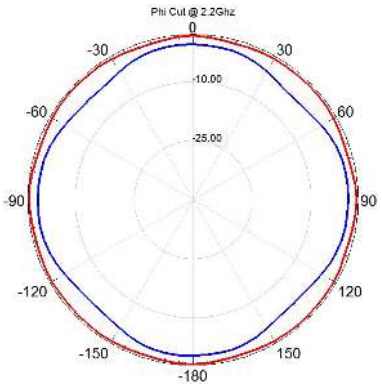

(c) Phi cut

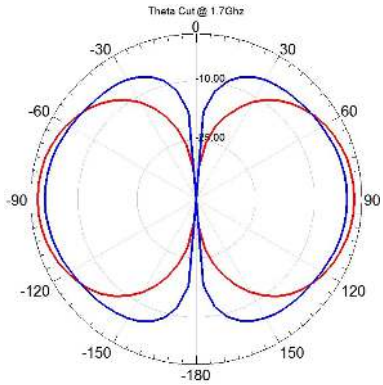

(d) Thetta cut

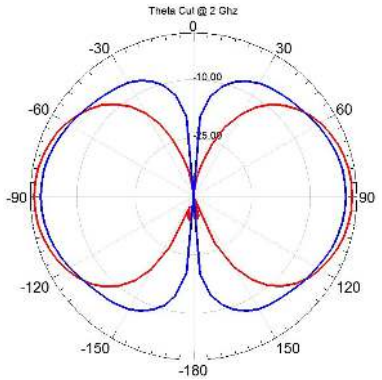

(e) Thetta cut

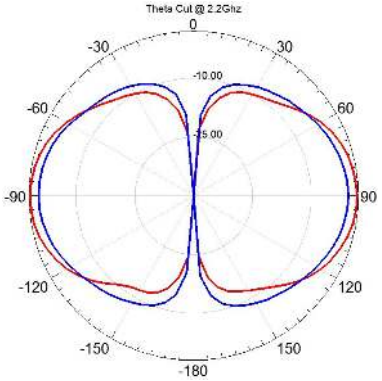

(f) Thetta cut

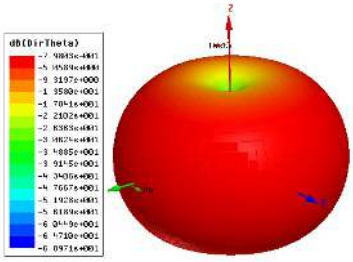

(g) 3D pattern (Vertical Polarization)

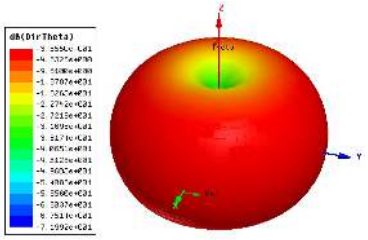

(h) 3D pattern (Vertical Polarization)

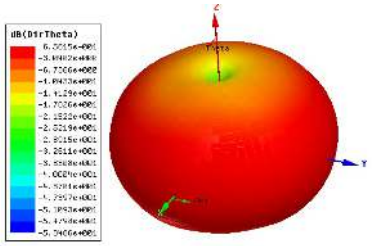

(i) 3D pattern (Vertical Polarization)

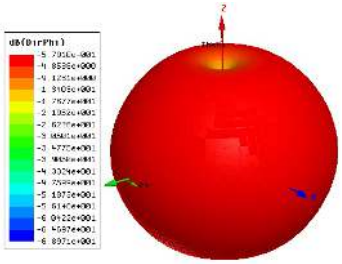

(j) 3D pattern (Horizontal Polarization)

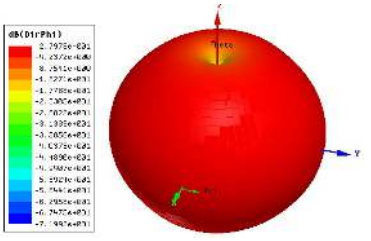

(k) 3D pattern (Horizontal Polarization)

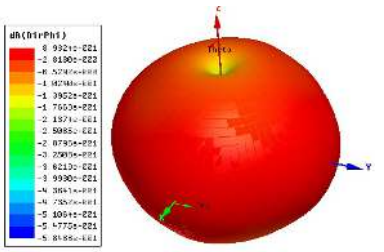

(l) 3D pattern (Horizontal Polarization)

Figure E.8: Dual Polarized antenna - OMNI mode @ 1.7, 2 and 2.2 GHz. Red line : Vertical polarized component, Blue line : Horizontal Polarized component

Table E.1: Elevation and azimuth 3dB (full angle) beam-width simulated values for both polarizations and every mode (OMNI, SECTOR and optimized SECTOR).

	Freq	**Elevation 3dB BW**		**Azimuth 3dB BW**	
		Vertical	*Horizontal*	*Vertical*	*Horizontal*
OMNI	2.2G	50^o	59^o	-	-
	2G	56.5^o	68^o	-	-
	1.7G	66^o	110^o	-	-
SECTOR	2.2G	51^o	64^o	74^o	74^o
	2G	57.5^o	109^o	80^o	90^o
	1.7G	65^o	80^o	89^o	70^o
Opt.SEC	2.2G	52^o	69^o	73^o	76^o
	2G	66^o	115^o	75.5^o	92^o
	1.7G	75^o	86^o	74^o	82^o

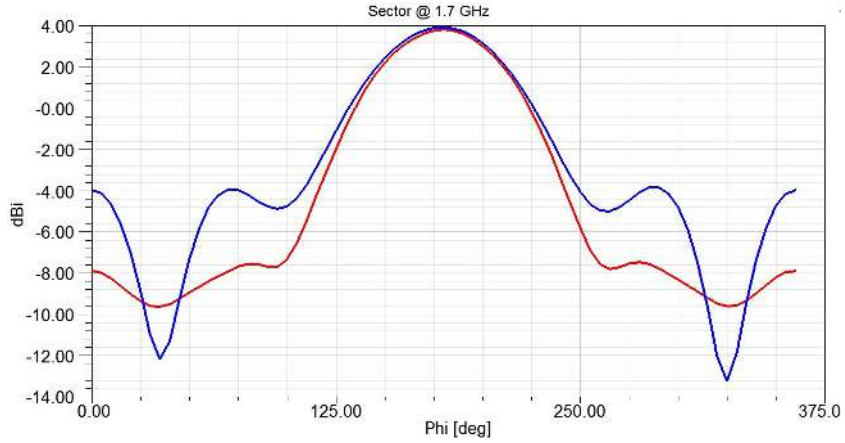

(a) Phi cut

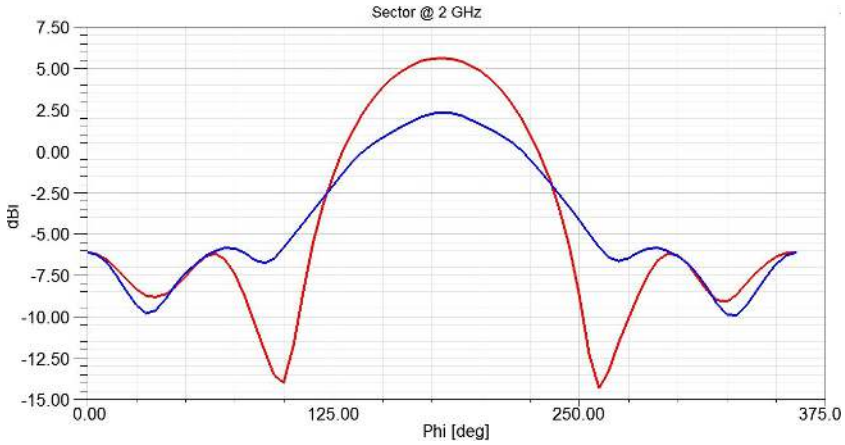

(b) Phi cut

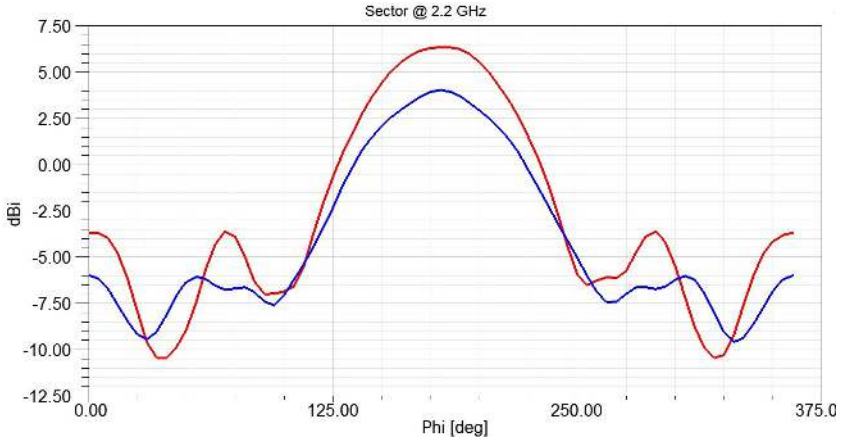

(c) Phi cut

Figure E.9: Dual Polarized antenna - SECTOR mode @ 1.7, 2 and 2.2 GHz. Red line : Vertical polarized component, Blue line : Horizontal Polarized component

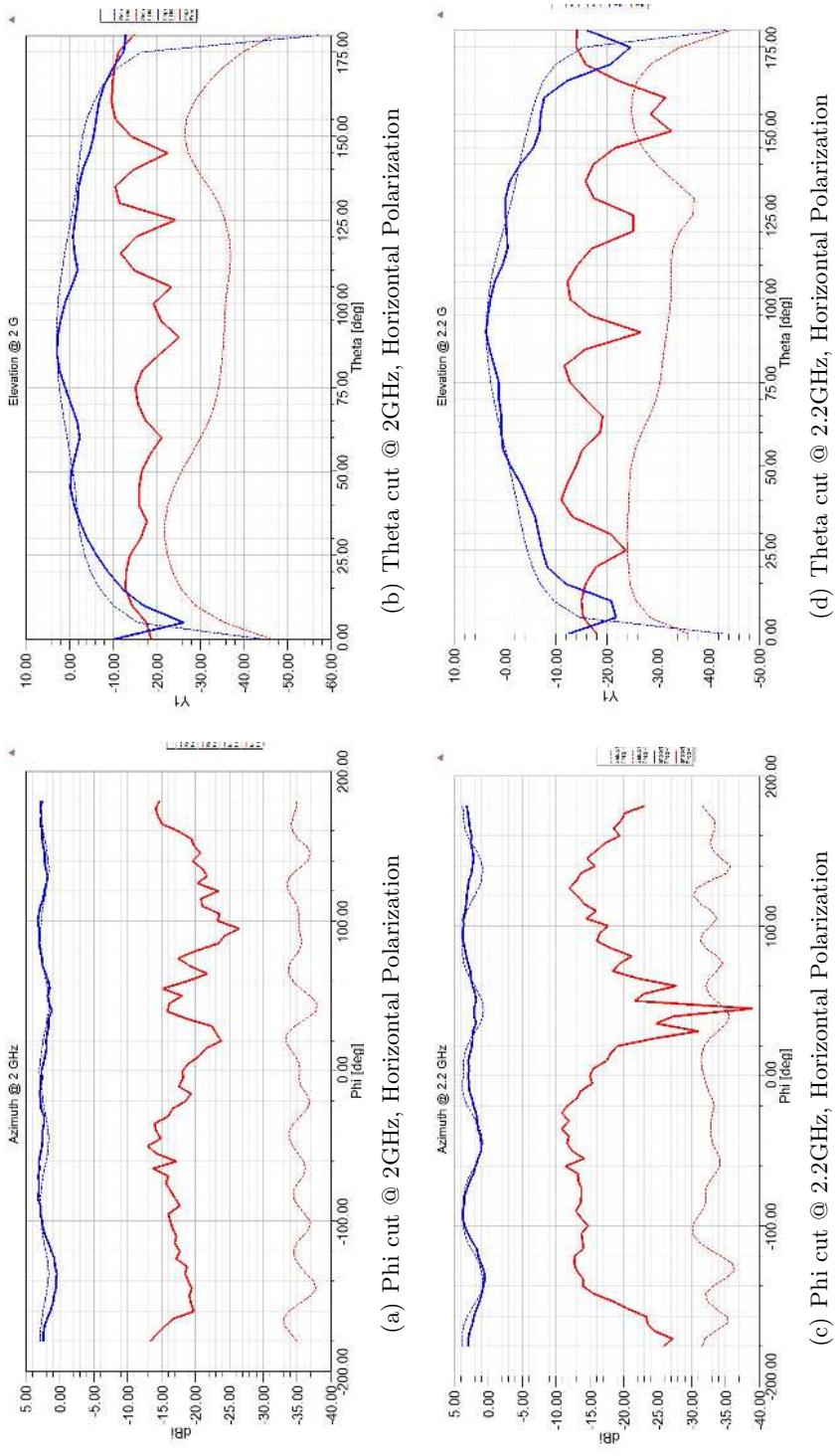

(a) Phi cut @ 2GHz, Horizontal Polarization

(b) Theta cut @ 2GHz, Horizontal Polarization

(c) Phi cut @ 2.2GHz, Horizontal Polarization

(d) Theta cut @ 2.2GHz, Horizontal Polarization

Figure E.10: Measured radiation patterns of the Horizontal components at 2 and 2.2 GHz for OMNI mode. Blue lines indicate Horizontal Polarization (co-polar) and red lines indicate Vertical Polarization (cross-polar). Dashed lines indicate the corresponding simulated patterns.

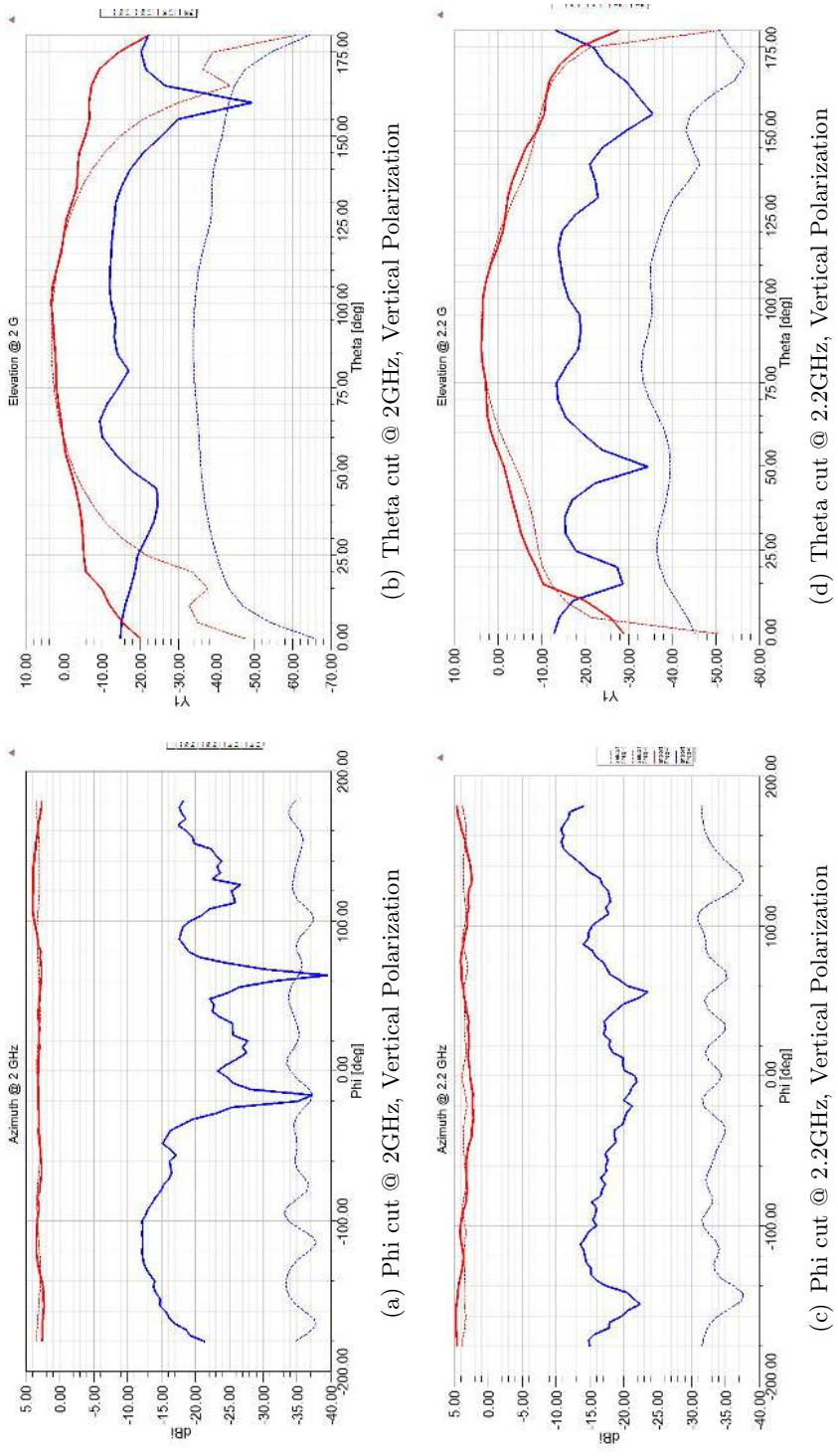

(a) Phi cut @ 2GHz, Vertical Polarization

(b) Theta cut @ 2GHz, Vertical Polarization

(c) Phi cut @ 2.2GHz, Vertical Polarization

(d) Theta cut @ 2.2GHz, Vertical Polarization

Figure E.11: Measured radiation patterns of the Vertical components at 2 and 2.2 GHz for OMNI mode. Blue lines indicate Horizontal Polarization (cross-polar) and red lines indicate Vertical Polarization (co-polar). Dashed lines indicate the corresponding simulated patterns.

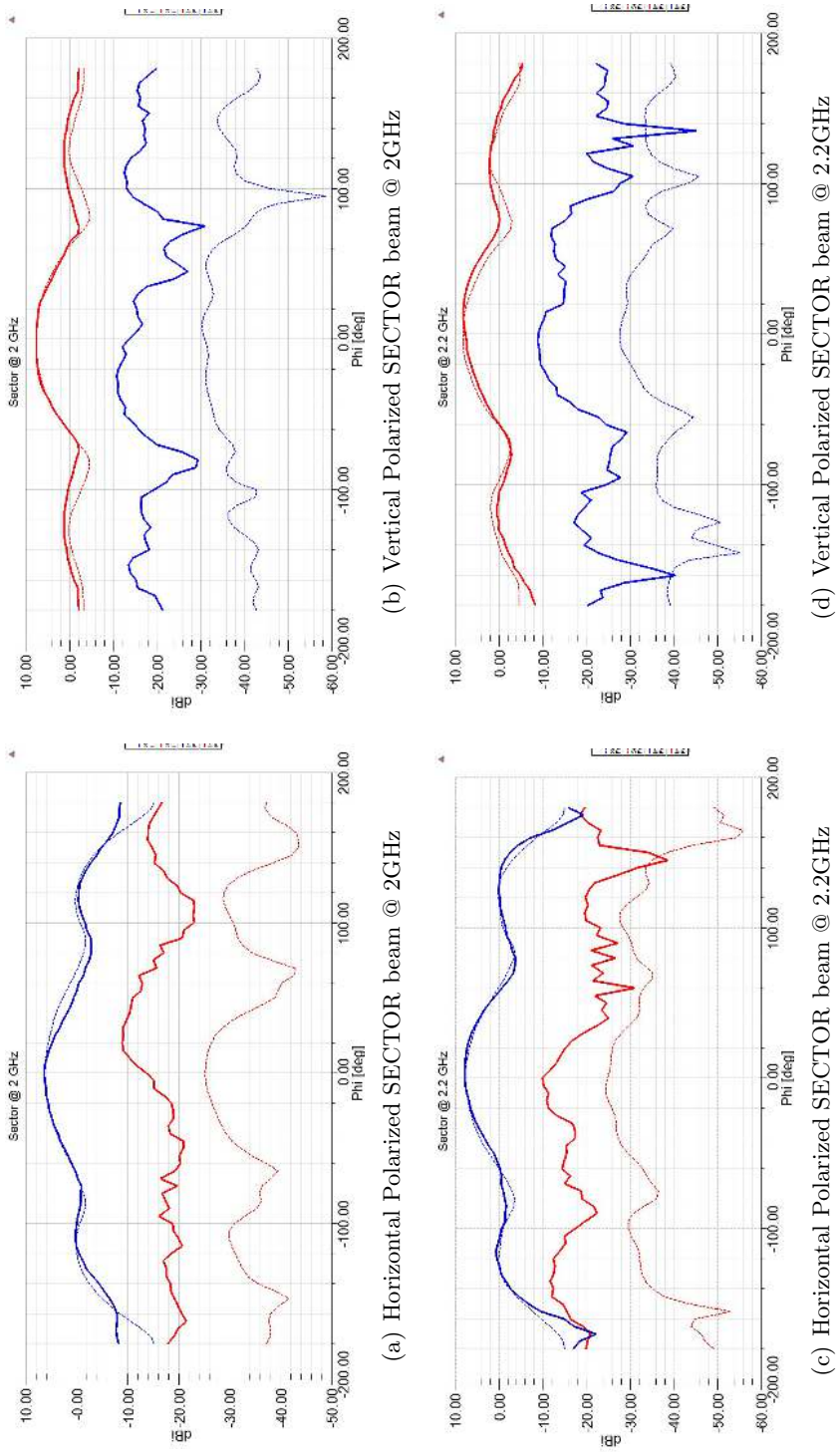

(a) Horizontal Polarized SECTOR beam @ 2GHz

(b) Vertical Polarized SECTOR beam @ 2GHz

(c) Horizontal Polarized SECTOR beam @ 2.2GHz

(d) Vertical Polarized SECTOR beam @ 2.2GHz

Figure E.12: Measured radiation patterns of the Horizontal and Vertical components at 2 and 2.2 GHz for SECTOR mode. Blue lines indicate Horizontal Polarization and red lines indicate Vertical Polarization. Dashed lines indicate the corresponding simulated patterns.

F

HFSS vs CST studio suite

The final antenna structure was designed and simulated in two different 3D electromagnetic simulation softwares, Ansys HFSS 2014.0.7 and CST Studio Suite 2013 v.2013.06 . HFSS solver was used as a frequency domain solver while CST as a time domain solver.

In HFSS, EM analysis in three different frequencies (2.2GHz, 2GHz and 1.7GHz) was set up together with a frequency sweep of 21 samples between 1.5GHz and 2.5GHz for calculation of S-parameters. At 2.2GHz, mesh adaptation took about an hour to complete, producing 377114 tetrahedrons and together with the frequency sweep required 3h and 25min to finish. At 2 GHz adaptation took about 2h and 20min producing 549892 tetrahedrons and at 1.7GHz mesh adaptation needed 5h and 43 min, producing 950432 tetrahedrons. In total, the whole simulation required **11h and 28min** and at maximum 34.4GB of RAM to complete.

In CST Studio suite, the hexahedral cell mesh was chosen with manual (uniform) definition of mesh. Again, field monitors and radiation patterns were setup at frequencies 2.2GHz, 2GHz and 1.7GHz and a frequency range between 1.5 and 2.5 Gigahertz . The hexahedral mesh was formed by 15.291.360 cells and the total required simulation time was **26h and 59min** while the maximum required memory was at 5.6GB. The required simulation time is way longer than HFSS but it is believed that with a more careful initial mesh formation, less cells may produced which will lead to shorter simulation time.

In general, the two softwares produced identical results (S-parameters, Radiation patterns, radiation efficiencies ...). Indicatively, some S-parameters plots are presented below to show the similarity of the results.

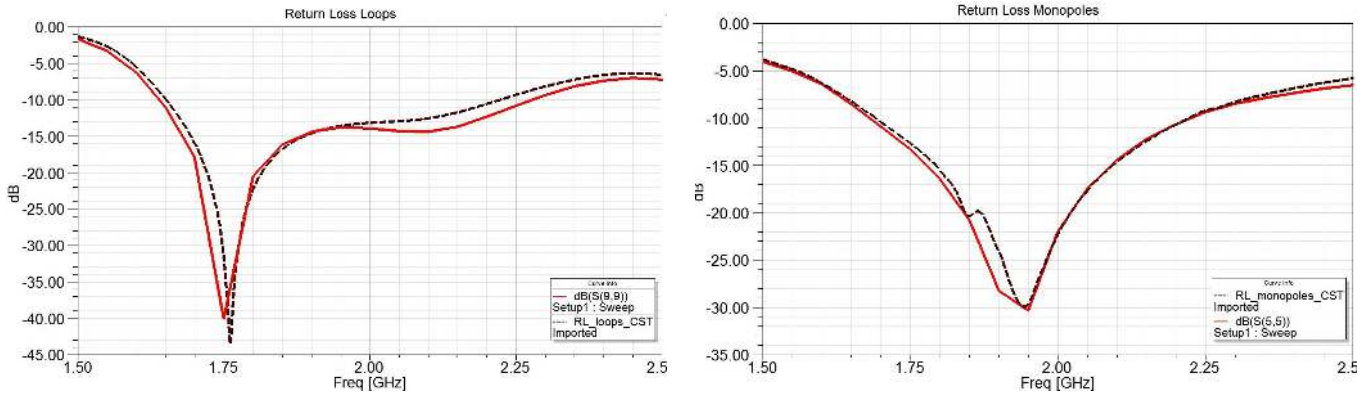

(a) (b)

Figure F.1: HFSS vs CST return loss plots. Loops (Up) and Monopoles (Down) are presented. Red solid line indicates HFSS results and black dashed line indicates CST result.

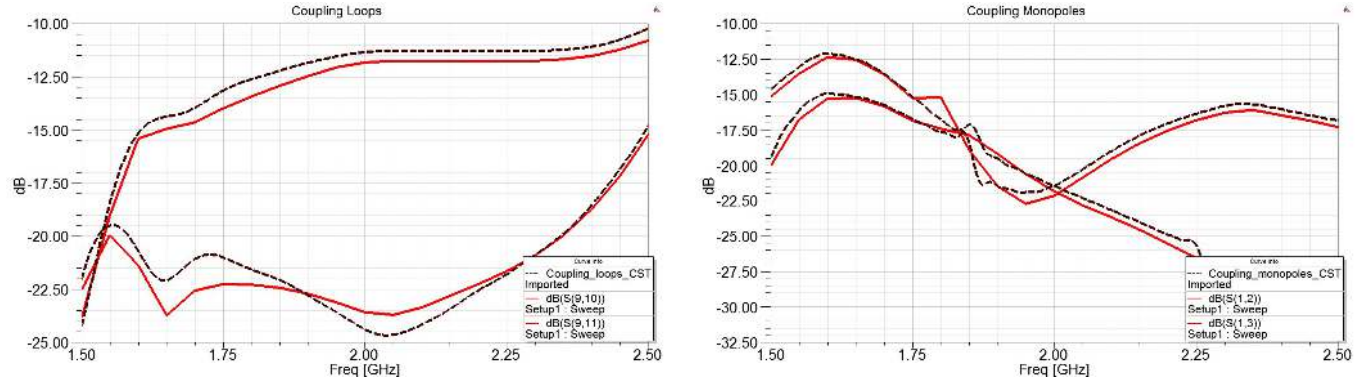

(a) (b)

Figure F.2: HFSS vs CST coupling plots. Loops (Up) and Monopoles (Down) are presented. Red solid line indicates HFSS results and black dashed line indicates CST result.